Positronium Formation at Surfaces and Studies Towards the Production of Low Energy Antihydrogen

A thesis submitted to the University of London for the degree of
Doctor of Philosophy

David Barry Cassidy
Department of Physics & Astronomy
University College London

November 1998

ABSTRACT

A magnetically guided slow positron beam has been used to measure positronium formation fractions via spectroscopy of annihilation radiation. Positrons with energies in the range 0-3 keV were implanted into tungsten, copper, magnesium oxide powder and silica aerogel targets at room temperature and at cryogenic temperatures (~30 K). This was done with and without nitrogen gas condensed on the surface of these materials. The resulting gamma rays were detected by a CsI detector and an associated PC-based spectroscopy system. In most cases studied the measured energy dependence of the positronium fractions was consistent with previous similar work, however, anomalous behaviour was found in some of the data when gas was condensed on metal surfaces.

Using the same positron beam initial measurements of positronium energy distributions have been made. This was accomplished using a HPGe detector to measure the Doppler shift of the energy of the positronium annihilation radiation. This novel technique has not yet been refined and estimates of its potential are reported.

A Monte Carlo simulation of the reaction to form antihydrogen by positronium impact upon antiprotons has been undertaken. Total and differential cross sections have been utilised as input to the simulation which models the conditions foreseen in planned antihydrogen formation experiments using antiprotons and positrons held in Penning traps. Thus, predictions of antihydrogen production rates, angular distributions and the variation of the mean antihydrogen temperature as a function of the incident positronium energy have been made.

Contents

Figure Captions

Chapter 2

Chapter 3

Chapter 4

Table Captions

Acknowledgements

I would like here to express my gratitude to those who, by association, have made the last three years such an enjoyable and rewarding time.

Firstly I would like to thank my supervisor Dr Mike Charlton whose expertise and tuition have always been first rate. I have also been fortunate enough to benefit from a close association with Drs Andrew Garner, Karen Paludan and Nella Laricchia who have provided invaluable assistance and friendship during my studies.

For their technical assistance I am indebted to Ivan Rangué and Ted Oldfield whose patience has been matched only by the vagueness of my requirements.

For their part in the creation of a very friendly and conducive working environment I would like to thank all of the above, my peers, Vanita, Aysun and Henrik as well as some of the departed members of the group, Drs Rowan Finch, Paul Ashley and Jeremy Moxom.

I am also grateful to Dr J Humberston whose knowledge of 3-dimensional co-ordinate geometry has saved me from numerous headaches.

My time spent at CERN and at Aarhus was made possible thanks to the kindness of Dr Jon Merrison whose ability to pull solutions seemingly from nowhere is always astounding. My experience of Geneva was also augmented in the most unforseen ways thanks to Dr Jeff Hangst.

I must also thank Dr Jim Mitroy for supplying me with numerous cross sections, and then for explaining in detail how to download the ones I really wanted.

This work is dedicated to my Mother, Emma, Melanie and Rufus who have had to put up with plenty from me over the years.

Chapter 1: Introduction

1.1 Positrons in the laboratory

Following the prediction by Dirac (1930a) (see appendix 1) positrons were first observed experimentally by Anderson (1932a, 1932b, 1933) in cosmic ray studies using a cloud chamber. Blackett and Occhialini (1933) later confirmed the observation of positrons while performing similar studies and found their charge-to-mass ratio to be of the same magnitude as that of the electron, as predicted by Dirac.

The realisation that positrons are spontaneously emitted from some radioisotopes allowed positrons to be routinely used in the laboratory. Early work with positrons was all based on annihilation techniques using fast β^+ particles. The introduction of slow positron beams was a landmark achievement as far as atomic collision physics is concerned and opened up new avenues of research. It was noticed in 1958 by Cherry that "positrons in the energy interval 0-5 eV, very numerous in comparison with those in equal intervals at somewhat higher energies, were emitted from the chromium on mica surface when it was irradiated by a ^{64}Cu positron beta spectrum". This conversion of fast positrons to those in the energy range 0-5 eV was such that only 1 "slow" positron was emitted for 10^8 fast incident. It was not until 1972 that any real progress was made in improving this conversion efficiency. Canter et al. discovered the so-called smoked MgO moderator. This converted $3x10^{-5}$ of the fast positrons to slow positrons and this allowed a (low intensity) slow positron beam to be used for the first time. This then gave rise to rapid progress in the understanding of positronic phenomena, and consequently moderators (those materials which slow positrons down and re-emit them at low energy) of ever increasing efficiency were discovered, with a corresponding rise in slow positron beam intensities. Solid neon moderators are the most efficient known today, which have an efficiency of around 10^{-2}.

The positron is now used as a non-destructive bulk and surface probe of various materials, especially in the detection of structural defects such as vacancies, and in the study of electronic momenta distributions. Atomic collision and scattering experiments carried out with positrons, electrons , protons and antiprotons have proved very successful in isolating

mass and charge effects in many types of processes and in the understanding of electron exchange, polarisation and electron capture effects. Positron studies are also of relevance to astrophysics. For example, the characteristic annihilation radiation of positrons has been observed in solar flares and also in radiation emissions from the galactic centre. A more practical use of positrons might be positron emission tomography, which is a well established medical imaging technique used for observing dynamic processes in the body such as blood flow and metabolism.

1.2 Some properties of the positron

The positron is the anti-particle of the electron and as such it will, according to the CPT theorem, possess the electronic mass, lifetime and gyromagnetic ratio. The electric charge and magnetic moment of the positron are equal and opposite to those of the electron. It is also a fermion, with spin 1/2 (in units of $\hbar$). Just as high energy photons can excite an electron from the Fermi sea and produce an electron-positron pair, so too can an electron-positron pair annihilate and produce photons, the energy of which is (in the rest frame) equal to the rest mass of the two particles, $2mc^2$, or 1.022 MeV. The number of photons that are produced following annihilation is determined by the quantum states of the particles, according to (Yang 1950)

$$(-1)^n = (-1)^{l+S} \qquad (1.1)$$

Where, n = number of photons, l = total orbital angular momentum and S = total spin of the system. Fig 1.1 shows the Feynman diagrams for radiationless, 1 photon, 2 photon and 3 photon annihilation.

The cross section of these decay modes depends on the number of vertices in the corresponding Feynman diagram, unless momentum conservation considerations come into play. This is because each node represents a photonic interaction and nature prefers to minimise such events. The cross sections are proportional to α^m, where m is the number of vertices and α is the fine structure constant.

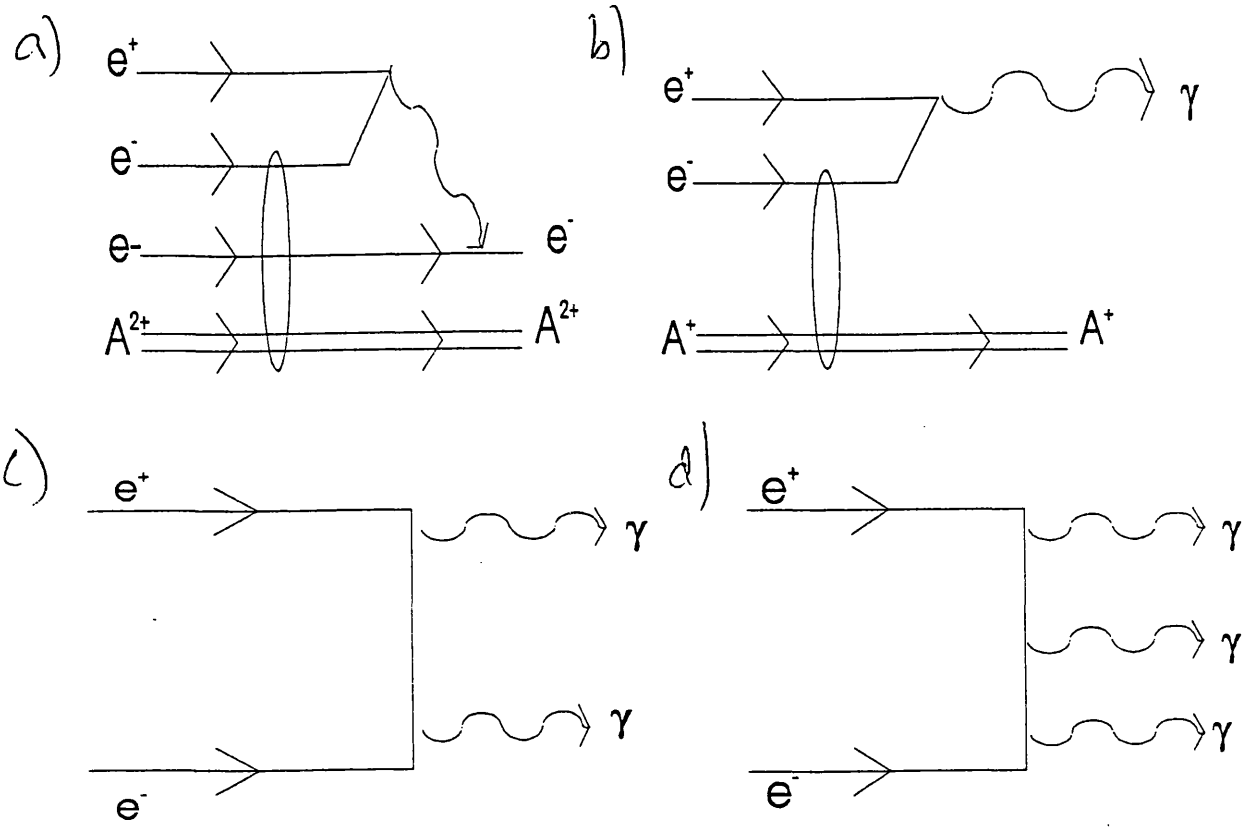

Figure1.1 (a) - (d). The Feynman diagrams of radiationless, 1 photon, 2 photon and three photon annihilation of a positron and an electron.

The processes shown in (a) and (b) are those of radiationless decay and single quantum annihilation respectively. In the first the annihilation energy is absorbed by a bound electron which then escapes from the atom. The resulting atom is thus doubly ionised since one electron has escaped and another takes part in the annihilation. In the single quantum annihilation, in order to conserve momentum, the presence of a third body is required. In fact, both of these processes are suppressed because of their need for an interaction with the atom or nucleus and the most probable decay mode is shown in (c), the two photon annihilation. Note that from 1.1 this channel is open only when $J = l + S$ is an even number. So, when the positron and electron are in a spin singlet state two photon annihilation is the most likely. The non-relativistic limit of the cross section for this process is (Dirac 1930b)

$$\sigma_{2\gamma} = \pi c \frac{r_0^2}{v_{rel}} \qquad (1.2),$$

where v_{rel} is the speed of the positron with respect to the electron. If the annihilation takes place in an atomic gas 1.2 is modified to 1.3 and in an electron gas it is modified to 1.4,

$$\sigma_{2\gamma}(A) = \pi c \frac{r_0^2}{v_{rel}} Z_{eff} \qquad 1.3$$

$$\sigma_{2\gamma}(e^-) = \pi c \frac{r_0^2}{v_{rel}} n_e \qquad 1.4,$$

Where Z_{eff}, is thought of as the effective number of electrons available for annihilation and n_e is the electron density.

The three photon annihilation cross section has been calculated (Ore and Powell, 1949) to be a factor of 370 less than the two photon cross section shown above. Thus, in direct annihilation the three photon contribution is negligible. Higher order channels are similarly suppressed.

It is possible for a positron and an electron to form a hydrogenic bound state, known as positronium, the gross energy levels of which are half those of hydrogen (because its reduced mass is approximately half that of hydrogen). The positron has a magnetic moment 658 times larger than a proton and this causes the hyperfine structure in the positronium energy levels to differ significantly from those of hydrogen. In addition to this there are other effects due to quantum electrodynamics, such as virtual annihilation. The following discussion is limited to ground state positronium only.

Positronium can be formed either with the electron and positron spins parallel or antiparallel. The former is known as ortho-positronium, or o-Ps and the total spin of such an atom is 1. The latter is called para-positronium (p-Ps) and has a total spin of 0. The relative spin orientations of the electron and the positron affects the interaction of the individual particle wavefunctions. When the spins are parallel it becomes more difficult for the two wavefunctions to overlap, and hence for annihilation to occur, and so ortho-positronium (lifetime in vacuum 142ns) is longer lived than para-positronium (vacuum lifetime 125 ps).

Also, the magnetic quantum number depends on the total angular momentum, which depends on spin. This number takes on integer values from -l to +l. Thus, ortho-positronium can exist in three magnetic quantum substates, while para-positronium can have m = 0 only.

Since, in the absence of an external magnetic field, these states are energy degenerate, they are equally likely to be formed. This means that, since there are three sub-states of o-Ps and only one of p-Ps, o-Ps is three times more likely to be formed. In terms of experimental physics this is fortunate in that the longer lived positronium lends itself to many different roles.

As we have seen, positronium is only quasi-stable and eventually decays. The number of photons created depends on the spin states of the positron and electron, just as we saw for direct annihilation. Thus, equation (1.1) demands that o-Ps decay into an odd number of photons (the most probable being three) and p-Ps into an even number of photons (the most probable being two). The two photons resulting from p-Ps decay are emitted with equal energies (511 keV, which, along with direct annihilation, gives rise to a peak in the annihilation spectrum, known as the "511 photopeak") in the centre of mass frame and back to back (i.e., at an angle of 180^0 to each other). In the laboratory frame the momentum of such p-Ps may be inferred from deviations from collinearity. Doppler shifts of the photon energy may also occur due to the velocity of the centre of mass of the annihilating pair. The three photons emitted from o-Ps decay are co-planar and may have energies up to 511 keV. The energy distributions of such photons has been calculated a number of times and is shown in figure 1.2 with some experimental results due to Chang et al (1985a).

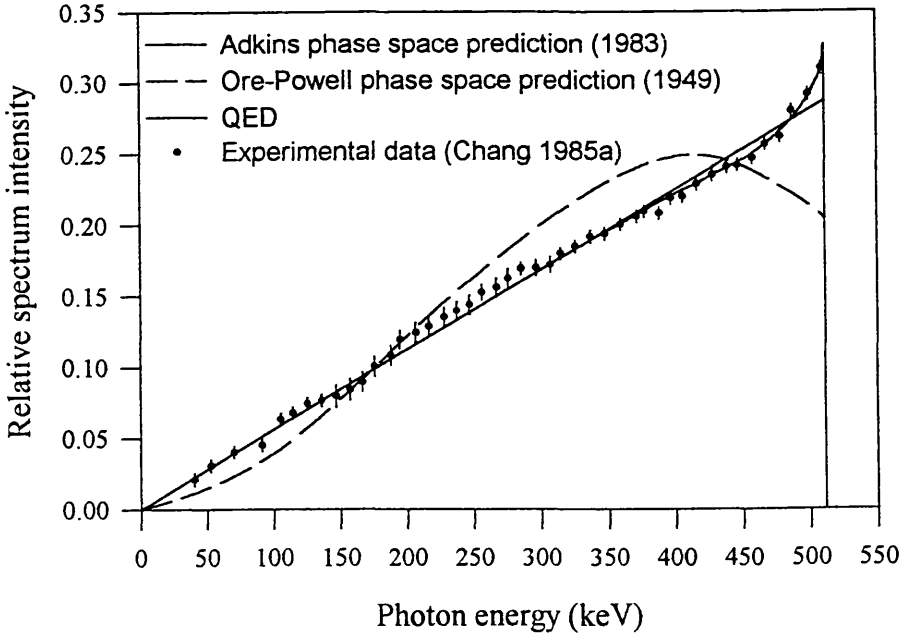

Figure 1.2. The energy distribution of radiation from the decay of o-Ps (Schultz and Lynn 1988)

1.3 Slow positron beams

This section is a brief overview of physics relevant to the development of slow positron beams. It is necessary to focus this description on a discussion of moderation, the process by which slow positrons are obtained from fast β^+ particles or accelerators. Thus we shall consider some of the possible processes which may affect an energetic positron implanted into a solid. Beyond this stage the only fundamental difference between slow positron beams is the method of beam transport.

1.3.1 Positrons in solids

Understanding the interactions of positrons with solids is very important in terms of slow beam production. Figure 1.3 shows positrons with energy <100keV in the near surface region of a solid. Many of these processes are relevant to the experimental work described in this thesis. In particular the slowing down of positrons in solid materials is fundamental to positronium formation at surfaces by thermalised positrons, while the first encounter scattering events determine the degree of positronium formation in backscattering.

1.3.1.a Implantation

A positron may be said to have stopped in a material when its motion is characterised by its temperature (that is, its kinetic energy is equal to its thermal energy) or if it is trapped at a particular site. The geometrical distance from the surface to the point where the positron has stopped is known as the implantation depth. For a positron beam normally incident on a target the probability of stopping at a certain implantation depth, z, is given by an implantation profile P(z). This function depends on the initial energy of the positrons and the nature of the target. Positrons diffusing in the final stages of thermalisation will have only a small effect on the final penetration depth at keV incident energies where the diffusion length is short by comparison with z. For lower energies the diffusion length may be of the same order as z, and in this case the implantation profile is less well defined and is dominated by the thermal motion. Also, since the diffusion process has no preferred direction the profile will simply become "blurred" by this process. The extent to which this occurs is dependent on the ratio of the penetration depth and the diffusion length.

The implantation profile for unmoderated β^+ particles has been studied by Brandt and Paulin (1977) for various materials. Annihilations resulting from β^+ impact in samples were monitored by a detector which was moved across a thin slit in the Pb shielding which surrounded the source/sample arrangement. An implantation profile of the form

$$P(z) = \alpha_+ \exp\{-\alpha_+ z\} \qquad (1.5)$$

was obtained by fitting the results obtained. Here z is the distance travelled by the β^+ particles in the sample and α_+ is the absorption coefficient. Mourino et al (1979) have noted that this quantity is well described by the mean β^+ energy, the endpoint energy, E_m, and the atomic number of the target material, Z. Thus, they have found, by fitting their data,

$$\frac{\alpha_+}{\rho} = 2.8\frac{Z^{0.15}}{E_m^{1.19}}(cm^2 g^{-1}) \qquad (\text{for } ^{22}\text{Na}) \qquad (1.6).$$

Mills and Wilson (1982) performed experiments on thin films (~ 3000 Å) of Cu, Al and Si (See fig 1.4 below) with a monoenergetic beam. It was found that the mean implantation depth, $\bar{z}$, varied inversely with the mass density ρ. In the case of aluminium and copper they found that $\bar{z}$ varied as

$$\bar{z} = AE^n \quad (\text{Å}) \qquad (1.7),$$

where n = 1.6 (+ 0.15, - 0.08) for Al , n = 1.3(+ 0.07, - 0.11) for Cu and A~ 400/ρ ÅkeV^{-n}. E, the beam energy, was varied from 1 to 6 keV. Other work using a similar technique has been performed by Baker et al(1991) in which higher beam energies were used (10-50 keV) and they have found deviations from 1.7 as well as showing that a simple mass density scaling is not sufficient.

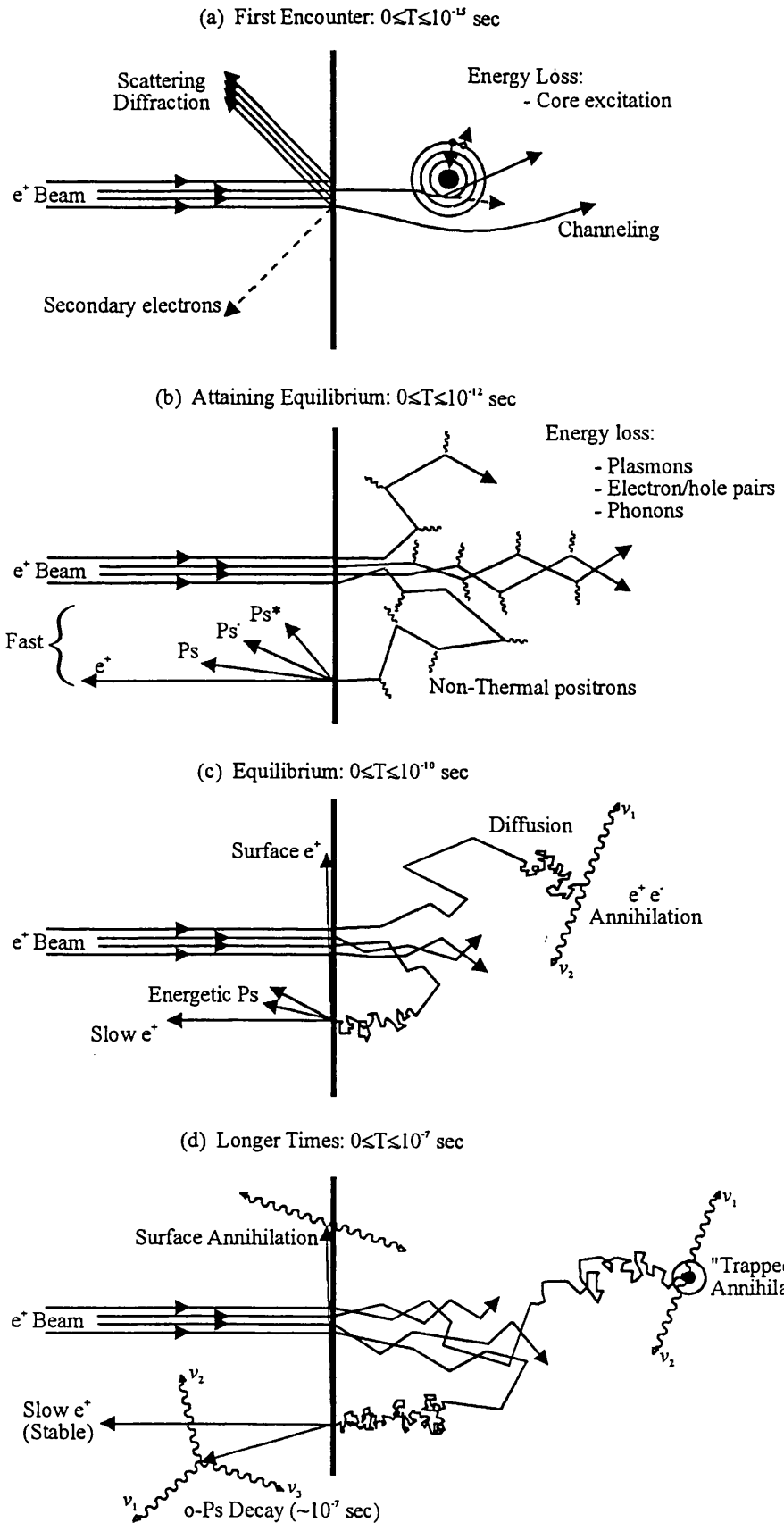

Figure 1.3 Interaction of a positron beam in the near surface regions of a solid. Schultz and Lynn (1988)

Monte Carlo calculations by Valkealahti and Nieminen (1983 and 1984) of implantation in the energy range 1-10 keV have shown good agreement with experiment. Their data was fitted to a Mahkovian distribution, which is of the form

$$P(z) = \frac{mz^{m-1}}{z_0} \exp[-(z/z_0)^m] \qquad (1.8)$$

Where, m is a shape parameter. When m = 2 equation (1.28) describes a Gaussian derivative profile, and for m = 1 a simple exponential profile. The quantity $\bar{z}$ is related to the mean implantation depth, z_0, as,

$$z_0 = \frac{\bar{z}}{\Gamma[\,(1/m)+1\,]} \qquad (1.9).$$

The dependence of $\bar{z}$ on the gamma function, Γ, simplifies for some profiles (Schultz and Lynn 1988), e.g., for the exponential (m=1) $\Gamma(2)=1$ and for the Gaussian (m=2), $\Gamma(3/2) = \frac{\sqrt{\pi}}{2}$.

The shape parameter obtained by Valkealahti and Nieminen for 3 and 5 keV positrons incident on Cu was m ~ 1.9, however the results of Mills and Wilson (1982) were more closely fitted by m = 1.4. The stopping profiles obtained in this way are shown in figure 1.4.

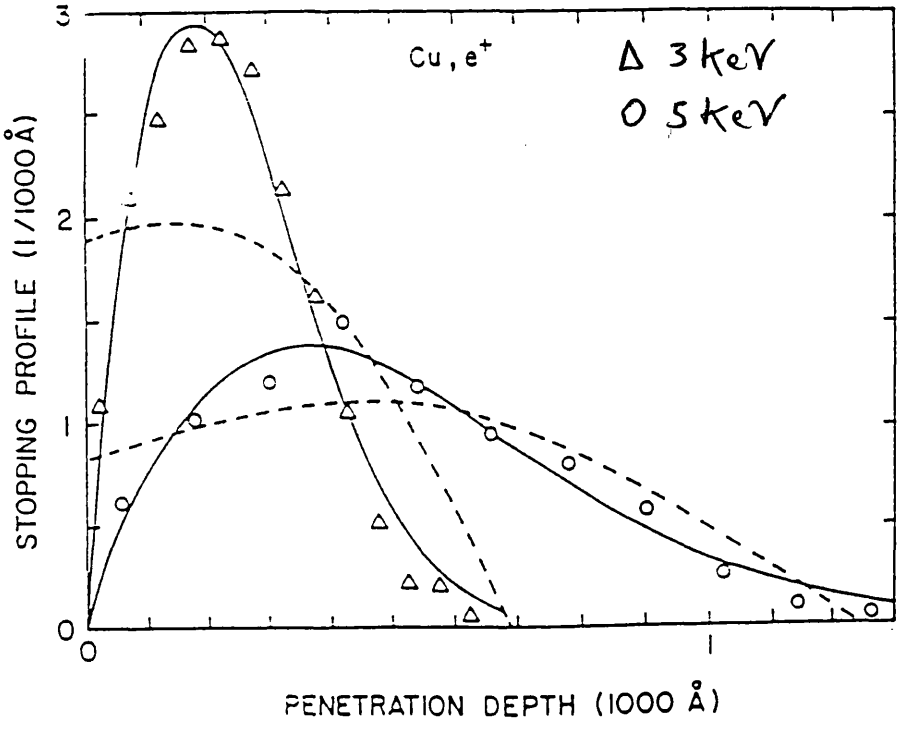

Figure1.4. Stopping profiles of 3 and 5 keV positrons in Cu from the Monte Carlo calculation of Valkealahti and Nieminen, taken from Schultz and Lynn (1988)

The factors which determine the final implantation profile and stopping depth in a solid are almost completely due to fast inelastic collisions. Thus, for high energies (tens of keV) the implantation profiles are very similar in form for most materials. The energy loss mechanisms for near thermal particles (~ 10 eV or so) are much more dependent on the target material.

1.3.1.b Thermalisation

Energy loss for very high energy positrons (MeV) in solids occurs primarily via bremsstrahlung emission of radiation. This involves an interaction between the positron and the (screened) Coulomb field of a nucleus or one of the electrons, resulting in the emission of a photon. This is much less efficient as an energy loss mechanism for positrons than it is for electrons since the former are attracted to the atomic electrons and repelled by the nucleus.

Following radiative stopping (several hundred keV), particle trajectories are randomised by relativistic nuclear (Mott) scattering and energy is then lost by electron scattering until the positron energy is reduced to around 100 keV. Then core and valence electron excitation are the dominant energy loss processes.

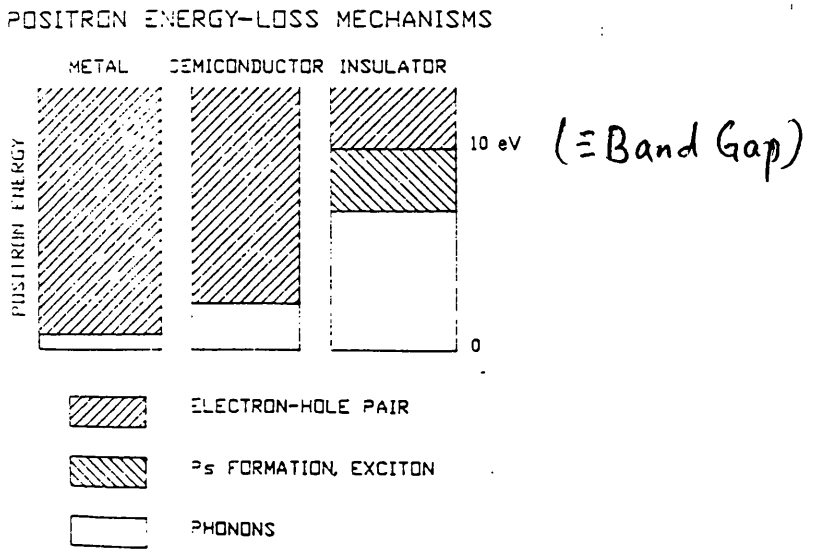

Figure 1.5. Energy loss processes in different types of materials from Schultz and Lynn (1988)

In metals, energy loss below the (core) ionisation threshold is predominantly due to inelastic scattering (Perkins and Carbotte 1970) with free electrons in the Fermi sea (conduction electrons) or by plasmon excitation (Oliva 1980). Interaction with the Fermi sea may occur as a single particle exciting an electron from this sea and thereby creating an electron-hole pair or by a collective density variation with the entire sea. The latter may be described by treating the conduction electrons as a plasma, the coupling of which with the charged positron can produce oscillations, known as plasmon excitations. At higher energies this process is quantitatively described by a dipole interaction. That is, electrons are attracted to the positron as it moves along, resulting in the accumulation of negative charge behind the positron, creating a dipole which in turn decelerates the positron.

Inelastic scattering with conduction electrons is the most important energy loss process for positrons below the (core) ionisation threshold in metals, but this falls off below the Fermi energy and the final stage of thermalisation is dominated by phonon scattering (Perkins and Carbotte 1970). These processes are temperature dependent and are significantly slower than those discussed previously, with thermalisation times of a few ps. Note that increasing electron density leads to increased screening of the positron-electron interaction and this gives rise to longer thermalisation times, in some cases exceeding the mean positron lifetime (Carbotte and Arora 1967). Figure 1.5 shows the energy loss processes for metals, semiconductors and insulators.

In semiconductors and ionic solids energy loss mechanisms are similar to those in metals, except that electron-hole creation is only possible if the positron energy is larger than the band gap. Measurements of the energy distributions of positrons reemitted from various ionic solids (Mills and Crane 1984) have observed energies in the range ~5-10 eV with 500 eV positrons incident on targets at 330K. Lynn and Nielsen (1987) have suggested that the energy of the positrons may be due to a slower rate of energy loss to phonons compared with that of electron-hole excitations so that positrons with energy below the band gap can diffuse to the surface and be reemitted before they lose much energy to phonon excitation. The formation of positronium in metals and semiconductors is generally thought not to occur since the high electron density causes screening, which reduces the electron-positron attraction.

It is often energetically possible for positronium formation to take place in insulators. This leads to a radical departure from the thermalisation process discussed above. Since positronium is electrically neutral the excitation of plasmons or electron-hole pairs is no longer possible, and so the energy loss rate in insulators is further reduced, and is largely determined by phonon scattering. The energy loss to optical phonons is larger than that to acoustic phonons (Schultz and Lynn 1988) and so in a system where the optical branch is open we expect the positronium thermalisation time to be determined by inelastic scattering of positronium by optical phonons. In materials which have no optical phonon branch (monatomic structures, such as the rare gas solids) the energy loss is very small. Gullikson and Mills (1986) have reported positron energy losses per collision in solid Ne of only 6meV, in accordance with the solid Ne average phonon energy.

1.3.1.c Diffusion

Positrons which thermalise in metals or semiconductors, as described above, usually do so in a time that is short compared to their lifetimes and therefore spend most of their lives interacting with the solid at low (thermal) energies. The motion of these positrons in the final stages of thermalisation becomes random as they undergo a multitude of collisions. Drift effects may be superimposed on this random motion, for example by the application of an electric field. This type of motion is described by the diffusion equation,

$$\frac{\partial n(x,t)}{\partial t} = D_+ \nabla^2 n(x,t) - \lambda n(x,t) - v_{dr} \frac{\partial n(x,t)}{\partial x} \qquad (1.10).$$

Here D_+ is the positron diffusion coefficient, n(x,t) is the positron probability density and is a function of time and position, λ is the decay rate and v_{dr} is a (field dependent) drift velocity. We shall consider only metals and semiconductors in this section since, as noted previously, the thermalisation of positrons in insulators is often rather slow and so the dynamics may not be characterised by (1.10) since this equation (as written) refers to near thermal motion only. Since the mean free path of the positrons is generally much smaller than the implantation depth it is assumed that (1.10) will be applicable (i.e. that the positrons will not diffuse right out of the material after very few collisions). We shall not consider any of the various solutions to this equation (e.g. Mills and Murray 1980, Jorch et al 1984, Beling et al 1987) but shall simply note that the assumptions behind its use are thought to be valid (McMullen, 1985).

Experimentally D_+ may be found by measuring the fraction of implanted positrons which return to the surface as free positrons or which form positronium. Such measurements are often complicated by uncertainties regarding which stopping profiles to use. Also, there are other parameters that should be taken into account in efforts to measure D_+. For example, knowledge of the positronium formation fraction may be important and this requires (see section 2.6) a calibration of the reference states for 0 and 100% Ps formation, or it may be necessary to know accurately the detection efficiency of the system in order to calculate absolute reemitted positron fractions. (see section 3.4). The diffusion coefficient is related to the diffusion length as

$$L_+ = (D_+\tau)^{1/2} \qquad (1.11),$$

where τ is the average positron lifetime (~ 100 ps in a metal, ~500 in an insulator). A typical value for L_+ is 1000Å. This represents the average distance that a positron may travel, by a random walk, during its lifetime. If this quantity is of the order of the implantation depth then the positron may return to the surface and be reemitted, either as a free positron or as positronium. The implantation depth for β^+ particles is typically around 10^6Å, which highlights why primary moderation efficiencies are so small.

Defects in the structure of solids, such as vacancies, can lead to trapping of positrons and thus reduce the diffusion length. This will necessarily reduce the probability of any positrons being reemitted from the target. The efficiency of vacancy trapping of thermal positrons has been calculated by Hodges (1970) to be of the order of 10^{15} per second per unit concentration of vacancy. This is illustrated by Dupasquier and Zecca (1985) who have calculated that in aluminium a vacancy concentration of 20 per atomic million can reduce the diffusion length by ~15%.

1.3.1d Positronium formation in solids

Since the free electron density is low in insulators it is possible for the formation of positronium to occur within such materials without inducing an ionising dipole, as would take place in a metal or semiconductor. Positronium formed in such a medium generally has a distorted atomic structure due to the surrounding lattice structure of the insulator.

Some parameters, such as the lifetime and binding energy, are therefore different to those of free positronium. One mechanism by which positronium is thought to form in insulators is known as the spur model, first put forward by Mogensen (1975). In this scenario an energetic positron enters the material and creates many ions and free electrons as it loses energy. Then, as the positron thermalises, it finds itself in the ionisation "spur" region and may combine with a free electron to form positronium. Another description of positronium formation is the Ore (1949) model, which was devised to explain the formation of positronium in gases but may be applied to more dense media. This model involves a consideration of the energetics of positronium formation, in which a positron-electron pair gain some binding energy E_b but must expend sufficient energy to promote a valence electron to the band gap, E_{gap}. The initial kinetic energy of the free positron must therefore be at least $E_{min} = E_{gap}-E_b$. It is also postulated in this model that positronium will become unstable if formed with a kinetic energy in excess of the binding energy E_b (which is less than the vacuum binding energy, 6.8 eV). This occurs when the positron kinetic energy is greater than E_{gap} so that interactions with other bodies, which are inevitable in a dense medium, will break up the atom. The formation of positronium is thus only viable in the positron energy (E) range $E_{min}<E<E_{gap}$. Both of these models are imprecise and either too complex to model accurately (spur) or too simplistic (Ore) to be of much use. Positronium formation in insulators has been observed for many materials such as ice, SiO_2, MgO, NaF, N_2 and most rare gas solids. (See, for example, Gullikson and Mills 1986, Mills and Crane 1984 and chapter 3).

1.3.2 Positrons at surfaces

For thermalised or near thermalised positrons returning to a surface after implantation the most likely processes are,

i) Reemission into the vacuum as a free positron. This requires the material in question to have a negative positron work function ϕ_+ unless the positrons are not thermalised and have enough kinetic energy to overcome the potential barrier of positive work function materials.

ii) Positronium formation. If a positron escapes from the surface and interacts with an electron as it does so it may form positronium, and this atom may then continue away from the surface.

iii) Localisation of the positron in a surface state. This may occur because of the image potential at the surface or if defects in the near surface region create potential wells into which the positron may fall. Any positrons stuck in a surface state could also form positronium which may be thermally desorbed.

iv) Reflection of the positron wave function by the potential step at the surface. This may be repulsive (for ϕ_+ positive) or attractive (for ϕ_+ negative).

1.3.2.a Surface Potential

Figure 1.3 Shows some of the possible fates of a positron interacting with a surface. The potential seen by the particles which determine these processes is made up from several different sources. The bulk potential is simply the repulsion from the ion cores combined with the attraction of the conduction electrons. Then, for a lattice without defects, the ion density abruptly vanishes at the surface, but the electron cloud spills out and a dipole effect is created by these charges. This serves to attract positrons towards the surface. Then, for positrons outside this cloud of electrons, the Coulomb field of the positron must be such that the electric field lines terminate at the surface and are perpendicular to it. This has the effect of producing a so called image potential, which may be thought of as the attraction between a positron and a mirror image particle (electron). The image potential is therefore attractive. The sum of all these effects is shown in figure 1.6.

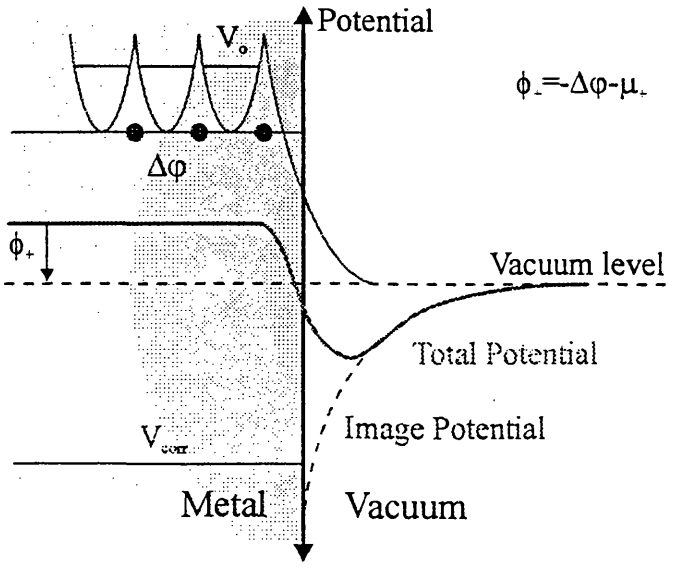

Figure1.6. The different components of the potential seen by the positron at a surface.The positron chemical potential includes terms due to the correlation with the conduction electrons (V_{corr}) and the interaction with the ion cores (V_0). (Schultz and Lynn 1988).

1.3.2.b Reflection

As seen in figure 1.3, not all positrons in the near surface region of a solid actually cross the solid-vacuum interface. There is the possibility of a quantum mechanical reflection by the potential step at the surface and this must also be considered. The de Broglie wavelength of a thermalised positron at room temperature (300K) is 62Å. If such a positron is then emitted by a material with a negative work function it will gain energy as it is emitted into the vacuum, which will lower the de Broglie wavelength. A gain of only 1eV will reduce the wavelength to 12Å. This means that the positronic wavevector will be mismatched at the surface boundary and so reflection may occur. If the temperature of the solid in which the positron is thermalised is reduced the energy gain results in an increasing mismatch between the wavevectors, and thus the probability of reflection increases. A positron that is reflected may return to the surface again and so any model of this process should include multiple encounters (see, for example, Jacobsen and Lynn 1996 or Britton et al 1989).
In metals with a positive work function, reflection may still occur. Then the positron will experience a potential step due to the surface well, the size of this step being the difference between the depth of the well and the positron work function. In both cases (positive and negative) it is possible for the positron to undergo one of the emission processes described above. Note that positrons that are not thermalised (epithermal positrons) may also take part in quantum mechanical reflection, but with a much reduced probability.

1.3.2.c Work function emission

The fact that some metals have negative work functions has implications for the reemission of positrons implanted into such metals, and therefore for the process of moderation. The work function of a material is defined as the energy needed to remove a particle from a point just inside the surface of that material to a point just outside the surface. The electron work function ϕ_- has been expressed by Lang and Kohn (1970) as the difference between the surface dipole, D, and the bulk chemical potential, μ_- thus;

$$\phi_- = D - \mu_- \qquad (1.12a).$$

Similarly, the positron work function, ϕ_+, is expressed as (Tong 1972)

$$\phi_+ = -D - \mu_+ \qquad (1.12b).$$

Here the dipole contribution is of the same magnitude as for electrons but opposite in sign. The positron chemical potential includes repulsion from the ion cores and attraction to the conduction electrons. For electrons, the chemical potential is considered to be the Fermi energy but this is not the case for positrons since only one positron is considered to be in the metal at any one time. Tong (1972) also realised that the surface dipole could be larger in magnitude than the positron chemical potential and so the positron work function could therefore be negative. The possible spontaneous emission of free positrons from such materials led to the use of metals with negative work functions as moderators, most notably tungsten. (See table 1.1 and Schultz and Lynn 1988 for a history of moderators). Electron work functions are always positive due to the additive nature of the terms in (1.12a).

The maximum kinetic energy of a positron emitted from a negative work function material is the value of the work function itself, as well as a component of thermal energy, which is generally small compared with the work function energy. The positron can lose some of this energy in the emission process by exciting electron-hole pairs, since it is highly correlated with the conduction electrons. Some energy loss can also occur via phonon scattering at the surface. The energy gained by work function emission leads to a velocity perpendicular to the emitting surface. The thermal motion is in all directions and will have a mean energy of kT/2 in the direction parallel to the surface. This means that the angular distribution of work function positrons will be highly forward peaked with a thermal spread. This angular spread θ will be given by

$$\theta = \tan^{-1}\left[\frac{kT}{\phi_+}\right]^{1/2} \qquad (1.13).$$

This does not include any of the possible energy loss mechanisms described above. If these processes occur, or if energy is lost by interactions with defects or impurities, the angular spread may be further increased.

The slow positron yield is expected to increase with the work function (Murray and Mills, 1980, Gullikson et al, 1988) for a particular metal. It is thought that, for a slow positron escaping from a metal positronium formation is usually energetically more favourable than the bare positron emission. However, if the work function magnitude is increased the

positron moves faster and so the interaction time with an electron is decreased, along with the probability of positronium formation. Since the emission of free positrons is in competition with positronium formation the former is expected to increase as the latter decreases. The experiment of Murray and Mills (1980) observed this by heating samples of copper and aluminium and then measuring the reemission of positrons at different sample temperatures, and hence (slightly) different work functions.

1.3.2d Positronium formation at surfaces

Since positronium cannot be formed inside the bulk of conductors or semiconductors the concept of a positronium work function is redundant when considering these materials. Instead we may think of a formation potential, ε_{Ps}, by considering the energetics of surface positronium formation. Conservation of energy yields a potential of this nature of

$$\varepsilon_{Ps} = \phi_- + \phi_+ - \frac{R_\infty}{2} \qquad (1.14),$$

where the binding energy of positronium in vacuum ($R_\infty / 2$) = 6.8 eV is large compared to most work functions. This means that ε_{Ps} is often negative and so positronium formation is one of the main branches for positrons which have diffused back to metal surfaces (see sections 2.6, 3.2 & 3.3). For those materials in which positronium may be formed (i.e. insulators, see section 1.3.1d and 3.2) it does make sense to define a positronium work function. The binding energy of positronium in a solid is less than that in vacuum (see section 1.3.1d) due to a repulsive exchange interaction between the electron in the positronium atom and the (bound) electrons in the medium. This difference in binding energies gives rise to a negative positronium work function of

$$\phi_{Ps} = -\mu_{Ps} + E_B - \frac{R_\infty}{2} \qquad (1.15),$$

where E_B is the binding energy of positronium inside the solid and μ_{Ps} is the positronium chemical potential. Thus, the energy required to move a positronium atom from a point just inside the surface to a point just outside is ϕ_{Ps}. This work function may also be thought of as the energy required to break up the positronium atom in the solid and then remove both components to outside the surface, less the energy gained from reforming the atom outside. That is,

$$\phi_{Ps} = \phi_+ + \phi_- + E_B - \frac{R_\infty}{2} \qquad (1.16),$$

which tells us that the positronium chemical potential is the sum of the electron and positron chemical potentials (see equations 1.12a and b). These negative positronium work functions are important in the formation of positronium in the metal oxide targets used in this thesis (see sections 3.2 and 3.3).

1.3.3 Moderators

We define moderation as the process by which one takes a distribution of β^+ particles, which will invariably have a very large energy spread (see figure 1.7), and produces from this a low energy quasi-monoenergetic beam of positrons. There are many difficulties associated with this and, despite the previous recognition of the need for such a beam, the first experimental observation of moderated positrons was not until 1958 (Cherry 1958) with an efficiency of $\sim 10^{-8}$. See table 1.1 for a list of the notable advances in moderator efficiency. Note that Madanski and Rasetti (1950) did make attempts to moderate β^+ particles in essentially the same manner as described, but without success. Most of the salient physical processes involved in moderation have been discussed above. Essentially, the process involves the implantation of high energy β^+ particles into a material (the moderator). These particles then thermalise and diffuse. Those that reach the surface of the material and are emitted as free positrons constitute the slow positron beam and will typically be electrostatically accelerated to some desired energy. It is of course possible to obtain a monoenergetic positron flux by applying a velocity selector to the β^+ spectrum. Figure 1.7 shows the energy distribution of a spectrum from a ^{58}Co source and the effect of moderation. Clearly the use of a moderator will produce a greater slow positron flux than a velocity selector.

Moderator and Geometry	Efficiency	Energy Width ΔE (eV)	Vacuum (Torr)	Reference
Pt, K, Ga, Glass Transmission	0	N/A	N/A	Madanski and Rasetti, 1950
Cr plated Mica Transmission	$3x10^{-8}$	–	10^{-7}	Cherry, 1958
Au plated mica Transmission	10^{-7}	2	10^{-7}	Costello et al, 1972
Mgo coated Au vanes Backscattering	$3x10^{-5}$	2.3	10^{-6}	Canter et al 1972
B Self moderator	10^{-7}	0.15	10^{-7}	Stein et al 1974
Al(100) Backscattering	$3x10^{-5}$	0.1	10^{-10}	Mills 1978
Cu(111)+S Backscattering	$9x10^{-4}$	0.3	10^{-10}	Mills 1979
Cu(111)+H_2S Backscattering	$1.5x10^{-3}$	0.6	10^{-10}	Mills 1980
W Vanes Backscattering	$7x10^{-4}$	1.3	10^{-7}	Dale et al1980
W(110) Backscattering	$3x10^{-3}$	0.7	10^{-10}	Vehanen et al 1983
W(100) Transmission	$4x10^{-4}$	3	10^{-10}	Lynn et al 1985
Ne Transmission	$7x10^{-3}$	0.58	10^{-10}	Mills and Gullikson 1986
W(100) Ni(100) Transmission	$9x10^{-4}$ $6.6x10^{-4}$	–	10^{-8} 10^{-8}	Gramsch et al 1987
W, Ni Cone Backscattering	$1.5x10^{-3}$ $1.0x10^{-3}$	7	10^{-7}	Lynn et al 1989
Ar, Kr Cup Field assisted transmission.	$6x10^{-3}$ $6x10^{-3}$	–	10^{-9}	Merrison et al 1992

Table 1.1 A summary of the historical development of moderators.

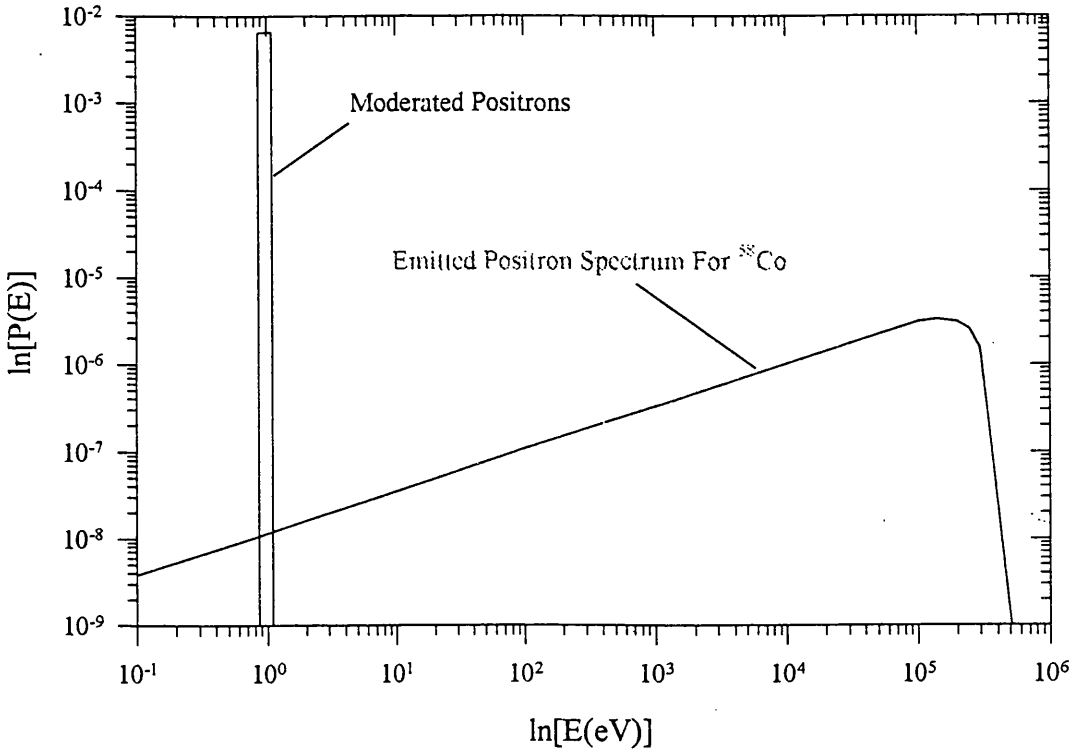

Figure 1.7. The energy distribution of positrons emitted from a W(110) moderator compared with the original β^+ spectrum emitted from a ^{58}Co source (Schultz and Lynn 1988).

P(E) = Positron Yield

The intrinsic efficiency of a moderator is not the only factor which determines the final conversion efficiency. The geometry employed can allow more of the initial β^+ particles to take place in the moderation process and thus increase the final slow positron yield. Some different moderator geometries are shown in figure 1.8.

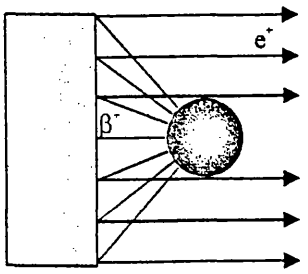

(a) Backscattering

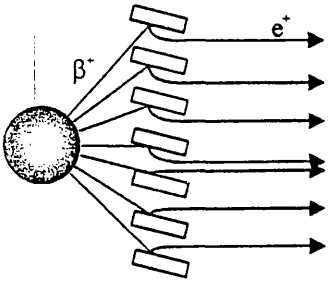

(b) Vane

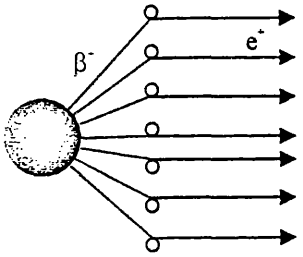

(c) Grid

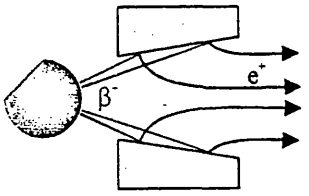

(d) Cone

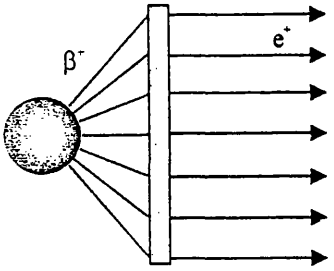

(e) Transmission

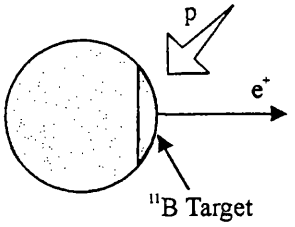

(f) Self-Moderation

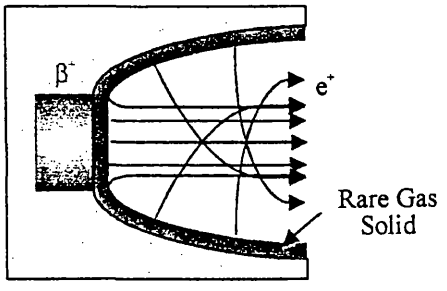

(g) Cup

Figure1.8. Various moderator geometries. (Garner 1997)

The moderator geometries shown in figure 1.8 a-e are typical tungsten geometries. (Tungsten is by far the most common moderater, with various arrangements in use). (a) is not very common since it requires a small source (so that the beam is not blocked or too highly shadowed by the source) which are no longer commercially available. The arrangements shown in (b-e) are still in use, with (c) or (e) being almost the standard method. This is because there is very little difference in the final conversion yield, and (c) and (e) are very easy to implement.

When tungsten, or indeed any metal, is used as a moderator in this way it is desirable that it be as clean and free of defects as possible. This means that such materials must be annealed before use. Thus, metals must be heated to a temperature sufficiently high to allow the metallic structure to reorganise itself into a defect-free form and to desorb any impurities. In addition to this the surface will also be cleaned which, as we have seen, is important in the emission of slow positrons. This heating should be done in an environment with the lowest possible pressure and preferably in-situ. It is possible to anneal tungsten moderators and then transport them through air to a separate system. Although this does reduce the overall efficiency, largely via surface contamination, it does not appear to do so to an undue extent.

Tungsten is a very durable material and may function as a moderator with a useful efficiency after a variety of preparations. It is this ease of use, combined with a relatively high efficiency (due to the large negative work function) that makes tungsten so popular. See section 2.1 for a discussion of the practicalities of annealing tungsten samples.

The rare gas solid (RGS) moderators are currently the most efficient known. There are technical difficulties associated with the use of such moderators, in particular Ne, since low temperature cryostats must be employed. The energy and angular spread of RGS moderators can be quite high due to epithermal positron emission (because of the relatively slow energy loss mechanisms, see section 1.3.1b). Also, the wide cup design common when cryostats are used may introduce further beam divergences (see figure 1.8g). The choice of moderator may ultimately depend on the application of the final beam.

1.3.4 Magnetic beam transport

A magnetically guided beam confines positrons (typically produced from some moderator arrangement and then accelerated to the desired energy) laterally by a field which is usually generated by a set of coils outside the vacuum chamber. Because the coils are located externally, the beam may be easily steered by adjusting their orientation (see figure 2.3 for a schematic of the magnetic beam used in this work). Many magnetic beam lines make use of a so-called Wien filter (e.g. Hutchins 1986) which consists of a pair of concentric plates across which a radial electric field is maintained. This field is orientated such that it acts perpendicular to the magnetic field. The resulting Lorentz force on the positrons passing through this region causes a drift velocity perpendicular to the electric and magnetic fields which has a magnitude of E/B, where E and B are the magnitudes of the electric and magnetic fields respectively. Since the transverse velocity of the beam is not affected by this process, positrons with different energies experience different degrees of deflection (depending on how long they spend in the deflection region). This apparatus can therefore be used as a velocity or energy filter (for particles with the same mass). Wien filters are also used to prevent backscattered or reemitted particles from returning to a scattering or emission site where they may be misinterpreted as primary particles. Details of magnetic beams will be described in more detail in chapter 2 since one was used in the experimental work discussed in this thesis.

1.4 Antihydrogen

1.4.1 Introduction to antihydrogen

In this section we shall consider the experimental prospects for the formation of low energy antihydrogen. Antihydrogen has, so far, only ever been deliberately produced in the laboratory twice (Baur et al 1997, Blanford et al 1998) and only at relativistic energies. The motivation for the production of antihydrogen is primarily the provision of stringent tests of fundamental physics, namely CPT invariance and the weak equivalence principle (WEP) (See, for example, Charlton et al 1994).

It is envisaged that such tests will be performed via spectroscopic analysis of antihydrogen, and this necessitates the use of trapped antiatoms. It is also envisaged that the neutral antiatoms produced will be trapped by a magnetic gradient trap and these require very strong magnetic field gradients. Using current magnet technology the highest field gradients that can be produced are of the order of a few Tcm^{-1}, which is sufficient to trap antihydrogen atoms with temperatures less than 1K only. Relativistic antihydrogen, in the context described here, does not lend itself to precision spectroscopy and so only techniques for the production of low energy antihydrogen are considered.

Difficulties in antihydrogen production begin with the collection of the constituent particles, i.e., positrons and antiprotons. The production of slow positrons was described previously and in this section we shall consider the utilisation of such techniques for antihydrogen creation. Antiprotons present some new challenges which arise from the fact that the primary sources of these particles require large accelerators. Although antiprotons are routinely produced at such facilities, the scale of these machines means that the use of antiprotons is not widespread, and so experimental antiproton physics is entirely dependent on just a few laboratories. This does not mean, however, that there are insufficient resources for the present purposes, although this situation did (temporarily) present itself with the closure of the low energy antiproton ring (LEAR) at CERN at the end of 1996. We shall discuss the production of low energy antiprotons, from both LEAR, and its successor the antiproton decelerator (AD), which is expected to be operational during 1999.

In addition to collecting positrons and antiprotons it is also necessary to cause them to interact and form antihydrogen. A number of techniques have been proposed to accomplish this (see Charlton et al 1994 for a summary), some of which will be considered in this section. We shall pay particular attention to the reaction of antiprotons with positronium since a Monte Carlo simulation of this reaction constitutes a major part of this thesis (see chapter 4). We shall, in this area, focus primarily on the antiproton trap in use by the ATHENA group, which is a collaboration of more than 50 scientists working to create low energy antihydrogen. (ATHENA is a contrived acronym derived from **Appara**T**us** for **H**igh precision **E**xperiments with **N**eutral **A**ntimatter, or **An**T**i**H**ydrog**EN** **A**pparatus).

Once antihydrogen has been formed the problem is then to trap it and perform the spectroscopic analysis which motivates these efforts. Some of the problems associated with doing so will be discussed here, as well as the aspects of CPT and WEP that may be tested with antihydrogen.

1.4.2 The components of Antihydrogen.

1.4.2a Antiproton production

We have seen that the most common source of positrons for use in physics experiments are radioisotopes which emit fast β–particles as they decay. Antiprotons are not emitted in this way since they are hadrons and therefore interact via the strong force. This will dominate the weak force responsible for radioactive decay and so there is no process of antiproton production analogous with β–decay. The most common technique used to produce antiprotons is the so-called "beam-target method" which simply involves directing an intense proton beam at a conversion target, which is usually a heavy material such as tungsten or iridium. The resulting antiprotons are then collected in a large acceptance channel (large in momentum spread and geometric beam size). The primary proton beam energy must be above the threshold for antiproton production (~6 GeV, Möhl 1997) and is typically in the range 20-200 GeV, for reasons we shall discuss later. Figure 1.9 is a representation of the production of antiprotons as described above.

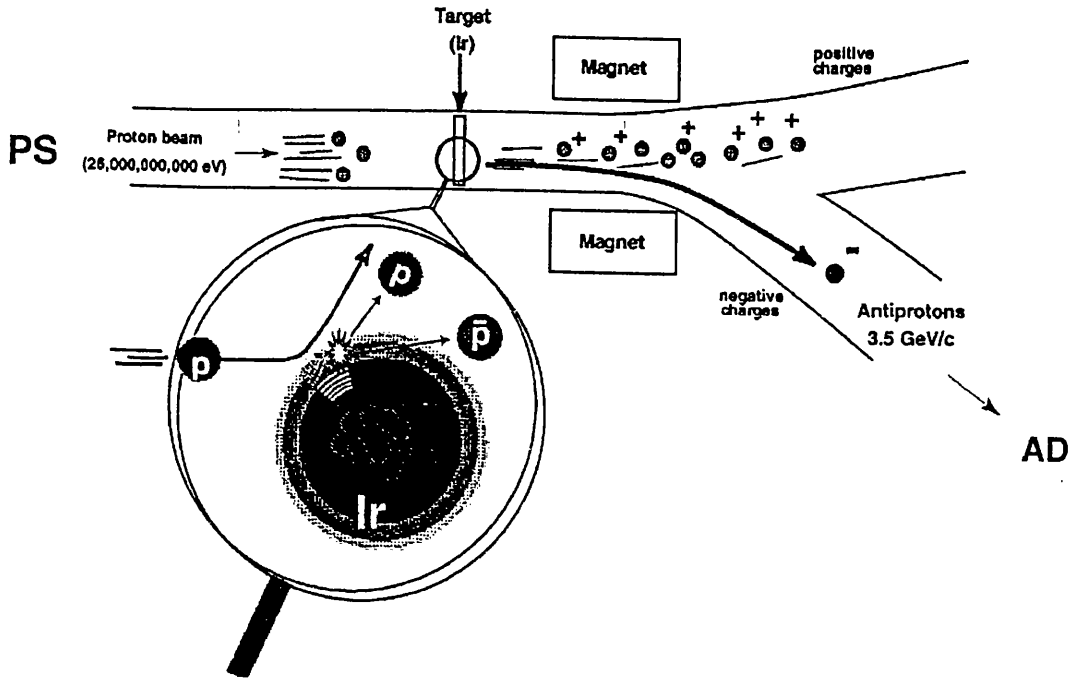

Figure 1.9 The principle of antiproton production in the AD (Landau, downloaded from the ATHENA website: www.CERN.ch/athena/public/pictures.html)

The antiprotons are primarily created via the mechanism

$$p + p \rightarrow p + p + p + \bar{p} \quad (1.17).$$

As the energy of the primary proton beam is increased the possibility of a proton-proton interaction such as in (1.17) is similarly increased. It would, therefore, seem advantageous to use the highest possible primary beam energy to obtain the maximum antiproton yield. However, the difficulties associated with using very high energy proton beams must be considered. Target heating means that the intensity must be reduced with increasing energy so, although the chances of a given proton taking part in the reaction (1.17) increase, there will be less protons to do so. Also, the production of a high energy proton beam is itself a nontrivial task and becomes increasingly expensive at higher energies.

The momentum of the antiprotons will be spread over a range, determined by the reaction kinematics, which will present an optimum momentum collection window. The upper and lower limits of this window will increase with proton beam energy and so the resulting

antiproton collection will have to operate at a higher energy, which means that the large acceptance required is more difficult to arrange. As well as this, if the antiproton energy is too high it will be difficult to cool them for later storage.

With these considerations in mind, the production of antiprotons at CERN for use in LEAR is accomplished with a primary proton beam momentum of 26GeV/c. The optimum antiproton collection momentum is then 4GeV/c, although antiproton collection takes place at 3.5GeV/c to aid later cooling. The primary proton beam used at Fermilab has a momentum of 120 GeV/c, with virtually the same antiproton yield and an optimum collection momentum of 9GeV/c. This arrangement is more suitable for collision experiments. Some of the characteristics of the arrangements at CERN and Fermilab (the two leading sources of antiprotons) are listed in table 1.2, which is taken from Möhl (1997).

Machine	CERN (AC)	Fermilab (Debuncher)
Proton beam momentum (GeV/c)	26	120
Optimum antiproton collection momentum (GeV/c)	3.5	9
Production cross-section [(srGeV/c)$^{-1}$]	0.013	0.25
Acceptances A_h (π mm rad) A_v (π mm rad) $\Delta p/p$ (10^{-3}) $\sqrt{A_H A_v}\,\Delta p / p$ (π mm rad)^2	200 200 60 12x10^3	25 25 40 1x10^3
Yield ($\bar{p}/p$)	3.5x10^{-6}	14x10^{-6}
Protons per pulse	1.5x10^{13}	0.5x10^{13}
Antiprotons per pulse	5x10^7	7x10^7

Table 1.2 Comparison of some of the characteristics of the CERN antiproton collector and the Fermilab debuncher. A_h and A_v are the horizontal and vertical acceptances respectively.

So, antiprotons with momentum 3.5 GeV/c are produced by the antiproton collector (AC) with the parameters listed in table 1.2. After this they are accumulated and further cooled in the antiproton accumulator (AA). A bunch of ~10^9 antiprotons may then be removed from the accumulator and injected into the proton synchrotron (PS) where it is decelerated (and cooled) to 0.6 GeV/c. Finally this pulse is transferred to LEAR where alternate cooling and deceleration stages reduce the pulse momentum to 100MeV/c. The cooling at each stage of deceleration (see below) is necessary to reduce the increase in phase space volume following deceleration. At high energies this will be stochastic cooling, while electron cooling, which is more efficient, is used in the lower energy stages of LEAR.

The output from LEAR is still too energetic to allow capture in a Penning trap (see section 1.4.2b) so a degrading foil is used to further reduce the beam energy. Also, the trap and the LEAR output beamline are physically disconnected and further moderation of the antiprotons may be achieved by increasing the air gap between them. Energies of < 50 keV (compared to 5.9 MeV from LEAR) are obtained in this way. The antiprotons which pass through the moderating gap/foil are then confined in the trap arrangement by a large magnetic field (~3 T) and endcap electrodes. Antiprotons with kinetic energies less than the electrode voltage are reflected back towards the entrance foil, the voltage of which is ramped up to prevent their escape. (Note that this process is only possible because the antiprotons are delivered in pulses). The trapping mechanism is explained in more detail below. Once trapped, electron cooling reduces the antiproton energy to thermal levels (the ambient temperature of the trap is cryogenic, ~4.2 K). This process is illustrated in table 1.3 which is a history of antiproton cooling from MeV to meV energies. Note that the antiproton yield from the conversion target depends on the AC acceptances and the primary proton beam. The yield in table 1.3 corresponds to the AC parameters in table 1.2

Decelerating stage	Momentum/Energy GeV/c / keV	Cooling	Antiprotons per pulse
Production at conversion target and collection in AC	$3.5/6.5x10^6$	_	$5x10^7$
Accumulator (AA)	$3.5/6.5x10^6$	Stochastic	$\sim10^9$
Proton Synchrotron (PS)	$0.6/2x10^3$	Stochastic	$\sim10^9$
Low energy antiproton ring (LEAR)	$0.1/5x10^3$	Stochastic Electron (beam)	$\sim10^8$
Moderating Air gap/foil arrangement	0.009/ <50	_	10^6
Penning Trap	Thermal	Electron (cloud)	10^6

Table 1.3. The use of LEAR in the slowing down of high energy antiprotons to thermal energies and subsequent capture in a Penning trap. No considerations are made for possible stacking of bunches other than in the AA stage.

Beam cooling is an important factor in the production of low energy antihydrogen. The process of stochastic cooling is technically very challenging, but the basic principle is fairly simple. If a particle, or an ensemble of particles circulates in a storage ring it/they will perform betatron oscillations about the central axis of the ring. (In storage rings the magnetic fields are designed to vary azimuthally, repeating in a cyclic fashion, and so the cyclotron orbits are no longer circular. Oscillations in the radial and axial directions around this new orbit are known as betatron oscillations). The nature of these oscillations depends on the precise focusing arrangement in use. As the beam travels around the ring its detailed form (that is, the shape of the beam in phase space) is observed by pick-up electrodes and a signal is constructed which is fed back to a "kicker". This signal provides a deflection which reduces the average betatron amplitudes and energy spread, thus cooling the beam in phase space. Since the beam will typically be moving at a speed close to that of light, the signal to the kicker takes a short cut across the ring so that it arrives at the kicker as the same time as the beam. If only one particle is in the ring this process is fairly simple but, in a real beam, fluctuations about a mean must be detected and the process is highly complex.

The basic principle of electron cooling is also quite simple. A high current electron gun is used to produce a monoenergetic electron beam which is velocity matched to the antiproton beam and injected into the storage ring so that the two beams travel together over part of

ring. The antiproton beam is then cooled in phase space as the electrons absorb transverse energy and momentum via Coulomb interactions. The cooling may be enhanced if a longitudinal magnetic field is applied such that the heavy particles (antiprotons) are largely unaffected but the electrons orbit the field lines with a small cyclotron radius. Stochastic cooling is preferred as the initial cooling process because it is difficult to obtain high current electron beams above a few tens of keV, and cooling times increase since the time spent in the section of the ring where electrons are present is reduced.

In response to the decision to close LEAR a proposal was made to adapt the antiproton collector, mentioned above, such that it may be used itself as an antiproton cooler and decelerator ring. To do so would incur less operating costs than the previous arrangement where four machines (PS, AC, AA and LEAR) are used to provide low energy antiprotons. In addition to this, much of the equipment from that arrangement can be used in the new arrangement, known as the antiproton decelerator, thus further reducing the cost (for example, the LEAR electron cooling device will be transferred to the AD with only minor modifications).

The primary production of antiprotons remains as in LEAR (that is, beam target production from protons supplied by the PS) and these are injected at 3.57GeV/c into the AD. They are then decelerated and stochastically cooled in alternating steps to 300MeV/c, after which electron cooling is employed. The beam characteristics are shown in table 1.4 which is taken from Maury (1997).

P [GeV/c]	ε_i [π mm mrad]	ε_f [π mm mrad]	$\Delta p/p_i$ (%)	$\Delta p/p_f$ (%)	Time [s]	Cooling Process
3.5	200	5	1.5	0.1	20	stochastic
2.0	9	5	0.18	0.03	15	stochastic
0.3	33	2	0.2	0.1	6	electron
0.1	6	1	0.3	0.01	1	electron

Table 1.4. The transverse emittences and momentum spread before (i) and after (f) cooling and cooling times. Only adiabatic cooling due to deceleration is considered. From Maury (1997).

The initial pulse of antiprotons at 3.5GeV/c contains around $5x10^7$ particles, around a quarter of which are available at low energy. It is expected that these pulses of $1.2x10^7$ antiprotons at 100 MeV/c will be available every minute or so in pulses 200-500 ns long. These may be stacked in groups of 10 production cycles if the PS beam is synchronised with the ejection cycle.

1.4.2b Antiproton trapping

The final stage of slowing down of the antiprotons takes place as they are injected into the Penning trap arrangement briefly mentioned above. A schematic illustration of a Penning trap is shown in figure 1.10.

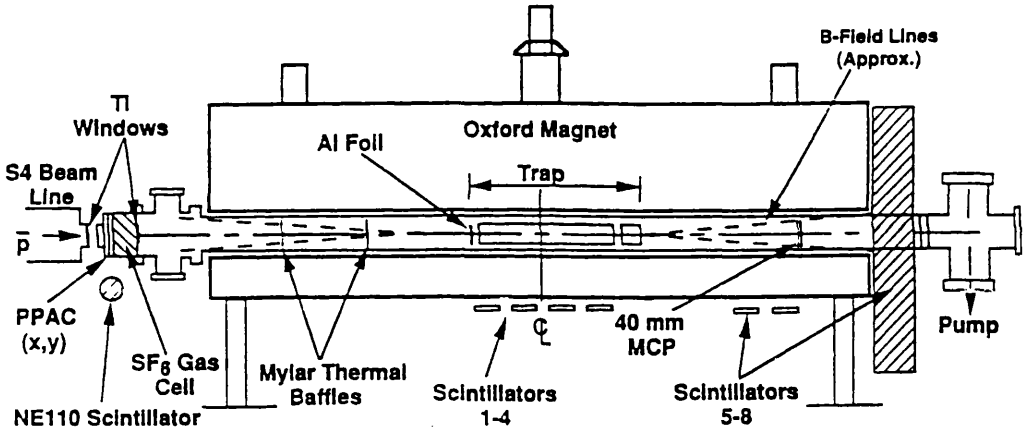

Fig(1.10) A schematic of the antiproton trap. The last stage of slowing down is the aluminium foil which is rapidly ramped up to 12.5 kV once the pulse has passed through. This, combined with the large axial magnetic field and other electrodes traps antiprotons with energies less than 12.5 keV (From Feng et al 1997)

Antiprotons (from LEAR or the AD) delivered at an energy around 5 MeV enter the trap from the left. LEAR bunches may typically contain 10^8 antiprotons, while the AD bunches are expected to contain at least $1x10^7$. These bunches, typically ~200 ns long, enter and pass through a titanium window, which reduces the energy. The superconducting magnet generates a field of ~3 T and this acts as a lens which can be made to focus a particular beam energy at a particular point, chosen to be the back of the aluminium degrading foil. The foil thickness is chosen so that the maximum number of low energy antiprotons are

transmitted (1-2% with below 30 keV). These particles are radially confined by the axial magnetic field and are reflected back towards the entrance electrode by the potential at the far end of the trap if they are of a sufficiently low energy. Then, if the potential on the entrance electrode is ramped up before the reflected pulse reaches it, the antiprotons will be trapped. Since there are technical limitations to how fast this voltage can be applied, the trap must be at least 50cm long to capture the burst below ~15 keV. The electric field confines the particles along the trap axis. Unless particles gain energy by collisions and escape from the trap (which is very unlikely), confinement is unlimited and antiprotons have, after cooling, been stored for months (Gabrielse et al 1990).

The stored antiprotons are still too energetic for antihydrogen synthesis and must be further cooled. This is achieved by electron cooling. Around 10^9 electrons are pre-loaded and cooled, via the emission of synchrotron radiation, in the trap before antiprotons are injected. After this injection, they interact with the thermalised electrons and are cooled to the ambient cryogenic temperature in a few minutes, after which long term storage can occur.

1.4.2c Positron accumulation and storage

The production and manipulation of positrons has been discussed previously. In this section we consider the accumulation of positrons in a trap, which may be of use in some methods of antihydrogen production. The most efficient trapping method for positrons is the buffer gas technique due to Surko and co-workers (Murphy and Surko 1992, Greaves et al 1994). This Surko trap has accumulated $1x10^8$ positrons in a three minute cycle and is orders of magnitude more efficient than other methods (Surko et al 1997 and references therein). The basic principle of the Surko trap is illustrated in fig 1.11. Slow positrons from a conventional beamline enter the trap and pass an electrostatic entrance potential just below the energy of the incident beam. They then encounter N_2 gas in the chamber at various pressures, maintained by differential pumping. As the positrons pass through regions I , II and III they may lose energy by electronic excitation of the gas molecules. At the end of the chamber another potential reflects them back to the entrance potential and, if enough energy has been lost before they reach this, they may be confined along the trap axis.

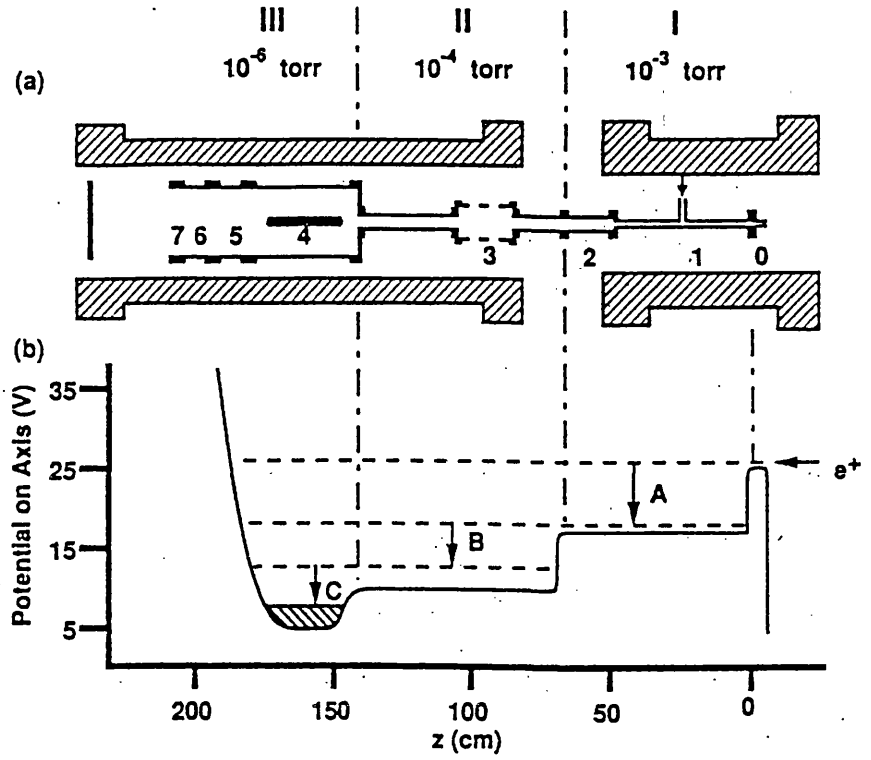

Figure 1.11. Surko trap/accumulator schematic showing different pressure and potential regions. (Holzscheiter and Charlton 1998)

An axial magnetic field of ~0.2 T confines the particles axially. The trapped positrons can lose further energy by exciting vibrational and rotational modes of the N_2 molecules and will eventually end up in region III. Positrons may be continuously accumulated in this manner.

To use such a technique for the production of antihydrogen, where UHV conditions are necessary, the accumulated positrons must be transferred into a separate UHV stage. This may be accomplished by accumulating as many positrons as desired and then switching of the buffer gas supply. The trap may then be pumped out to a base pressure and then the particles transferred to an isolated UHV system from which transfer to the antiproton trap can take place. It is expected that at least $5x10^8$ positrons may be transferred every 3 minutes in this way (Surko et al 1997).

1.4.3 Combining positrons and antiprotons

A number of reaction schemes to produce antihydrogen are possible (see, for example, Charlton et al 1994) and in this section we shall consider only the positronium-antiproton reaction,

$$\bar{p} + Ps \rightarrow \bar{H} + e^- \qquad (1.18)$$

since this is connected with this thesis. Some other reactions are:

Radiative recombination: $\bar{p} + e^+ \rightarrow \bar{H} + h\nu$ (1.19)

This reaction has a very low cross section, although this may be increased by laser stimulation: $\bar{p} + e^+ + mh\nu \rightarrow \bar{H} + (m+1)h\nu$. (1.20)

Three body recombination: $\bar{p} + e^+ + e^+ \rightarrow \bar{H} + e^+$ (1.21)

Reaction (1.18) has a relatively large cross section (~10^{-15} cm^2) which may be enhanced by using excited state positronium. We shall consider only ground state positronium in accordance with later work in this thesis. The cross section for (1.18) is derived from the application of charge conjugation and time reversal to calculations of positronium formation in collisions between atomic hydrogen and positrons. The total formation cross sections (as well as some differential cross sections) for the first three states of antihydrogen may be found in Chapter 4. The charge conjugate of (1.18) has been observed (Merrison et al, 1997) with the cross sections consistent with calculations.

1.4.4 Antihydrogen and tests of fundamental physics

1.4.4a Trapping antihydrogen

The trapping of antihydrogen gives rise to difficulties that do not occur with charged particles. If, as we envisage, antihydrogen is created in a Penning trap by positronium impact on antiprotons, then as soon as an atom is formed it will no longer be trapped and will rapidly escape from the trap and annihilate. It is necessary, therefore, to impose additional non charge-dependent confinement of the antiatoms. This is achieved by the superposition of an inhomogeneous magnetic field across the Penning trap fields.

The application of such a field results in confinement because the antihydrogen atoms possess a magnetic moment which has a potential energy in a field **B** of $-\mu\mathbf{B}$ (where μ is effectively the positron magnetic moment). If the magnetic moment is antiparallel to the magnetic field the atom will move towards the field minimum where its energy is lowest, and conversely atoms with parallel moments will move to the field maximum. Thus, if an inhomogeneous magnetic field has minima in three dimensions, atoms with antiparallel magnetic moments will be confined. These atoms are known as low field seekers (and their opposites as high field seekers). Since the high and low field seekers are degenerate in energy in the absence of a magnetic field, the field minima are designed to be non-zero to prevent spontaneous transitions which may result in a reduced yield of trapped atoms. The trap configuration which will be used is known as an Ioffe-Pritchard trap (Pritchard 1983) and typically achieves a depth sufficient to trap atoms of 1K or less. Thus, of the antihydrogen atoms created only low field seekers (50%) with temperatures less than 1K (1%, see section 4.6) can be trapped.

1.4.4b Spectroscopy of antihydrogen

It is expected that the spectroscopic properties of antihydrogen are very similar or identical to those of hydrogen, and therefore the techniques of high precision hydrogen spectroscopy must be used to perform analyses of trapped antihydrogen. There will, however, be far less atoms than is usual and the strong fields present are likely to exacerbate Zeeman and Doppler effects, so further technical difficulties are expected.

Anithydrogen atoms in the magnetic gradient trap mentioned above will still have temperatures ranging up to 1K. In order to perform the highest precision measurements these temperatures must be reduced to mK levels. The usual cooling method of evaporation is not available with such low densities and so laser cooling must be employed. In this process a laser is directed towards the atoms at a frequency slightly detuned from a resonance transition. Then, if the atom is moving, say, towards the laser the Doppler shift cancels out the detuning and a photon is absorbed and then reradiated. However, the reradiated photons are emitted isotropically while the absorbed photons all come from the same direction. There is thus a net loss of momentum for the atom, and hence it is cooled,

in the direction of the laser. Since the atoms are trapped only one laser is required to reduce the absolute temperature. In practice this is very difficult to achieve and initial experiments are likely to be performed without such cooling.

Atomic energy levels may be observed by exciting electrons (or, in this case, positrons) from one state to another and observing the photons emitted as they spontaneously de-excite. The transition from 1S to the metastable (lifetime 0.125s) 2S state has a linewidth, due to the long life of the 2S state, of only ~1Hz and, since the transition frequency is $\sim 1 \times 10^{15}$ Hz accurate measurement of this transition offers a precision level of 1 part in 10^{15}.

1.4.4c Antihydrogen, CPT and the WEP

Before going to enormous lengths to create, trap and interrogate atomic antihydrogen it is natural to consider the potential information that may be so obtained. We shall consider here the tests of the CPT theorem and of the weak equivalence principle.

The CPT theorem states that a quantum field theory must remain invariant under the combined operations of charge conjugation (C) parity (P) and time (T) reversal (See e.g. Charlton et al 1994 and references therein). This means that that the combined operations

$$\begin{aligned} q &\rightarrow -q \\ x &\rightarrow -x \\ t &\rightarrow -t \end{aligned} \qquad (1.22)$$

(a simplified representation of the C, P and T operators) should be an invariant in any quantum theory when q is charge, x represents space and t time. Charge conjugation is not necessarily restricted to electric charge. It may represent baryonic, leptonic...(see for example, Itzykson and Zuber, 1980) etc "charge", and so this invariance implies that matter and antimatter behave symmetrically. In particular, the entire theorem thus implies that matter and antimatter have equal masses and lifetimes (these properties are not affected by 1.22), and equal and opposite electric charges and magnetic moments. The energy levels of bound systems of matter and antimatter must therefore be identical, at all levels of structure, and it is this prediction that will be tested by the spectroscopic analysis of antihydrogen compared to hydrogen.

Another cornerstone of modern physics is the general theory of relativity (GTR). An important principle of GTR is the WEP which states that all bodies in a gravitational field experience the same acceleration. A simple way of describing this principle is to consider the acceleration due to gravity of a falling body on Earth. The Newtonian force (F) experienced by such a body of mass (m_g) is given by

$$F = \frac{GM_E m_g}{r^2} \qquad (1.23).$$

Where G is the gravitational constant, M_E is the mass of the Earth and r the separation of the body and the centre of mass of the Earth. The acceleration, a, of such a body is given by Newton's second law of motion

$$a = \frac{F}{m_i} \qquad (1.24).$$

Now, the mass of the body in (1.24) is written as m_i and is the inertial mass, which defines the response of the body to the application of a force. The mass in (1.23) is the gravitational mass which defines the way in which two masses couple via gravitation. Since the WEP states that all bodies have the same gravitational acceleration the WEP may be stated as

$$m_g = m_i \qquad (1.25).$$

This may seem trivial but, since m_g refers to the interaction of matter with gravity and m_i refers to the acceleration of matter in response to any force, a deeper implication is that gravitational fields are equivalent to accelerations. This is the essence of the WEP. The principle is referred to as weak because it is only applied to mechanical quantities. The Einstein equivalence principle (EEP) includes the WEP and also all other non-gravitational phenomena.

The WEP has been shown to be true to an accuracy of 1 part in 10^{12} by the experiments similar to those of Eötvös et al (1922) in which the gravitational accelerations of a variety of different materials were measured and found to be the same to the precision quoted above. There has been no experimental test of the WEP for antimatter. Directly measuring the gravitational acceleration of charged particles is extremely difficult because of the need to shield out all stray electric fields, which would otherwise dominate the gravitational forces acting on the particles. This problem is avoided using antihydrogen, but the technical

challenge of such a measurement remains daunting. To measure a cloud of atoms in free fall one must adopt a statistical approach, and the low number of antihydrogen atoms likely to be available would provide poor statistics. Direct measurements of this nature are not likely to provide any useful data.

However, again the 1S-2S transition may be used as a test. It can be shown (Hughes and Holzscheiter 1992) that for a transition frequency $\bar{\omega}$ (1S-2S) for antihydrogen, and ω(1S-2S) for hydrogen then,

$$\frac{\bar{\omega}(1S-2S)-\omega(1S-2S)}{\omega(1S-2S)} = 3(\alpha_g - 1)\frac{U}{c^2} \qquad (1.43)$$

Where U is the gravitational potential and α_g is a coupling parameter between antimatter and the gravitational field. (This may be thought of as a measure of the difference in gravitational acceleration for antimatter compared to matter, so that if matter experiences a gravitational acceleration a, then antimatter will experience an acceleration of $\bar{a} = a\alpha_g$).

So, if the gravitational potential, U, is changed by an amount ΔU, any change in the transition frequencies of hydrogen or antihydrogen as a result, as in,

$$\frac{\Delta\bar{\omega}(1S-2S)-\Delta\omega(1S-2S)}{\omega(1S-2S)} = 3(\alpha_g - 1)\frac{\Delta U}{c^2} \qquad (1.44)$$

would indicate a violation of WEP by antihydrogen (Hughes and Holzscheiter 1992). To achieve a large change in potential difference one could measure the transition frequencies at different times of the year since the eccentricity of the earth's orbit causes the solar gravitational potential at the surface of the earth to change by $\Delta U / c^2 = 3 \times 10^{-10}$ during a three month cycle (Charlton et al 1994).

1.5 Motivation for the present work

The previous sections have attempted to provide a general background to some methods and considerations of positron beam physics and antihydrogen production. This was necessary in order to put the present work into context since it comprises an experimental study of the formation of positronium in conditions similar to those of the antiproton trap where a positronium converter will be located in an attempt to carry out reaction 1.18. The study of

materials which are probably not suitable for such a reaction (metal oxides) was also undertaken to complement the studies of the metal targets. Also a preliminary attempt was made to measure the kinetic energy of positronium emitted from a metal surface since this is of extreme importance in the antihydrogen production rate (using 1.18). These rates are known from the Monte Carlo simulation which was carried out in order to provide a basis for the comparison of different reaction schemes under consideration by the ATHENA collaboration.

Chapter 2: Experimental arrangement and methods

This chapter contains a description of the experimental arrangement used to measure positronium formation fractions on various targets at room and cryogenic (~30 K) temperatures as well as an attempt to observe the Doppler shift of the annihilation radiation of positronium emitted from a copper target. Much of the equipment used is typical of positron beam experiments and the simplicity of this system serves to illustrate some of the basic techniques employed in experimental positron physics.

2.1 Source/Moderator

The source of positrons used in this work was a commercially available radioisotope, ^{22}Na. On installation (2/11/94) the source activity was 185Mbq and, with a half life of ~2.6 years was thus approximately half of this when these investigations began. The decay scheme of ^{22}Na is shown in figure (2.1). The endpoint energy for the β^+ particles is 0.545 MeV.

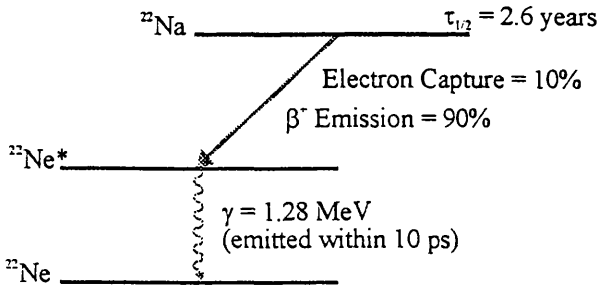

Figure 2.1 The decay scheme for ^{22}Na

As described in chapter 1, these fast particles are moderated to produce a nearly monoenergetic (with a spread of ~3 eV) energy tuneable beam. The source consists of a spot of ^{22}Na deposited on a platinum disc and sealed with a thin titanium window and preferentially emits positrons in one hemisphere. This was mounted such that the emitted β–particles struck four annealed tungsten meshes. These meshes were not aligned, so that the transmission was reduced and particles that enter them underwent the energy loss mechanisms, described in section 1.3, and were thus moderated. The meshes were annealed in an oven which consisted of two separated pieces of 99.95% pure tungsten foil (0.025mm thick). These strips formed part of a circuit and, with the meshes in between, could be heated by passing a current through them. This heating was performed

in a vacuum (of ~10^{-2} mbar). Initially the oven was heated to over 100°C to remove water adsorbed on the surface of the foils or the meshes. Then the temperature was gradually raised to ~2000°C. During this stage the pressure in the chamber rose and so the heating had to be sufficiently slow to allow the pumping rate to be greater than the rate at which material was desorbed from the oven assembly. Thus, the pressure was kept below 10^{-1} mbar throughout the heating process.

After heating, the meshes were allowed to cool to room temperature. They were then transferred through air and installed in the source/moderator unit. This comprised two sets of stainless steel rings. The first contained a push fit holder into which the meshes were held in place, and the second served to hold an earthed grid. A schematic of this arrangement is shown in figure 2.2.

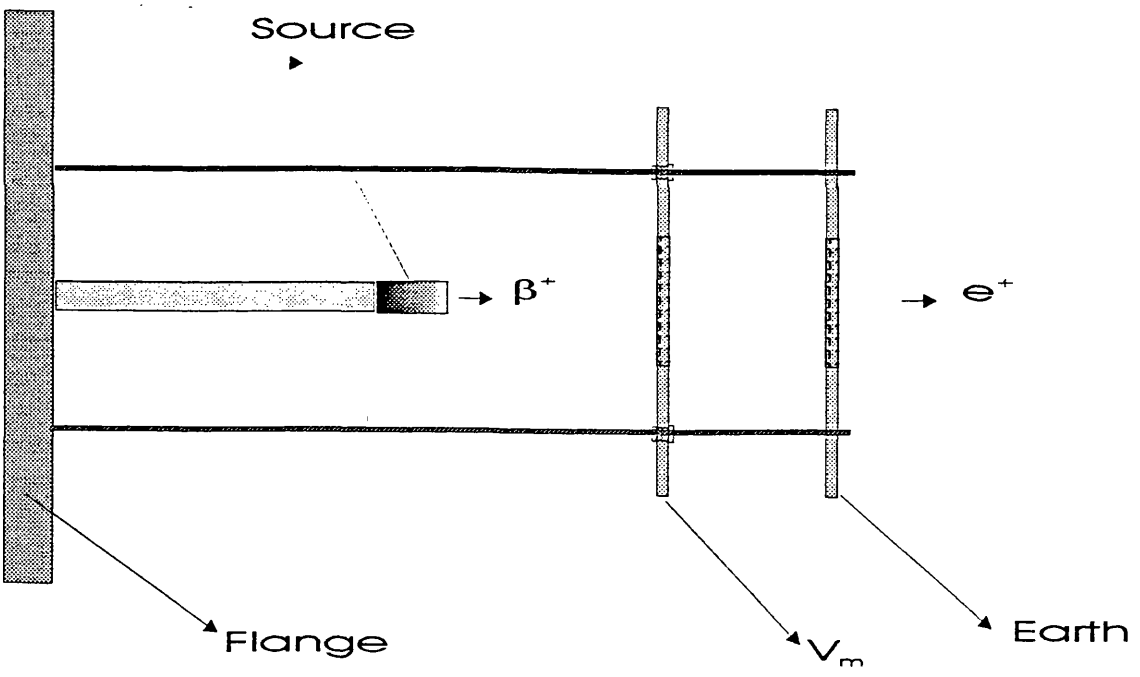

Figure 2.2. A schematic of the source/moderator arrangement. The presence of the earthed grid produces a near uniform electric field between it and the moderator which accelerates the slow positrons to the desired energy, determined by V_m.

The fact that tungsten does not necessarily need to be annealed in situ (although this would be preferable), as well as its relatively high efficiency, makes it the moderator of choice for many experimenters, despite the fact that more efficient types exist (see table 1.1).

The source and the moderator are electrically connected (external to the vacuum chamber) so that the maximum energy (in eV) of the slow positrons which have passed through the earth grid is given by

$$E_{e^+} = V_m + |\phi_+| \qquad (2.1),$$

where V_m is the voltage applied to the source/moderator and, ϕ_+ is the tungsten positron work function, which is -2.6 eV. The fact that this is a negative quantity means that thermal positrons are ejected with an energy ranging from 0 to 2.6 eV, as described in section 1.3.2c, and so the beam is expected to have an energy spread of at least 2.6 eV.

2.2 Vacuum system

The system used for the measurements was an ultra high vacuum (UHV) system. The usual base pressure, as measured by an ionisation gauge in the interaction region (see below) was ~10^{-7}-10^{-8} mbar, falling to ~10^{-9} mbar when the cryostat was in operation. These pressures may have been further reduced by baking the system (that is, heating the entire chamber) to a ~ over 100 °C, but the chamber pressures obtained without doing so were sufficient for this work. The schematic of the system is shown in figure 2.3. The two oil based diffusion pumps (one 6 inch and one 2 inch diameter, both containing Santovac-5 oil) were backed by Varian SD-300 rotary pumps. Both backing lines were fitted with a Pirani gauge to measure the backing pressure. Also, magnetic valves and manual isolating taps were installed between the backing and diffusion pumps. The system may be thought of as consisting of two distinct regions, the source region (SR) and the interaction region (IR). These could be isolated from each other by closing the UHV gate valve. This enabled modifications to be carried out in the interaction region while the source end remained at low pressure, thus protecting the moderator from contamination. Each region had its own independent pumping arrangement for this reason.

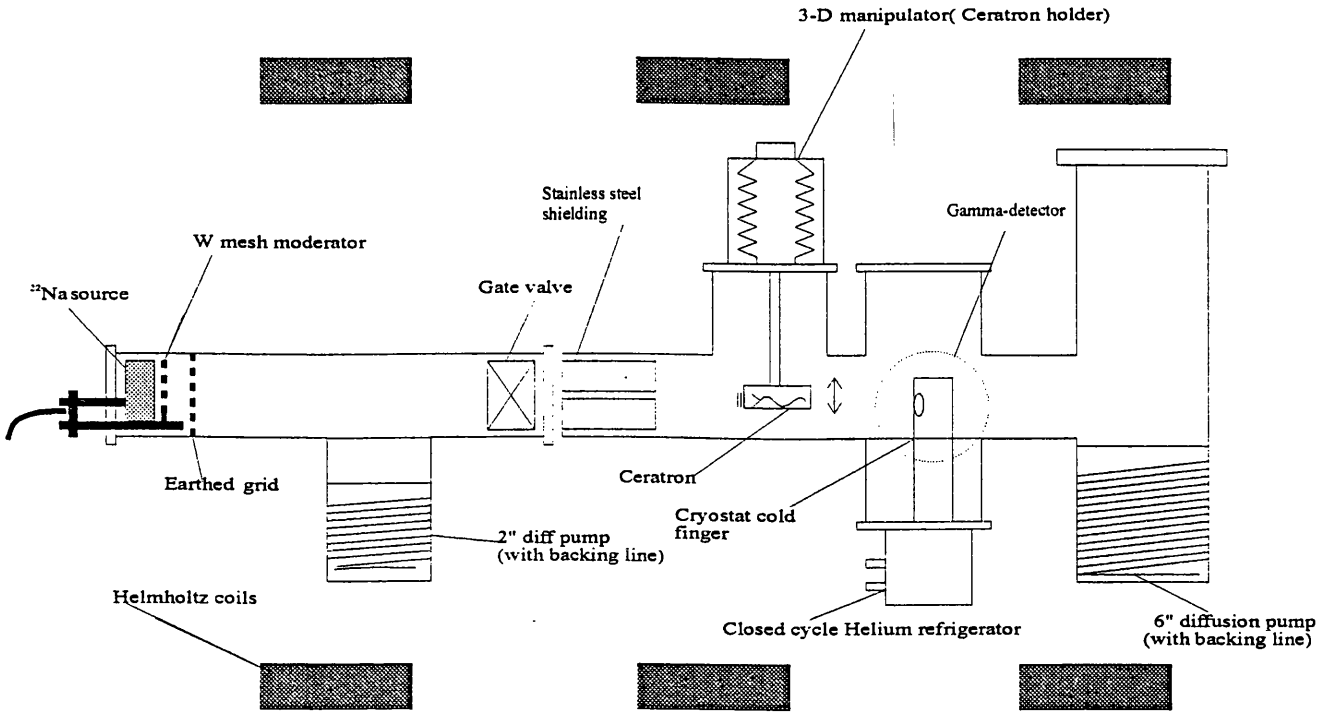

Figure 2.3 A schematic of the beamline.

The walls of the chamber itself were stainless steel and the various components were flanged together using oxygen-free copper gaskets. (The diffusion pumps were attached using indium wire seals). Inside the chamber, stainless steel was used where possible. However, for convenience, the ceratron (charged particle detector) was mounted on an aluminium block and the cryostat radiation shield was made from copper, but these did not significantly affect the vacuum conditions.

A number of measures were taken to protect the system in the event of an interruption to the power or water supplies. To prevent the diffusion pumps (which were water cooled) from overheating in the absence of water flow, trip meters were installed which relied on the pressure of flowing water to maintain a closed circuit. Thus, if a leak, blockage or other interruption to the supply occurs the circuit will be broken. This caused the diffusion pumps to shut down, the magnetic valves to close and all internal high voltage devices (that is, the moderator and/or the ceratron) to be switched off. The same happened if the power was cut

off or if the backing pressure (as measured by the Pirani gauges) increased above 0.1 torr, which might have indicated a leak, an uncontrolled influx of gas or a pump failure.

2.3 Beam transport

The positron beam was magnetically guided along the length of the experiment and the confining magnetic field, produced by six Helmholtz coils of radius 600 mm, produced field strengths in the range ~ 0-100 Gauss. The current supply to each coil, as well as its position, was adjusted manually to optimise beam transport. In addition to this, four sets of rectangular steering coils were positioned such that both sections (SR & IR) of the apparatus were enclosed above, below and at the sides by a cube-like structure of coils. These were ostensibly installed to counter the effect of the Earth's magnetic field on the positron trajectories. The geometry of the system prevented the use of a true Helmholtz arrangement (in which all of the coils are separated by their radius along the length of the experiment), although a close approximation was possible.

The motion of a particle with charge q in a magnetic field depends on the relative orientation of the velocity, v, of the particle and the field lines. When these are parallel, no force acts, and so the particle moves in a straight line. If they are perpendicular a force (F) given by,

$$F = Bqv \qquad (2.2)$$

acts in a direction perpendicular to both B and v and therefore results in a circular motion. Since a mesh moderator was used, the emission of slow positrons occurred over a wide range of angles (the angle that these particles make with the field lines is known as the pitch angle θ_p). The positrons then underwent a superposition of circular and linear motion. That is, they followed a helical path, spiralling along the axis of the field. The velocity components of the particle were then $v\cos\theta_p$ along the field lines and $v\sin\theta_p$ in the plane perpendicular to the field. It is the latter that gave rise to the circular motion. The radius of such motion is, from 2.2 and Newton's second law,

$$r = \frac{m(v\sin\theta_p)^2}{F} = \frac{mv\sin\theta_p}{qB} \qquad (2.3).$$

If the variation of the magnitude of the guiding magnetic field varies slowly compared to the time taken to complete an orbital rotation, then the radius of orbit and the energy of the

particle will vary adiabatically. Then, if the field strength changes from, say, B_1 to B_2 the pitch angle varies as

$$\frac{B_1}{B_2} = \frac{\sin^2 \theta_{p1}}{\sin^2 \theta_{p2}} \qquad (2.4)$$

So, in the interaction region this angle decreases due to the steering arrangement in use, which involved an increased field strength at the target area. These pitch angles are expected to be small since, generally, $V_m >> \phi_+$ so even if work function emission of a particle were to occur perpendicular to the magnetic field (this is unlikely, see equation 1.13) the maximum pitch angle would be

$$\theta_p \approx \arctan\left(\frac{\phi_+}{V_m}\right)^{1/2} \qquad (2.5)$$

which is of the order of ~3° or so for typical energies used in this work.

2.4 Cryostat and target

The various targets used in this investigation were all attached to the cryostat cold finger on the bench and then installed in the vacuum chamber. The targets were, MgO, silica aerogel, annealed tungsten foil and untreated copper. With the exception of the former, these were all simply attached to a copper mount on the cryostat head (in the case of the latter, the mount was itself the target). The MgO was applied by burning magnesium strips and allowing the resulting smoke (MgO powder) to form a layer approximately 1 mm thick on the copper support.

The cryostat comprised an APD closed cycle helium compressor (model HC-2) with an APD expander (model DE-202). The compressor unit was an hermetically sealed rotary vane positive displacement device. The lubricant was a synthetic oil which, since the unit is sealed, was never changed. Some oil contamination of the gas supply can occur and so the unit was fitted with an adsorber, which cleans the gas and may be replaced when necessary. The expander (see figure 2.4) uses the gas output from this compressor to achieve refrigeration by the following principle.

Initially, high pressure helium is admitted through the rotating disc valve through the slack cap and into the regenerators. These regenerators, having been cooled by the preceding exhaust stroke, cool the incoming gas. The entire unit containing the regenerators and the slack cap moves coherently and is called the displacer. This is lifted up as gas flows through the slack cap passage which creates expansion space at the heat stations for gas that has already passed through the regenerators. The gas cools in the heat stations as it is expanded and is then pushed out through the regenerators in the exhaust stroke. Each successive cycle cools the heat stations and the temperature is progressively reduced. The cooling time is approximately 1 hour (to ~30K).

The temperature of the second heat station (which is where the target mount is attached) was checked with a platinum resistance thermometer using a standard four point probe and found to be ~30K. The radiation shield was attached to the first stage heat station and fully enclosed the second heat station, other than a 10mm radius hole which was drilled in the shield through which the positron beam entered (see figure 2.3). A high transmission (95%) copper grid across this hole maintained a near uniform electric field between the target and shield when a bias was applied to the target.

When gas was condensed on the target it was directed onto the cold surface, rather than allowing the entire chamber to be flooded. This was achieved by the use of a PTFE tube, attached from the gas inlet to a small hole in the radiation shield just in front of the target. The gas line was fitted with a reducing valve to ensure a constant gas flow and the inlet was via a needle valve so that gas could be injected at very low pressures (10^{-9} mbar and upwards).

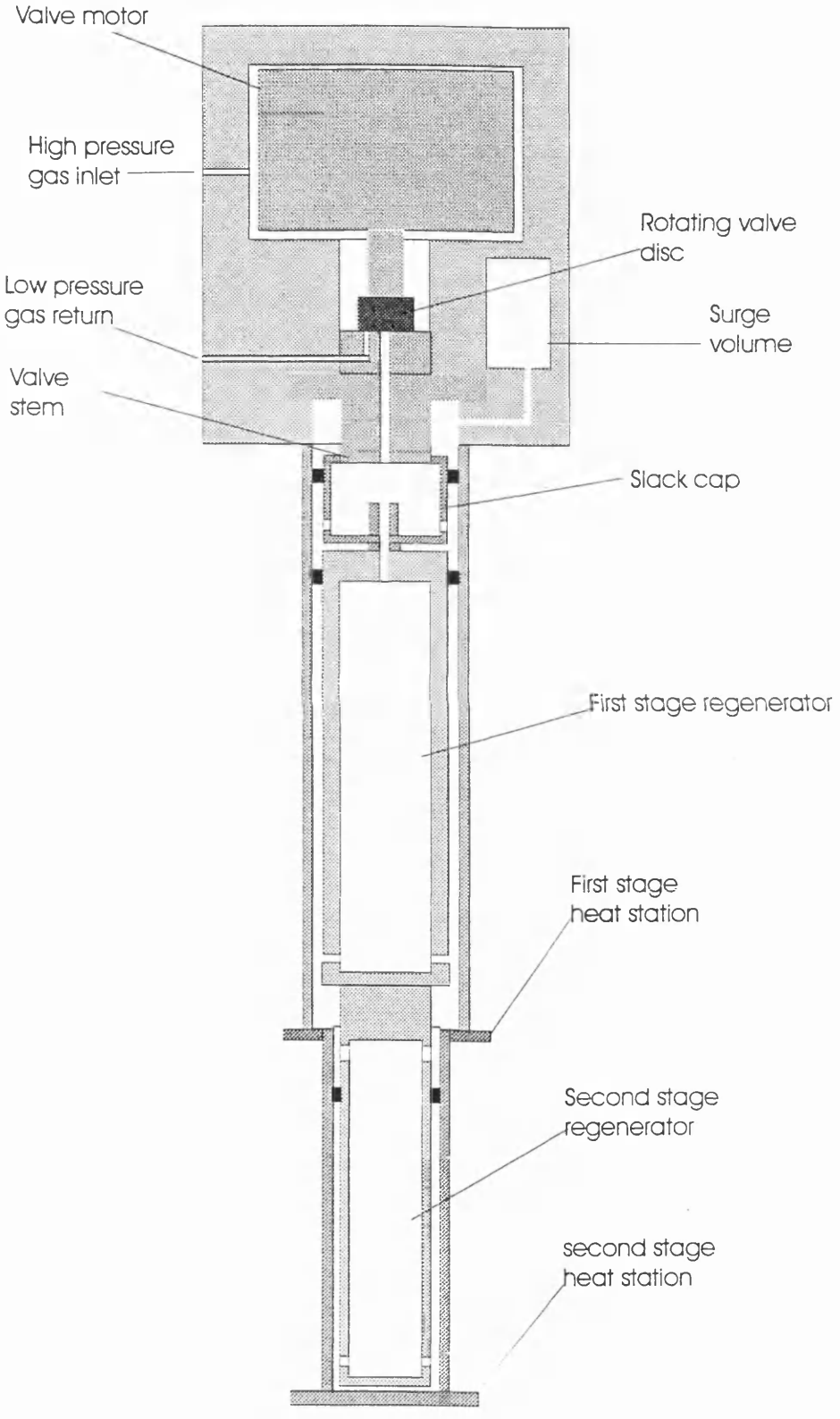

Figure 2.4 The helium expander (DE-202). The internal white regions represent the areas where gas flow occurs. During successive pumping cycles helium is expanded and ejected from the expander which progressively cools down to ~30 K.

2.5 Detectors and electronics

The measurement of positronium fractions was accomplished by spectroscopy of the positron/positronium annihilation radiation. The spectra were measured with an eV products CsI photodiode (model no. eV-250). This device consisted of a cylindrical CsI crystal scintillator, 40mm in diameter and 40mm long, coupled to a photodiode, and contained a built in pre-amplifier. The small size of this detector made it easy to install and it was possible to place the crystal face close to the target area. A photodiode (rather than a photomultiplier) based detector was chosen since close proximity to the target meant that the detector was in the magnetic field produced by the Helmholtz coils. The operating bias was +70V and this was supplied by batteries connected across a voltage divider. Large resistors were used to avoid drainage and this unit supplied sufficient power for more than one year before new batteries were required, making the unit very cost effective. The pre-amplifier operating voltage of +/- 12V DC was also supplied via batteries which also provided sufficient power for over a year.

The output from the CsI photodiode was connected to an ORTEC 572 spectroscopy amplifier. These amplifiers feature very low noise and a large gain range and are therefore suitable for many applications. The output from the 572 was connected to a multi channel analyser (MCA). This is a PC based device that records the number of signal pulses occurring at different pulse heights.

The positronium annihilation radiation Doppler shift measurements were made using a similar arrangement to that described above. The detector used was an ORTEC high purity Germanium (HPGe) detector, model number GEM-20200, which had a resolution of 0.2%, as measured (see section 3.5). The crystal position was approximately the same as that of the CsI, despite the difference in size (the Ge crystal was 50 mm diameter and 56 mm long).

The output of the preamplifier associated with the HPGe detector was also connected to a 572 amplifier. The output from this was then connected to an ORTEC 408a biased amplifier. This device consists of a discriminator and amplifier so that a portion of an amplified signal can be selected, via the discriminator and then boosted, allowing close inspection of one part

of a spectrum; in this case the 511 keV photopeak. The 408a output was connected to a MCA.

The beam transport was optimised and monitored by the use of a ceratron. This is a single channel electron multiplier made from high resistivity ceramic (hence the name) glass with a large secondary electron coefficient. That is, several secondary electrons are liberated for each incident particle. Incident particles (in this case, positrons) enter the ceratron cone and release a (secondary) electron by collision. The back of the detector is maintained at a high positive voltage (typically ~3 kV) and so the secondary electron is accelerated towards this point. Because the channel is curved (a number of forms exist) there is no clear path towards the back and the accelerated electron repeatedly strikes the wall, releasing more electrons, which themselves release yet more, and so on. This results in a cascade effect such that an incident particle gives rise to a pulse which reaches the back of the detector and is collected as the output signal (see figure 2.5)

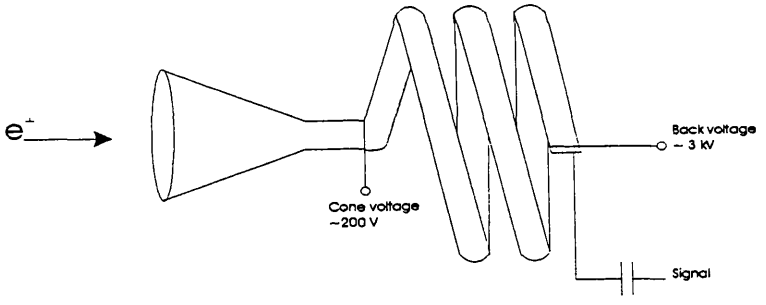

Figure 2.5 A single channel electron multiplier. The coiled channel means that secondary electron emission occurs in a cascade, delivering a pulsed signal to the back of the detector.

The cone is usually kept at a small (~200 V) potential, which is negative for positron detection and positive if electrons are to be detected. However, if one is making a comparison between electrons and positrons an adjustment to the potential on the back should be made so that the overall potential difference between the cone and back, and hence the gain of the device, is kept constant. The output pulse from the back of the ceratron was amplified by an ORTEC 9301 fast preamplifier which simply boosted the relatively small signal. However, this also boosted any noise and so the preamplifier output was connected directly to an ORTEC 583 constant fraction differential discriminator. This device generated a timing pulse and also acted as a single channel analyser. The possible discriminator levels ranged from -30 mV to -5V, so that the input signal had to exceed the lower level setting but

not that of the upper in order to generate the output signal. This was necessary because the fast current pulses from the ceratron output had a range of voltage amplitudes from a few tens of mV up to a few hundred mV, and random noise pulses exhibited similar characteristics at the lower end of this range. With the discriminator, these were filtered out. The pulses so generated were then counted by an ORTEC 994 dual counter/timer. In this application this unit simply counted the number of input pulses (per second, as set) which corresponded to a particle flux, which was dependent on the detection efficiency of the ceratron and was always, therefore, less than the actual flux. In this way the positron beam was monitored and beam transport, via manipulation of the coil positions and currents, was optimised.

2.6 Positronium fraction measurement: Technique and calibrations.

The positronium fraction is defined here as the fraction of incident positrons entering a material which subsequently go on to form positronium, either in the bulk or at the surface of the material, which is then emitted into vacuum. However, for some of the materials used in this work this definition should be applied with caution. For example, MgO powder is comprised of a granular structure with large intergranular spaces (See section 3.2). Positronium can be formed in these grains and then diffuse into the spaces, although it may still be considered to be in the "bulk". Similar considerations apply to the silica aerogel. Specific details of the formation of positronium with the various materials used are discussed more fully elsewhere (see sections 1.3.1d, 1.3.2d and 3.2). Positronium fractions, as defined, may be determined by spectroscopy of the annihilation radiation. The three-gamma decay of ortho-positronium (see figure 1.2) means that the rest mass energy of the annihilating positronium atom (1022 keV) is divided into three, such that the photons contribute to the entire gamma-ray spectrum, up to 511 keV, whilst the photons associated with two-gamma annihilation contribute only to the peak at 511 keV, known as the photopeak. Thus, the ratio of the number of events in the entire spectrum to that of the photopeak can be directly related to the amount of ortho-positronium present. Since ortho-positronium is created in a fixed ratio to para-positronium (3:1, see section 1.2), knowledge of the amount of o-Ps present allows one to determine the total positronium fraction (see

below). As an illustration, the difference in the annihilation gamma-ray spectra for the extreme cases of 0% and 100% positronium formation are shown in figure 2.6.

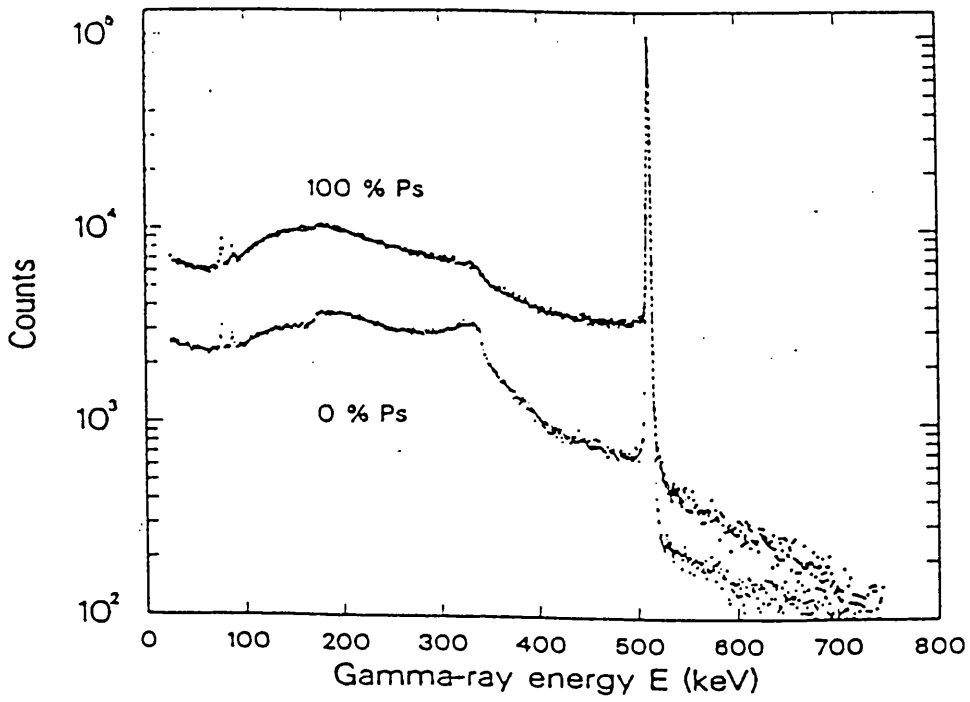

Figure 2.6 Annihilation spectra for positronium fractions of 0% and 100 %, as measured by a high resolution Ge detector, normalised to peak heights. It is clear that there is a greater proportion of counts in the region between the peak and the Compton edge in the case for 100% positronium formation than for the case where there is no positronium. (see text) Lahtinen et al (1986)

The following description of the quantitative measurement of positronium fractions follows the work of Marder et al(1956) as well as that of later researchers, such as Coleman et al (1993), Schultz et al (1986) and Mills (1978). It should be pointed out that this technique is appropriate only to the formation of positronium in vacuum (which may be interpreted as, for example, the intergranular spaces in a metal oxide, see section 3.2) since o-Ps residing in the bulk of a solid is likely to annihilate via pick-off into two photons instead of three. (Pick-off is the process by which the ortho-positronium wavefunction overlaps with the (spin averaged) wavefunction of a local electron, resulting in fast two photon annihilation. The rate at which this occurs is clearly dependent on the local electron density). The following treatment is based on the relative number of counts in certain regions of the

spectrum (the particular form of which is itself based on the number of photons given off during annihilations), and so, if the pick off rate is small, corrections can be made for the process. If the rate is large this type of analysis will not be valid. A parameter, R, is defined as

$$R = \frac{(T-P)}{P} \qquad (2.6),$$

where T refers to the number of counts in the total spectrum and P to the number in the photopeak (approximately). The actual definition of these regions is largely arbitrary but must remain constant for a given set of measurements and associated calibrations (see below). The limits chosen for the photopeak (42 keV centred on peak) were wide enough to minimise sensitivity to small drifts in spectra position. The limits for the total spectrum went from the peak upper limit to an arbitrary point near the lower end, (from 250-530 keV) which was chosen to be well above an area of low level noise at the lowest end of the spectrum. The exact source of this (electronic) noise was not clear but could vary during measurements and would, if included in the measured regions, give rise to erroneous data.

Let f be the positronium fraction and subscripts 0 and 1 refer to 0 and 100% positronium formation respectively. Then we may say that the total counts in the spectrum for a given Ps fraction contain contributions from positronium formation (fT_1) as well as direct annihilation and background radiation, $(1-f)T_0$. Thus, we may say that,

$$T_f = fT_1 + (1-f)T_0 \qquad (2.7a)$$

and similarly

$$T_f = fT_1 + (1-f)T_0 \qquad (2.7b).$$

and similarly,

$$P_f = fP_1 + (1-f)P_0 \qquad (2.8).$$

If 2.7a is re-written in terms of 2.6 we find,

$$P_f(1+R_f) = f(R_1P_1 + P_1) + (1-f)(R_0P_0 + P_0)$$

If we replace P_f in 2.8 with the expression 2.7.b we find,

ind,

$$+ R_0P_0 + P_0 \qquad (2.9a)$$

which reduces to,

$$(R_f - R_0)P_0 = f(R_f P_0 - R_0 P_0 + R_1 P_1 - R_f P_1) \qquad (2.9b),$$

or

$$\frac{1}{f} = 1 + \frac{(R_1 - R_f)P_1}{(R_f - R_0)P_0} \qquad (2.9.c).$$

This equation is widely used for measurements of positronium fractions. Clearly, to extract f from 2.9c one must measure R_f (that is, measure T and P for some unknown f which is to be determined). It is also necessary, however, to perform some calibration measurements to determine R_0 and R_1 (and, by implication, P_0 and P_1). Background radiation was determined simply by measuring T and P with a small negative voltage on the moderator so that fast "unmoderated" positrons (which were considered to be part of the background radiation) were largely unaffected, but the slow positron beam was cut off. The measured T and P values were then simply subtracted from measurements made when the slow positron beam accelerated to the target region.

To determine R_0 a 3 keV beam was implanted into untreated (neither surface nor bulk) copper. No positronium was expected to form in this scenario since very little (less than 10%) backscattering is likely to occur (Knights and Coleman 1995a) and the implantation depth is much larger than the diffusion length. In section 3.4 we find a *thermalisation* length for the copper samples used in this calibration of ~ 10 Å , while at 3 keV a mean implantation depth of ~ 300 Å is expected, and so no positrons were therefore expected to reach the surface, and the R_0 measurements were thought to be reasonably accurate.

To achieve 100% positronium formation, and thus measure R_1, a flange mounted halogen lamp/ silver foil target assembly (shown in figure 2.7) was constructed. Silver is known to form positronium, following positron impact, very efficiently when heated (e.g. Lynn 1979, Poulsen et al 1993). A silver foil sample (20 x 20 0.25 mm, 99.95% pure) was therefore heated by the halogen lamp and the ratio P/T was measured. A low energy (50 eV) beam was implanted into the heated silver foil which had a small negative potential (15 V) applied to it, so that any reemitted positrons were drawn back to the surface where they must, eventually, either form positronium or annihilate. The current in the halogen lamp

was gradually increased until no further increase in the positronium fraction (as measured by the ratio of P/T) was observed, at which point 100% positronium formation was assumed and the T_1 and P_1 data were recorded. In fact, data were continuously collected and associated with the lamp current (as a measure of the foil temperature) in order to observe the thermal desorption effect and the positronium fraction for both clean and contaminated surfaces was compared, as shown in figure 2.8, with positronium fractions calculated according to equation 2.9c. The positronium fraction may be seen to be levelling off at a current of ~10 A , but this is not a definitive saturation. It proved to be impossible to heat the samples further without destroying them and so this possible source of error had to be accepted. However, the positronium fractions measured are consistent with other work (see chapter 3).

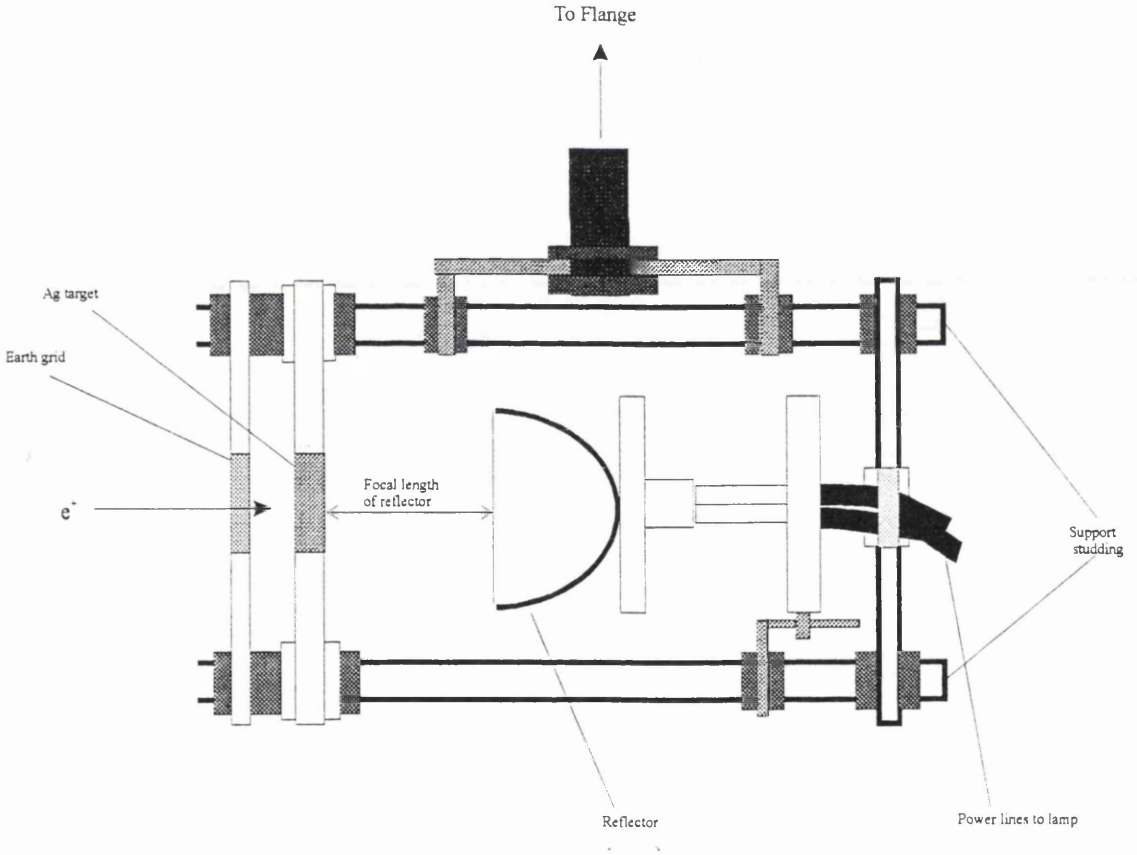

Figure 2.7. The halogen lamp and silver foil assembly. The Ag target is heated from behind by a 150W halogen lamp which is positioned so that the focal point of the reflecting lamp is the centre of the target.

The hysterisis type curve of figure 2.8 (with correspondingly lower fractions seen when the current was increasing compared to those as it decreased) was thought to be due to surface contamination effects. When the silver was heated the surface was gradually cleaned so that

when the current was reduced the contamination levels for a given current were also reduced. Since positronium can only be formed at the surface of silver, as with all metals, the formation of positronium is correlated to the state of the surface.

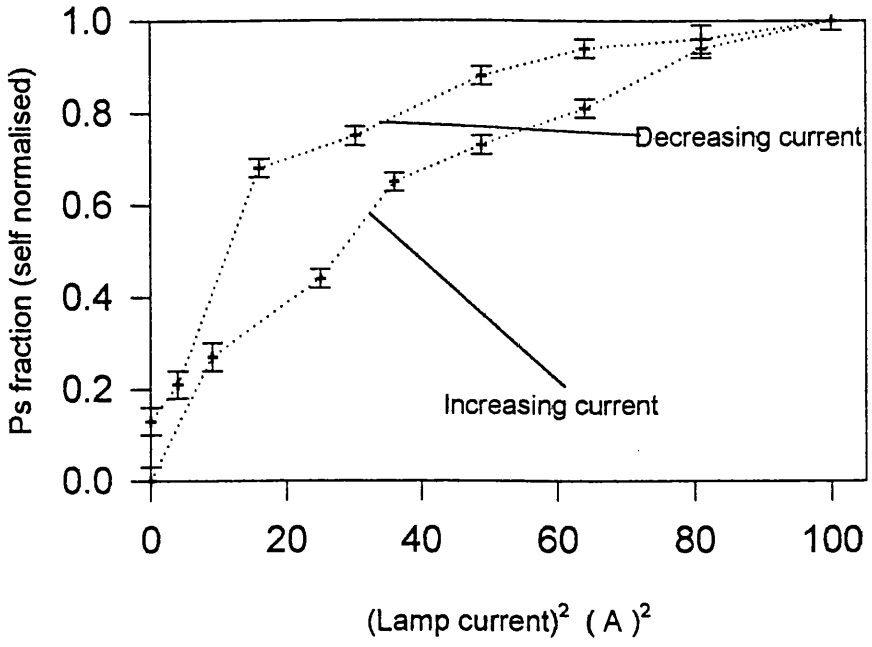

Figure 2.8. The variation of the positronium fraction for 50 eV positrons incident on heated silver foil with lamp current (shown as current squared). The hysterisis effect is thought to be due to surface cleaning.

2.7 Doppler shift measurements: background subtraction and peak analysis.

If energetic positronium is formed, in the manner described in section 1.3.2d, the wavelength of radiation from the annihilation of such positronium will be, in the non-relativistic case which is appropriate here, Doppler shifted by an amount

$$\Delta\lambda = \left(\frac{v_{Ps}}{c}\right)\lambda_0 \qquad (2.10)$$

in the direction of v_{Ps}, the positronium velocity, where λ_0 is the unshifted wavelength (2.43 x 10^{-12} m, corresponding to an energy of 511 keV per photon for p-Ps annihilation). These studies are necessarily restricted to p-Ps, since o-Ps annihilation does not give rise to photons of a fixed wavelength, such that shifts of their wavelengths cannot be measured.

As well as p-Ps annihilation there will of course be direct two photon annihilation. These photons will be Doppler shifted due to the momentum of the annihilating electron-positron pair and will give rise to a broadened 511 keV photopeak. Since the measurement of the Doppler shift of positronium annihilation radiation requires that it be moving predominantly in one direction, it is envisaged that these studies will be restricted to positronium formed from (metal) surfaces.

In order to measure the Doppler shifts associated with the decay of energetic p-Ps it is first necessary to subtract the background underlying the photopeak. The form of gamma ray peaks measured with Ge detectors (see section 2.5) is generally asymmetric, with a non-linear background due to gamma-ray scattering, incomplete charge collection and electron escape from the detector. Figure (2.10) shows an example of such a non-linear background (the general form of which is common to all gamma ray peaks) from a ^{137}Cs source (peak centre at 662 keV). The filled circles represent the peak, as measured, and the asymmetry between the low (A-B) and high (C-D) energy regions is clear. The analytical form of such peaks has been the subject of study of many authors and several forms of peak function, containing different step functions to describe the asymmetry, have been proposed (e.g. Robinson (1970), Kern (1970) Sasamoto et al (1975)). These are generally complicated functions with two or more variable parameters, the exact nature of which may ultimately have little effect on the final peak function. The peak functions $F(i)$ employed by the above authors are of the form

$$F(i) = G(i) + b(i) + S(i) \qquad (2.11).$$

where i is the channel number, b is the background, S the step and G is the Gaussian peak function. The reason for this arrangement is that a single peak can usually be approximated by a Gaussian, or normal, distribution, due to the statistical nature of system noise and the charge collection process in the detector. The form of this distribution is

$$G(i) = A\exp\left[\frac{-(i-i_0)^2}{2\sigma^2}\right] \qquad (2.12),$$

where $\sqrt{2}\sigma$ is the root mean square deviation of i from the Gaussian centroid channel (i_0) which is taken to be the FWHM of the measured peaks. In this case we expect the near Gaussian function representing the peak to have two components, arising from both the

direct and the (Doppler shifted) p-Ps annihilation. The photons from o-Ps annihilation are expected to make only a small contribution to the photopeak (see section 3.5) and are therefore ignored in this analysis. The background function $b(i)$ may be considered to be a linear function, determined by the background level in the high energy region (C-D). Although each region contains different levels of contribution from some of the various sources of background, any anomalies that arise by treating $b(i)$ as linear may be corrected for in the step function $S(i)$. The step effect is generated by the peak itself and so the step function should include the parameters characterising the peak. Following the work of Jorch and Campbell (1976) and that of Chaglar et al (1981), the step function chosen for this work is

$$S(i) = \frac{H}{2}\left[1 - erf\left(\frac{i - i_0}{\sqrt{2}\sigma}\right)\right] \qquad (2.13),$$

where H is the difference in height between the regions A-B and C-D. That is, the height of the step. This is determined by taking the mean number of counts in the regions A-B and C-D (sufficiently distant from the actual peak areas) and subtracting the former from the later. The reasoning behind this choice of function is that, since the peak "generates" component S(i) (i.e. the level is proportional to i), it should be both associated with the Gaussian function and proportional to the fraction of the peak in the interval $i - \infty$. This is exactly defined by the error function, erf. However, since the background decreases with energy the complementary error function, $erf = \{1 - erfc\}$ is used. The form of this function is shown in figure 2.9

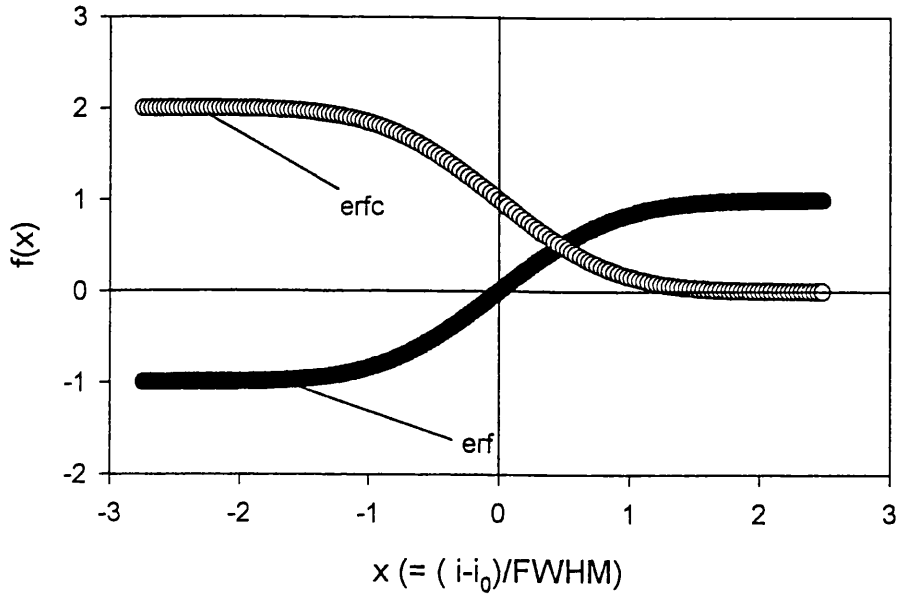

Figure 2.9 The functional forms of the standard (filled circles) and complementary (clear circles) error functions. The form of S(i) leads to a decreasing level of background subtraction at increasing photon energy.

The effect of using this function for background subtraction is shown also in figure 2.10. The filled circles show a measured ^{137}Cs peak and the disparity of the regions (A-B) & (C-D) is now quantified by H. The triangles show the same peak following a subtraction of the step function S(i), and the linear background b(i) with the relevant parameters for this peak. The mean value of the counts in the region (A'-B') is close to zero and in the region (C'-D') is zero, indicating that the peak region itself contains mostly "real" counts.

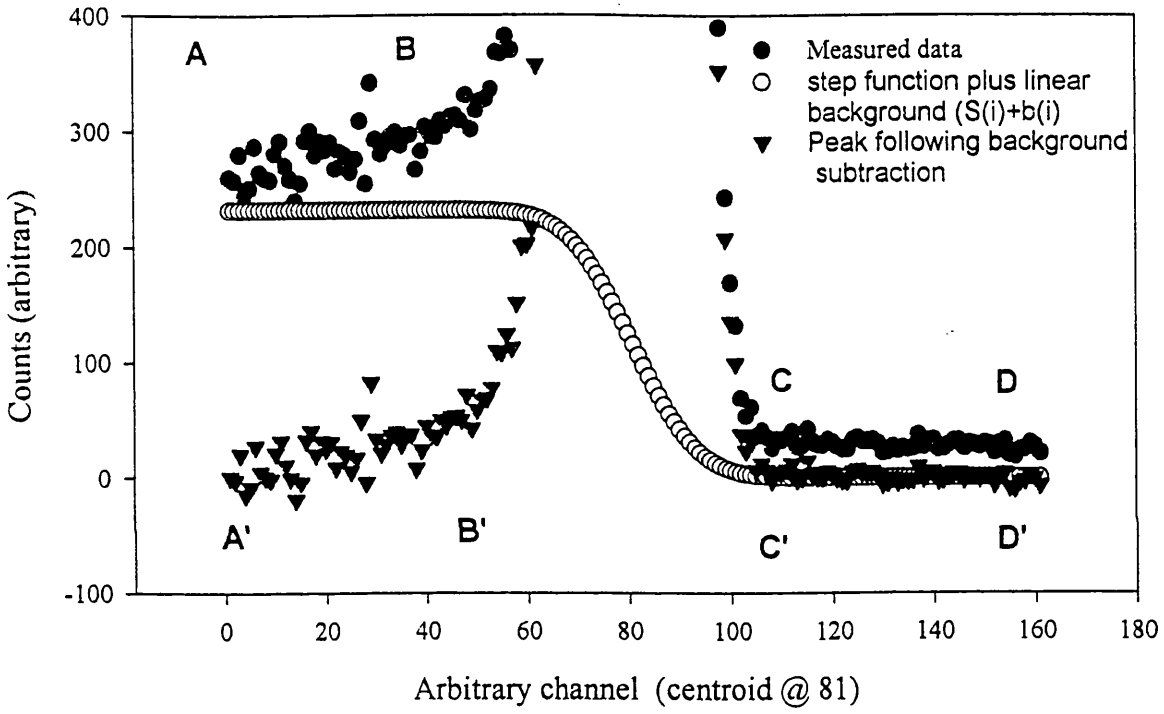

Figure 2.10 A ^{137} Cs peak before and after backgrounds subtraction. The subtraction of a background function reduces the average value of the counts either side of the peak to zero.

The experimental arrangement allows measurements to be taken with the target set at an angle to the beam so that a component of the positronium velocity will be seen by the detector, which is perpendicular to the beam, via the Doppler shift of the annihilation radiation. Thus, data can be collected for the case where no positronium is formed (using a high energy beam) or where no Doppler shift can be seen (when the target is perpendicular to the detector) or with positronium that is either blue or red shifted (depending on the relative target/detector orientation). The geometry of this arrangement is illustrated in figure 2.11. In this way it was hoped that, following background subtraction, the p-Ps component could be resolved by comparing spectra from different system configurations and that the mean positronium energy may be determined by the shift of the p-Ps peak relative to the

511 keV photopeak. The difficulties associated with resolving this component are discussed in section 3.5.

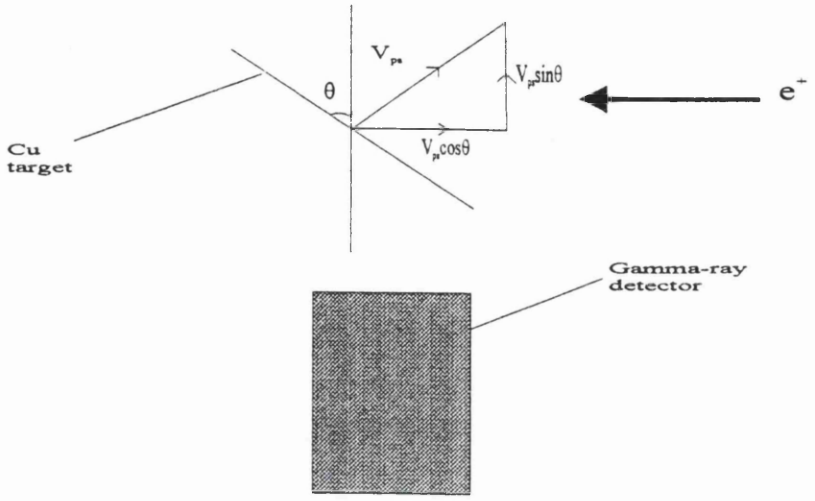

Figure 2.11. The relative orientation of the beam, target and detector. The measurement of spectra with a red shifted para-positronium component is shown. By rotating the target blue shifted components may also be measured.

Chapter 3: Results and discussion

3.1 Some points about errors

Before presenting the results of the experiments described in chapter 2, it is appropriate to consider (briefly) errors and possible sources of inaccuracy that may have arisen. All of the work considered here involved the analysis of gamma-ray spectra, which are of course comprised of photon counts which are statistical quantities. The propagation of statistical error in the addition/subtraction or multiplication/division of two such statistical measurements, $(C_i \pm E_i)$ and $(C_j \pm E_j)$, where $E_{i(j)} = \sqrt{C_{i(j)}}$, is given by the standard formulae,

$$P = C_i \pm C_j \quad , \quad E_P^2 = E_i^2 + E_j^2 \qquad (3.1),$$

and

$$Q = C_i \times \div C_j \quad , \quad \frac{E_Q^2}{Q^2} = \frac{E_i^2}{C_i^2} + \frac{E_j^2}{C_j^2} \qquad (3.2),$$

where E_P and E_Q are the propagated errors in P and Q respectively. These standard formulae were utilised in the subtraction of background peaks to provide the P and T measurements (see section 2.7) and also in the calculation of the positronium fractions using equation 2.9c to give the errors bars quoted in the next section. There were, however, other sources of error which are difficult to quantify or were expected to be negligible. Since the experiments were not performed in a temperature-controlled environment small drifts in the gain of the spectroscopic amplifier, and hence the peak position, occurred. This was compensated for by the choice of the regions T and P (see section 2.6). As a test of the sensitivity to such drifts, two regions T_o and P_o were defined three MCA channels below the "real" regions and the positronium fractions were calculated for both sets of parameters. The difference in spectra position (as judged from the position of the 511 keV peak) on a hot day and at night is typically of the order of a few channels. The difference in the calculated positronium fraction was found to be less than 1% and so this effect was not considered to be of any importance for the positronium fraction measurements. In the case of the Doppler shift measurements drifting was a more serious problem (due to the use of a biased amplifier, as well as the nature of the work) and so a ^{137}Cs source was used to

monitor peak positions while data were collected. If drifting occurred by even 1 channel, the data were discarded. This did mean that only short (~ 1500 s) runs could be taken, with correspondingly poor statistics.

Problems also arose in connection with the calibration measurements described in section 2.6. The P/T level measured as the silver foil was heated did not completely level off, which would indicate 100% positronium formation (see figure 2.8) since the target was destroyed when heated with a lamp current above 10A. Heating the silver caused positronium trapped in a surface state to thermally desorb, giving increasing positronium fractions up to 100%, and so insufficient heating may have led to a fraction less than the maximum. This calibration was thus probably in error, although comparison with other work indicated that the positronium fractions measured were reasonably accurate. Mills (1978) in similar experiments to those described here, estimated an error in his positronium fractions of $^{+5}_{-20}$%, where the asymmetry was to allow for the possibility that some positrons might not escape from the surface as positronium at high temperatures. Such estimations were very difficult to quantify and in this work have not been included in the data analysis. It is, however, expected, that similar error considerations apply and that the counting errors which are included do not describe the true accuracy of the data.

3.2 The target materials and positronium formation

This section is a discussion of the processes by which positronium may be formed in both the metal and metal oxide targets. It is necessarily divided into two sections since the positronium formation processes of these materials are fundamentally different. Clarification of these concepts will expedite an explanation of the data shown in the next section.

Probably the most important aspect of positronium formation in the metal targets was that it was entirely a surface process. That is, positronium cannot exist in the bulk of a metal (or semiconductor) that is free of defects. The reason for this is that a positronium atom in a region of high free electron density (an electron gas) would polarise that region. This would

then screen the electron-positron interaction, reducing the binding energy by an amount that depends on the density of the electron gas. In fact, this binding energy approaches zero for an electron density just below that found in Cs, the most dilute alkali metal (see for example, Lowy and Jackson 1975) and so the positronium binding energy is zero for metals. So, when positronium was formed following positron bombardment of the metallic targets (see section 1.3 for a discussion of the implantation process) it could only do so when a delocalised positron interacted with an electron in the region of lower electronic density just outside the metallic surface. Positrons in this region may have diffused back to the metal surface where they would have been ejected by work function emission (see section 1.3.2c) for materials with negative work functions (i.e. the tungsten), or they may not have been completely thermalised (epithermal) and could then have overcome the potential barrier present in materials with a positive work function (i.e. the copper). Alternatively, they may have been backscattered positrons. Note that, at the lowest incident positron energies when the implantation depth is small, the distinction between these processes is purely semantic. The ability of implanted positrons to return to the surface region depended on the implantation energy and the nature of the material (i.e., the structure and the density). If trapping sites were present the positronic mobility would have been restricted and the fraction which returned to the surface reduced.

The formation of positronium in the MgO and silica aerogel targets was fundamentally different to that in the metal targets, as considered above, due to the granular structure of these materials, and the fact that they are insulators. The distinction between the bulk and the vacuum was less clear cut in the case of the metal oxide targets because there are large voids in the "bulk" of these materials. Smoked MgO powder (as well as other metal oxide powders such as SiO_2 or Al_2O_3) are comprised of spherical grains with radii of the order of 100 Å, and with a free volume between the grains of around 50 times the grain size (Brandt and Paulin 1968). This meant that the grains could reasonably have been considered to be independent of each other. The situation was a little different for the silica aerogel (made from superfine compacted SiO_2) which has grain sizes of ~ 50 Å radius and a void size of around 14 times the grain size (Chang et al 1985b). These differences had little affect on the results described here. The grains were still effectively isolated from each other and the positronium formation mechanism was basically the same for both materials (see section

1.3.1d for a discussion of the positronium formation mechanism in insulators). When positrons entered such granular materials they were stopped in the grains where they could form positronium, which would then have been able to diffuse out to the void. This meant that, unlike in the metal targets, the ability of positronium to form was not dependent on migration back to the surface region, and therefore was not diminished with implantation energy. The formation of positronium at grains located deep within the sample was just as likely as it was for those grains near the sample surface.

3.3 Positronium and reemitted fraction measurements

The results of the positronium fraction measurements, as described in section 2.6, are presented in this section. During these measurements the base pressure of the vacuum system varied from ~ 10^{-7} to ~10^{-8} mbar. Where the presence of gas is indicated, N_2 was injected into the vacuum chamber at a pressure of $1x10^{-5}$ mbar for 5 minutes. Note that all of these measurements were performed with a negative bias of 15 V on the target to ensure that any reemitted positrons were returned to the target where they must either go on to form positronium or annihilate. The reemitted fraction measurements were made by comparing the total number of counts in the T region (as previously defined) with the negative bias applied and with the bias polarity reversed, so that any reemitted positrons were ejected. In all cases incident positron energies in the range of 0-3 keV were used.

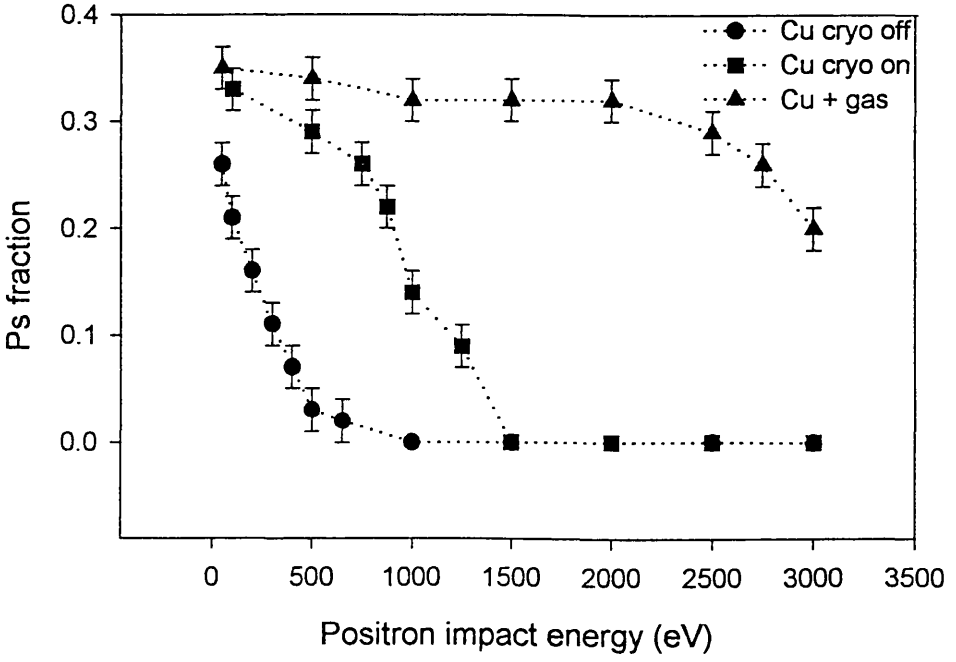

Figure 3.1 The variation of the positronium fractions with incident positron impact energy for copper.

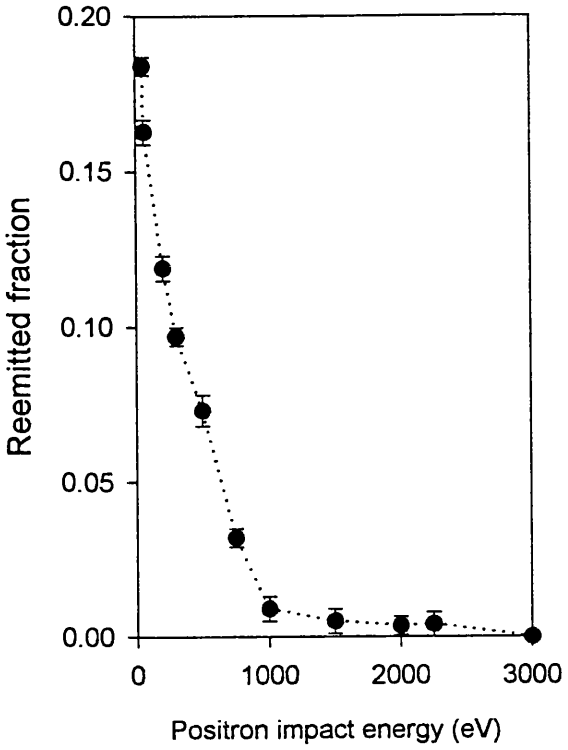

Figure 3.2 The variation of the reemitted positron fraction with incident positron impact energy for copper.

Figures 3.1 and 3.2 show the variation of the positronium and reemitted fractions with positron impact energy for the copper sample. For the moment we shall consider only the "cryo off" curve, which refers to measurements at room temperature. The form of these data is readily explained by the nature of the material involved. The sample was untreated and was therefore expected to contain many defects and impurities. Positrons implanted into this material were thus unlikely to diffuse very far before becoming trapped, either in a vacancy or in a surface state, and annihilating. So, the fraction of positrons that managed to diffuse back to the surface and were reemitted, either as free positrons (see figure 3.2) or after positronium formation, both fell off quickly with the implantation energy. Any such positrons in the copper sample were necessarily epithermal, by virtue of the positive positron work function (ϕ_+ = ~0.5 eV), and the energy dependence of the reemission of such positrons seen in figures 3.1 and 3.2 is in accord with other studies of reemission from metals with (small) positive work functions (for example see Knights and Coleman 1995b, Overton et al, 1995).

Figures 3.3 and 3.4 show the positronium and reemitted fractions for the annealed tungsten foil sample. Again, for the moment we shall consider only the cryo off measurements. These data show a much weaker energy dependence than those of the copper, which is attributed to the fact that, despite their common metallic nature, these samples were different in two very important ways. The annealed tungsten contained less trapping sites than the copper and so the diffusion length was therefore likely to have been significantly longer (see section 3.3).

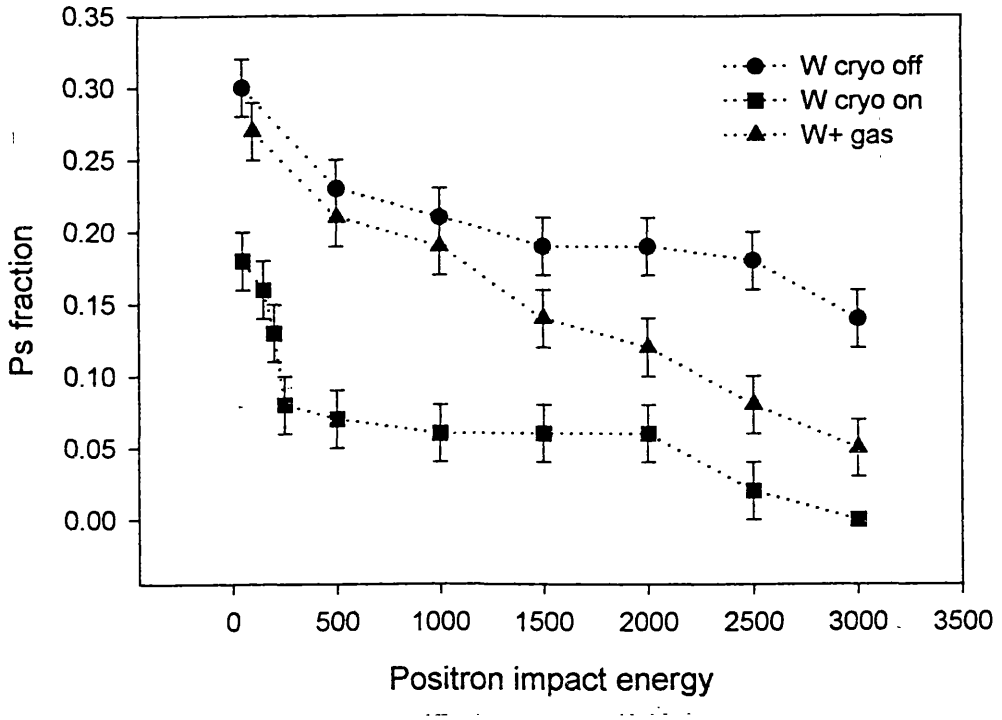

Figure 3.3 The variation of the positronium fractions with incident positron impact energy for tungsten.

Thus, positrons were able to back diffuse to the surface from greater implantation depths. Those positrons that did manage to reach the near surface region would have been ejected from the metal due to the negative work function of tungsten ($\phi_+ = -2.6$ eV). This view was supported by the variation of the reemitted fractions shown in figure 3.4 (cryo off) which showed a weak energy dependence. Unlike the data from the copper sample, the energy dependence of the tungsten reemitted fraction did not correlate closely with that of the positronium fraction. This may have been due to errors in the calibration of the latter measurements. This matter

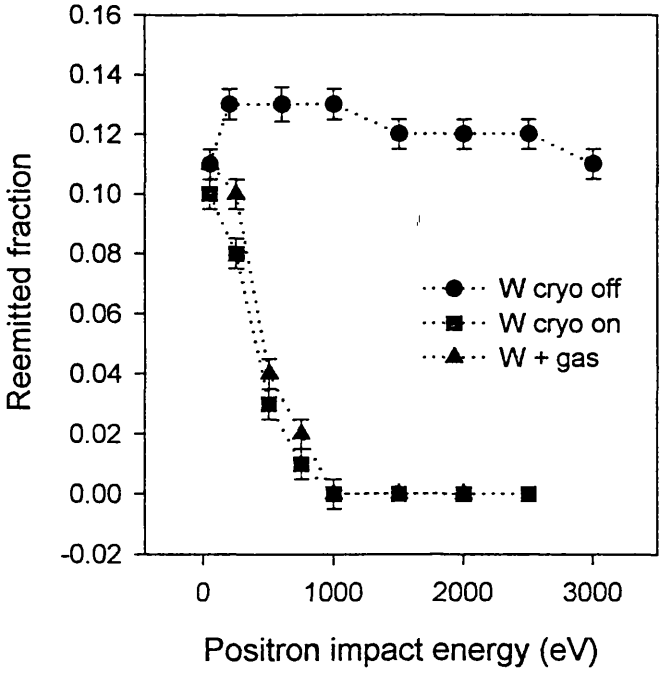

Figure 3.4 The variation of the reemitted positron fractions with incident positron impact energy for tungsten.

is considered in chapter 5. As is evident from figures 3.1 and 3.2, there is a significant fraction of epithermal positrons reemitted at energies up to ~ 1 keV from the copper target, and a similar proportion is expected to contribute to the reemission fraction from tungsten. Goodyear et al (1994) have measured the energy spectra of positrons reemitted from annealed tungsten foils over the energy range considered in this work. They found three distinct components which they associated with work function emission, epithermal emission and energy loss from surface contaminants. Work function emission was observed for all incident energies while epithermal emission (defined as the reemission of positrons with energies of 2eV above the work function) was observed with decreasing intensity up to energies of 1.5 keV. Thus, the low energy regions of figures 3.3 and 3.4 were attributed to both work function and epithermal positron emission. Since the foil was not annealed in situ it was expected to be contaminated on the surface in a similar fashion to the samples used by Goodyear et al and so the absolute positronium yield was very likely to have been reduced (by an unknown amount) compared to that which would have been observed if the sample had been cleaned in situ (Goodyear et al 1994).

The general form of the cryo off curves of figures 3.1-3.4 is thus explained in terms of the mobility of positrons within the target materials. In the copper they are easily trapped and so cannot diffuse to the surface, even at relatively low implantation energies. Those that can reach the surface must do so with enough energy to overcome the positive potential step due to the work function if they are to be reemitted. Therefore, no reemission or positronium formation occurs at or above these implantation energies (i.e. ~1 keV). Positrons in tungsten are more mobile, since there are fewer trapping sites, and can back diffuse to the surface at implantation energies well above those seen with the copper. In addition to this, the negative work function of the tungsten means that even positrons with thermal energies in the near surface region are ejected. So, the tungsten positronium fractions were higher than those of copper, while the energy dependence was weaker.

We now turn our attention to the cryo on and sample+gas data of figures 3.1, 3.3 and 3.4. When the cryostat was operational the sample temperatures were of the order of 30 K (see section 2.4) and so some of the vacuum contaminants present condensed on the samples. Any changes to positronium fractions seen with cold metal targets was attributed to the

effects of condensed layers and not to the intrinsic sample temperature. Lynn et al (1980) have shown that the positron trapping rate and positronium fraction are effectively independent of sample temperature (below room temperature) for Cu(111). The assumption is made that this is also the case for the metal samples used in this work.

There were two sets of measurements made with the cryostat on. In the first, denoted by "cryo on" in all positronium fraction figures, no additional gas was introduced and the vacuum contaminants present (mostly water) condensed on the target surfaces. These measurements were of interest primarily because they represented conditions similar to those that are expected to be present in the antiproton trap (see section 1.4.2b). The exact nature and quantity of these contaminants was not quantified (except by base pressure prior to freezing, which was always ~ 10^{-7} mbar or less, and ~10^{-8}-10^{-9} while the cryostat was on). The gas measurements were made with N_2 gas injected directly onto the cold finger (see section 2.4) via a PTFE gas line such that the pressure as measured by an ionisation gauge rose to 5 x 10^{-5} mbar for 5 minutes. This was expected to produce a very thick layer of solid N_2, although the exact size was not known. Applying considerations similar to those of Gullikson and Mills (1990) we estimate a gas layer ~ 0.04 mm thick.

The copper data of 3.1 (Cu+gas) show that the thick layer of solid N_2 was a more efficient positronium converter than the unnanealed copper. Similarly, the condensed vacuum contaminants also produced more positronium than the bare metal target. The reason why the surface "contamination" of the copper target actually increased the positronium fractions was probably that the irregular and uncleaned surface and bulk of the Cu contained a lot trapping sites. The affect of the vacuum contaminants may have been to allow positrons that did not penetrate through to the Cu surface to diffuse back out to the vacuum more easily since it is likely that there were less trapping sites in the condensed layers. Also, positronium may have been formed within these layers (largely composed of molecular solids) which subsequently diffused to the vacuum. When the positrons did penetrate to the Cu the positronium fraction fell rapidly to the bare Cu levels, as shown in figure 3.1. It seems that the gas layers applied were thick enough to prevent most of the implanted positrons from reaching the Cu, although a steady decline was observed in the positronium fraction at energies above ~ 2.5 keV. The diffusion length in solid N_2 is

estimated in section 3.3 as ~2400 Å, in reasonable agreement with the value of 1800±300 Å obtained by Gullikson and Mills (1990), although these authors assume a Gaussian stopping profile, while an exponential profile is assumed in this work. Without that assumption the data of Gullikson and Mills yields a diffusion length of ~2000 ± 300 Å.

The cold tungsten data (figure 3.3 cryo on, W+gas) is not so readily explained. While the cryostat was operating the positronium fraction was seen to fall dramatically, falling to ~5% at implantation energies above 500eV or so. It is not clear why these data are different from the Cu data with contaminants condensed on the surface. If the surface layer (which should be approximately the same for both samples) was thin enough to allow positrons to reach the tungsten then we would expect positronium fractions similar to those obtained with the tungsten at room temperature. If, on the other hand, the layer was thick enough to prevent penetration to the metal surface we should expect positronium fractions similar to those seen in figure 3.1 (cryo on measurements). In fact neither of these situations were observed. The steep fall off of these data suggests epithermal reemission from a surface layer, and the reemitted fraction data of figure 3.4 (cryo on), while showing a weaker energy dependence, are consistent with such a process. However, this is not in accord with the cryo on data for the copper target. In the gas data (W+gas) the variation for implantation energies below ~ 1 keV was virtually identical to the data for the bare tungsten. Above this energy the data began to diverge, with the gas fractions falling off faster than the bare metal data. These fractions were, however, lower and more sensitive to energy than the gas on copper fractions. This is also not yet fully understood. Chapter 5 contains some speculations on these data, as well as some suggestions for possible systematic studies that may shed some light on the problem.

It is assumed that the metal oxide samples, MgO and aerogel, used in this work was similar to those described by Brandt and Paulin (1968) and Chang et al (1985b) respectively (see above). The targets used were different in physical size. The MgO was prepared by burning strips of Mg in air and allowing the smoke to collect on a copper plate with a 20 mm square face. The final layer was ~1 mm thick. The silica aerogel target was a cube around 20 mm square.

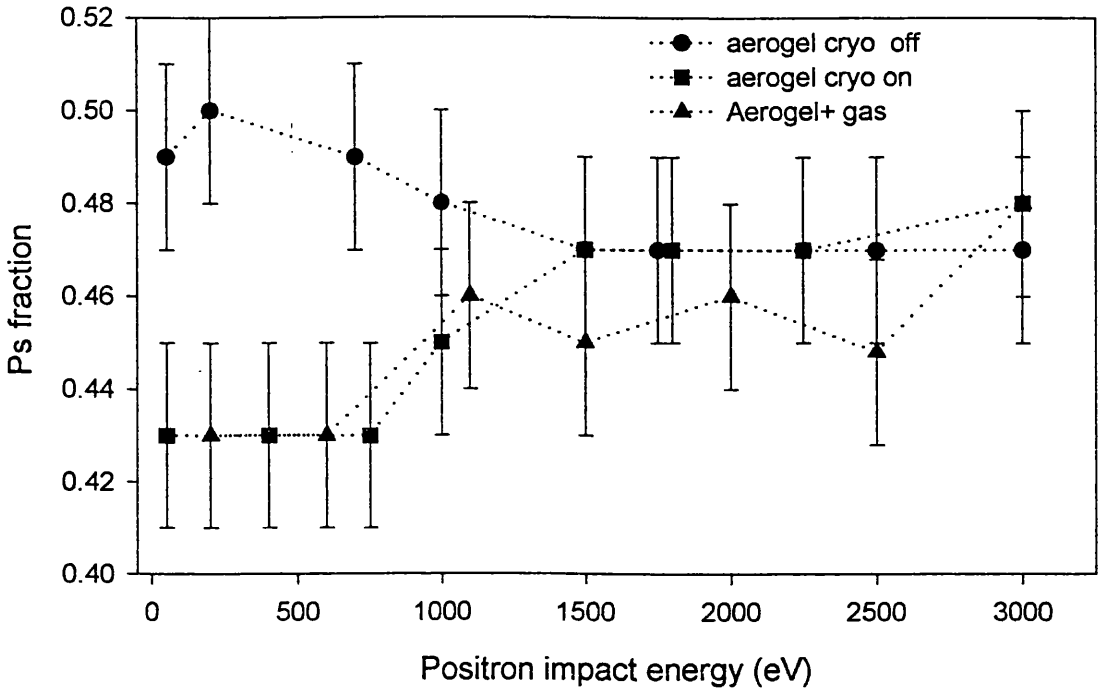

Figure 3.5 The variation of the positronium fractions with incident positron impact energy for silica aerogel

When positrons enter such materials they may be stopped in the grains and form positronium by the process described in section 1.3.1d, which may then diffuse out into the void. Figures 3.5 and 3.6 show the positronium fractions for the aerogel and MgO targets respectively. Again, for the moment we shall consider only the cryo off curves. It is clear that the positronium fraction for silica aerogel was independent of the beam energy in the range used in this work (that is, 0-3 keV).This was attributed to the form of the sample and the small grain size of the aerogel, so that deeper penetration into the bulk simply meant that positronium was formed in grains located deeper into the sample. Although this did not inhibit positronium formation, it may have prevented any such positronium from escaping back out into the vacuum (as opposed to the intergranular spaces). The small size of the grains meant that ortho-positronium could diffuse out into the void before annihilating by pick off into two photons, which would have given a reduced apparent positronium fraction. A similar argument applies to the formation of positronium in MgO, shown in figure 3.6, however in this case some energy dependence was observed. Since this sample was smoked onto the copper plate in a relatively thin layer and had large void sizes, there was a finite chance that an incident positron could simply pass through the MgO and

impinge directly on the copper, where it would be very likely to annihilate into 2 photons (particularly if, after passing through the MgO, they impinge on the Cu at energies above 500 eV, see figure 3.1).

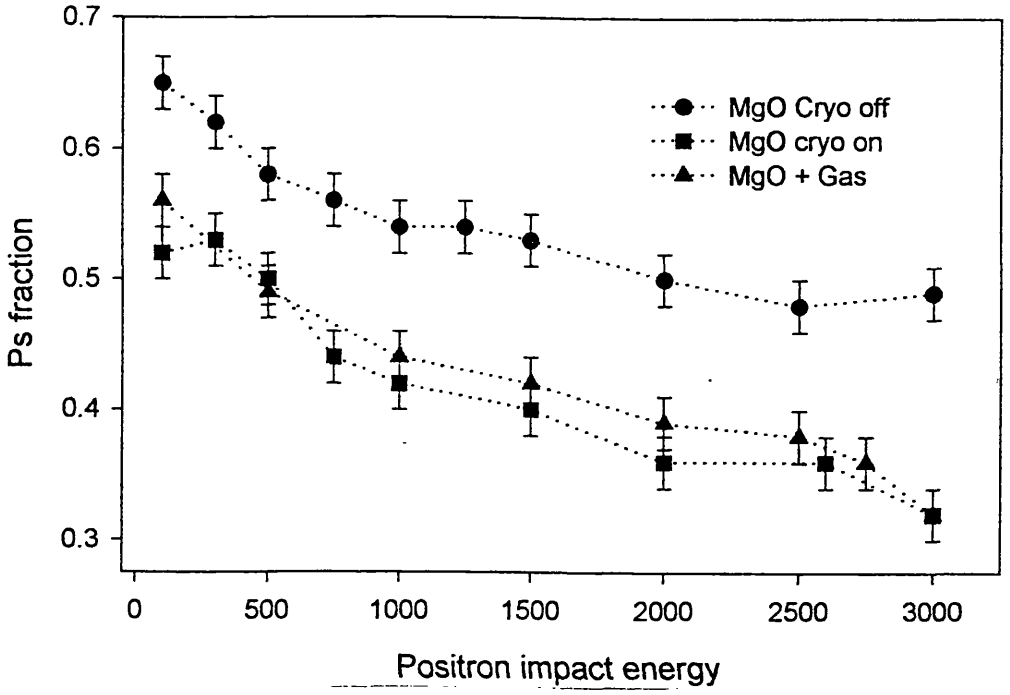

Figure 3.6 The variation of the positronium fractions with incident positron impact energy for MgO

The apparent density of the smoked MgO was ~0.05 g/cm^3 (Brandt and Paulin 1968) and so, applying equation (1.7) we find a mean implantation depth of 8000 Å/keV^n. The sample was approximately 1 x 10^7 Å thick and so the probability of any positrons reaching the copper is extremely small and it is not thought that the beam managed to penetrate through the MgO. From section 3.4 we find an apparent diffusion length of ~ 0.15 x 10^6 Å and so the energy dependence of the cryo off curve of figure 3.6 was attributed to penetration of incident positrons into grains rather than transmission or diffusion through to the copper substrate. Positronium formed deeper inside the grains may have annihilated by pick off before diffusing out to the intergranular void spaces, thus reducing the apparent positronium fraction as observed. This was not observed in the case of the aerogel target and we attribute this to the smaller grain sizes of that material, so that positronium could always diffuse out before appreciable pick off occurred.

In figure 3.5 (cryo off) we see that the presence of condensed vacuum contaminants had very little affect on the positronium fraction for the aerogel target. Similarly, the addition of N_2 gas on the sample (aerogel + gas) made no difference at all. In figure 3.6 (cryo off) the positronium fraction for the MgO fell by ~15% with the cryostat on, and again the addition of gas (MgO + gas) had no affect at all, within the counting statistics. This initial drop could have been due to a change in the diffusion length of positronium formed in the MgO grains, as a result of a decrease in the positronium diffusion constant, which is a function of temperature (see equation 34 of Schultz and Lynn 1988). This effect was not observed in the aerogel target and this could be explained by the smaller grain sizes, so that even with a reduced diffusion length ortho-positronium could still escape to the void spaces. However, since the aerogel is a very poor heat conductor it is possible that it did not cool down to temperatures sufficient to freeze out the contaminants or gas and that this is why no change was observed for that material. The systematic reduction of the positronium fraction due to a reduced diffusion length in the MgO would explain why the energy dependence of all data of figure 3.6 is the same, but the present data does not allow us to determine if this is actually the case.

For a 2 cm x 2 cm x1 mm MgO powder area and a 2 cm cubic aerogel sample the total granular surface area is ~ 0.025 and 3.5 m^2 respectively (with the sample and grain sizes quoted above). These are both enormous surface areas (the aerogel area is of the same order of magnitude of the inside of the vacuum chamber) and explain why the presence of gas on these samples did not significantly change the positronium fractions (assuming freezing took place). Although the exact amount of gas present was not known, it was very unlikely that enough gas was injected into the chamber to form a layer over such large internal surface areas, and thus no change was in the positronium fraction was observed.

3.4 Diffusion and thermalisation lengths.

In order to understand the data of the previous section, the diffusion lengths of positrons in the target materials was considered. This section contains a description of the process by which the quoted diffusion lengths were obtained. It should be pointed out that the measurement of these parameters was not the objective of this work, and the data collected

was therefore not well suited to the extraction of exact diffusion lengths. The values presented here are intended only as an approximate guide with which to investigate the nature of the measured positronium fractions.

The implantation into, and subsequent behaviour of positrons in, solid materials is described by various parameters (see section 1.3.1). One of the most important of these is the depth to which such particles reach before they become thermalised, or begin the process of thermalisation. That is, the depth at which subsequent motion is characterised by the diffusion equation (see 1.3.1c). For a monoenergetic beam such implantation will be described by a distribution about some mean depth, known as a stopping or implantation profile. The most widely used implantation profile is the Mahkovian of equation 1.8,

$$P(z) = \frac{mz^{m-1}}{z_0^m} \exp[-(z/z_0)^m] \qquad (1.8)$$

Where, m is a shape parameter (see below) and z_0 is an energy dependent parameter, related to the mean stopping depth, $\bar{z}$, by equation 1.9,

$$z_0 = \frac{\bar{z}}{\Gamma[(1/m)+1]} \qquad (1.9)$$

The value of the shape parameter, m, is usually taken to be 2, which defines a Gaussian profile (see below), although some authors have found that this value does not provide a good description of the transmission of beams through thin films (e.g. Chen et al 1985, Poulson et al 1991). The use of (1.8) in the following analysis is considerably simplified by choosing a shape parameter of unity. This shape parameter does not reproduce experimental results as well as the Gaussian ($m = 2$) or the experimentally observed value of 1.4 (McMullen 1984). However, the discrepancy is minimal in the range of most of this work (see figure 3.7 and table 3.1). So, using the exponential profile we find that (1.8) and (1.9) are reduced to

$$P(z) = \frac{1}{z_0} \exp[-(z/z_0)] \qquad (3.3)$$

and,

$$z_0 = \bar{z} \qquad (3.4)$$

respectively.

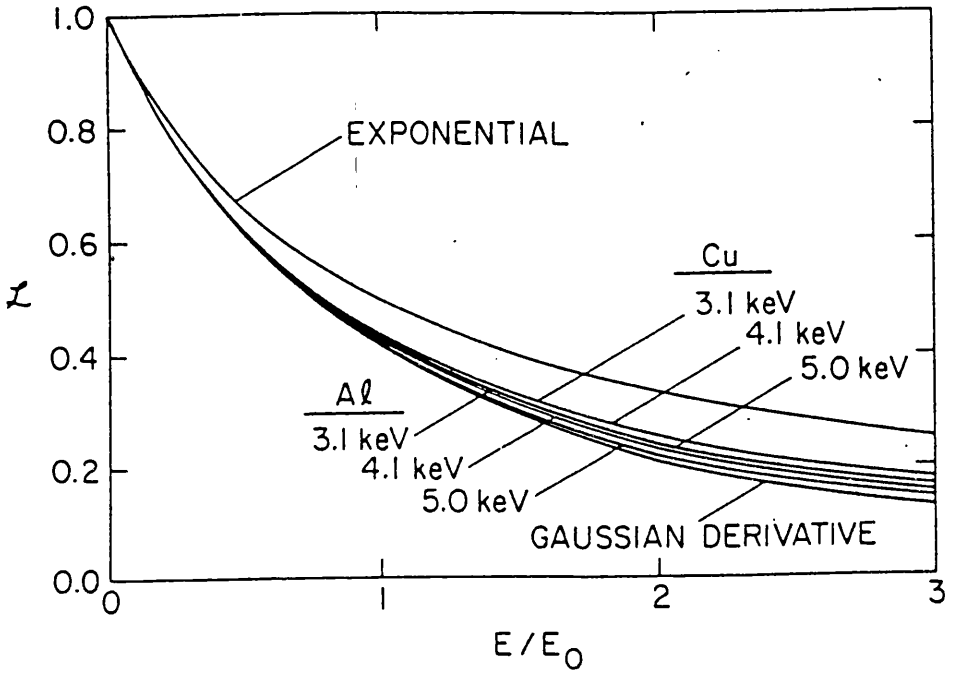

Figure 3.7 Laplace transform of positron stopping profiles and experimental results of Mills and Wilson (1982). The exponential and Gaussian profile predictions are from McMullen (1984). The use of the exponential profile is justified in this work since the energy range under consideration was such that generally $E<E_0$. The exception to this was the copper target, however the thermalisation lengths obtained were considered to be approximate.

The dependence of the mean depth with energy is assumed by Mills (1978) to be linear but later work suggests a power law (Lynn and Lutz 1980) of the form,

$$\bar{z} = AE^n \qquad (1.7)$$

with n = 1.6. The material dependent constant A was found empirically to be $400/\rho$ Å/keV^n where ρ is the material density in g/cm^3 (Mills and Wilson 1982, Vehanen et al 1987).

The number of implanted positrons that escape through the surface following back diffusion, F_s, is given by the integral,

$$F_s = \int_0^\infty P(z)N(z)dz \qquad (3.5)$$

(which is the Laplace transform of the stopping profile), where $N(z)$ is the number of positrons that diffuse back to the surface from a depth z and $P(z)$ is again the Mahkovian stopping profile. The former is obtained by solving the diffusion equation in one dimension

and integrating the positron flux through the plane of the surface (z = 0). This yields (Lynn 1981)

$$N(z) = \frac{\exp[-z / L_+]}{1 + \beta / L_+} \tag{3.6}$$

where L_+ is the diffusion length and β is the reflection coefficient at the surface. If we take this to be zero (i.e. there is no reflection) and use the shape parameter of unity the integral reduces to

$$F_s = \int_0^\infty \frac{1}{z_0} \exp[-z\left(\frac{1}{z_0} + \frac{1}{L_+}\right)]\, dz \tag{3.7}.$$

Thus, assuming the power law relationship (1.7) we find that,

$$F_s = \frac{1}{1 + \frac{E^n}{E_0^n}} \tag{3.8}$$

where E_0 is a characteristic energy defined as the energy at which half of all implanted positrons return to the surface. This is given by,

$$E_0^n = \frac{L_+}{A} \tag{3.9}$$

where A is the same constant from (1.7). If f_0 is the positronium branching ratio (i.e. the fraction of positrons that form positronium upon returning to the surface, given by the positronium fraction extrapolated to E = 0) then we may relate (3.8) to measured positronium fractions, f such that,

$$f = \frac{f_0}{1 + \frac{E^n}{E_0^n}} \tag{3.10}.$$

So, by fitting positronium fraction data to 3.10, the parameters f_0 and E_0 may be obtained, the latter yielding, from (3.9), the diffusion length. The same process may be applied to the reemitted positron fraction, where f and f_0 then correspond to the reemitted fraction and the surface branching ratio for reemission. In the case of epithermal emission the evaluation of diffusion lengths in the manner described above takes on a different physical significance. The quantity E_0 in the equations above is defined as the energy at which half of all positrons implanted diffuse back to the surface, and this is then related to the diffusion length from 3.9. In the case of epithermal emission this relationship becomes

connected to the energy loss of the positrons. Once the energy falls below that of the (positive) work function, reemission is no longer possible and so the functional form of 3.10 represents the correlation between reemission and energy loss in terms of the distance travelled in the material. This is no longer seen as the diffusion length because positrons may have a diffusion length which is in excess of the implantation depth, but may still be prevented from escaping due to the potential step at the surface. Thus, following the work of Nielsen et al (1986) and Knights and Coleman (1996) the property extracted by the process of fitting 3.10 for epithermal positrons is thought of as the *thermalisation length* (L_T). This is defined by Knights and Coleman as the mean distance travelled by epithermal positrons as their energy falls from ~ 10 eV to a value just below the work function. This assumes that the implantation profile describes positrons which have undergone some initial fast energy loss (by core electron excitation, which occurs on a time scale of ~ 10^{-13} s) down to ~10eV, but which have not begun to lose energy by slower mechanisms, such as plasmon or phonon scattering or electron/hole pair excitation, which typically occur over time scales of 10^{-12} s (see section 1.3.1, and figure 1.3). Thus, the process of thermalisation is investigated by the study of epithermal positrons in this way.

Some values of E_0 obtained from fits of Ps and reemitted positron fraction data, and the corresponding diffusion/thermalisation lengths, as well as values of A/ρ, are shown in are shown in table 3.1. The relevant fits and data are shown in figure 3.8

Target (method)	E_0 (keV)	E_0^n (keV^n)	A/ρ (Å/keV^n)	L_+ or L_T (Å)
W (Ps)	4.42	10.78	20.7	223 (+)
W(e^+)	9.02	33.75	20.7	699 (+)
Cu (Ps)	0.19	0.07	44.8	3.2 (T)
Cu (e^+)	0.30	0.15	44.8	6.5 (T)
MgO (Ps)	6.05	17.8	8000	0.15×10^6 (+)
N_2 (Ps) (Cu+gas)	3.4	17.08	341.9	2422 (+)

Table 3.1 List of targets and parameters used to determine diffusion and thermalisation lengths, denoted by (+) and (T) respectively.

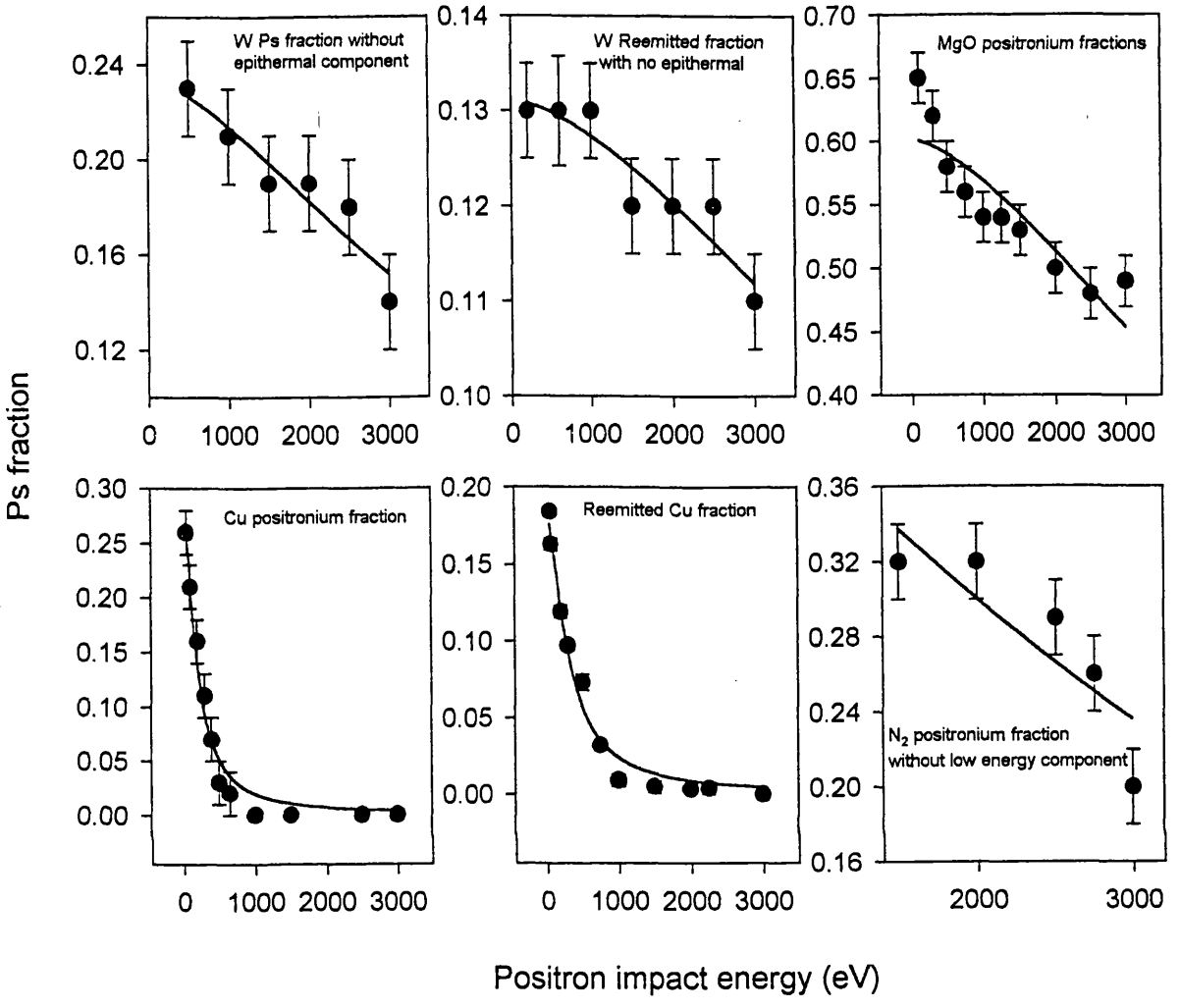

Figure 3.8 Fits to positronium and reemitted fraction data using the procedure described in the text. The values of E_0 extracted by this process are shown in table 3.1

The discrepancy between the Ps fraction determinations of E_0 and those of the reemitted fraction indicates that the former exhibit a stronger energy dependence than the latter. This could be a result of inaccuracies in the calibrations necessary to determine the absolute positronium fraction (see section 3.1), which could result in an incorrect scaling of the positronium fraction with energy. The tungsten fits were made without the lowest energy data points which may contain a contribution from epithermal positrons. However, the diffusion length of positrons in well annealed tungsten is of the order of 1000 Å, (for a diffusion coefficient of 1.5 cm^2s^{-1} (Schultz and Lynn 1988) and a typical lifetime of 10^{-10} s) so it would appear that the sample used in this work was not well annealed. Any defects

present in the sample would have resulted in positron trapping, which would have reduced the effective lifetime and hence the measured diffusion length. The copper thermalisation lengths obtained are in accord with other values of this parameter obtained for polycrystalline metals by Knights and Coleman (1996) which range from 4 to 10 Å. Again, the discrepancy between the two measurements may be due to incorrect scaling of the positronium fractions and so the reemitted fraction is likely to be more accurate. The MgO diffusion length is actually an approximation since it was obtained by treating the sample as a uniform medium with an "effective" density of 0.05 g/cm^3 (Brandt and Paulin 1968). This parameter was evaluated in order to estimate the probability of the transmission of positrons through the sample and is not expected to correspond to the actual diffusion process. The N_2 diffusion length was obtained using only data (figure 3.1 Cu+gas) above 1 keV, following Gullikson and Mills (1990), and is in reasonable agreement with the obtained by those authors (see section 3.4).

3.5 Doppler shift measurements

Using the apparatus described in chapter 2, attempts were made to measure the Doppler shift of positronium emitted from a large (10 x 10 cm) copper target following bombardment with low energy (~50 eV) positrons. This work is intended as a primary investigation into the use of Doppler-shift spectroscopy as a method to measure the kinetic energy of positronium emitted from metal surfaces. (See chapter 5 for a discussion of the relevance of such measurements to the main body of this thesis, namely the formation of low energy antihydrogen). The 511 keV photopeaks were amplified using a biased amplifier and the background underlying each peak was determined (and subtracted) using the procedure described in section 2.7. All peaks shown in this chapter have undergone this type of background subtraction and further discussion in this section is based on the understanding that all background components have been removed. The peaks were then considered to be comprised of a Doppler broadened direct annihilation component and a Doppler shifted positronium component. Since the 3-gamma annihilation of ortho-positronium produces photons with energies ranging from 0 up to 511 keV, the fraction of these photons present in the photopeak region is considered to be negligible. To see why this is we may approximate the percentage of o-Ps counts that appear in the photopeak in

the following way. If we assume that the o-Ps counts are linear up to 511 keV (see figure 1.2) then for a peak 4 keV (actual FWHM was 3.3 keV) wide the relative fraction of the o-Ps counts in the peak region is approximately "2" (for a spectrum intensity at peak normalised to 1) and the total fraction is given by 1/2 x 511 x 1 = 255.5. Therefore the fraction of all o-Ps counts present in the peak region is ~0.8%. For a total positronium fraction of 25% (appropriate to this work), ~19% of the total count rate will be due to o-Ps, and so 0.8% of these will appear in the peak. So, in short, less than 0.5% of the total peak is comprised of counts from the annihilation of o-Ps and this contribution is therefore considered to be negligible in relation to ~8% p-Ps and ~92% direct annihilation. Then the photopeak is thought of as simply a combination of the para-positronium and the (much larger) Doppler broadened components.

Now, the relative size of the p-Ps component depends on the positronium fraction, which is around 25% (see figure 3.1) for 50 eV incident positrons. The relative fractions of entire spectrum originate from direct, o-Ps and p-Ps annihilation in the following proportions

- (1-f) e^+e^- (peak),
- 3f/4 3γ o-Ps (total),
- f/4 2γ p-Ps (peak).

where f is the positronium fraction. Thus, if the o-Ps contribution is negligible, the counts in the peak will be divided into counts from only p-Ps (f_{p-Ps}) and direct (f_{dir}) annihilation thus,

$$f_{p-Ps} = \frac{f}{4-3f} \quad \text{and} \quad f_{dir} = \frac{4(1-f)}{4-3f}. \qquad (3.11\ \text{a \& b})$$

For f = 25% we therefore expect the photopeak to be comprised of components due to p-Ps and direct annihilation that have (normalised) relative areas of 0.08 and 0.92 respectively.

In this experiment the gamma ray detector was perpendicular to the beamline and the target was mounted on a rotating manipulator. Measurements were then taken with the target at ± 45° to both the beamline and the detector, such that a component of the p-Ps velocity would give rise to either red or blue shifted annihilation photons. Although this resulted in the measured shift being lower than it would have been for the face-on case, it did mean that background from the source was minimised at the detector. Also, this arrangement allowed measurements to be made for both blue and red shifts. In order to isolate the p-Ps component subtractions were made of blue from red shifted peaks. The resolution of the system was obtained from a ^{137}Cs source, which is a gamma emitter at 662 keV. The peak measured from this source had a FWHM of 13 channels. Since this peak had its centroid at channel 1732 and the 511 peak at channel 360 (for one set of runs; these numbers varied slightly as drifting occurred) we had 151/1372 = 0.11 keV per channel (± 0.0002keV, which was considered to be negligible). Thus, the FWHM energy spread of the ^{137}Cs peak was 1.43 keV and the system resolution was $\Delta E/E = 1.43/662 = 0.2\%$.

The data presented below represent a typical illustration of many independent data runs, all of which exhibit very similar characteristics. The inaccuracy inherent in the present experiments prevented the results from being rigorously quantified. It is therefore instructive here to present only one set of low energy data. For quantitative comparison, similar data is presented in which high energy (1500eV) positrons were implanted into the target. In this latter case no structure was observed. Figures 3.9a and b show the initial peaks R(1500) and B(1500) and the subtracted peak R(1500)-B(1500) for positron impact energies of 1.5 keV. Figures 3.10a and b shows similar peaks for low energy (50 eV) implantation, denoted simply by R and B. In all figures, R indicates that the target was set (arbitrarily, see figure 2.11) at + 45° and B that it was set at - 45°.

The form of the peaks shown in figures 3.9a and 3.10a which are, intrinsically, close approximations to Gaussians (see section 2.7), was due to the statistical variation of the photon counting process. Since it was very important to maintain fixed centroids (as monitored by the Cs peaks) and avoid drifting effects, the run times had to be limited to ~1500s, which was close to the longest time for which stable peak positions could be maintained. This proved to be the fundamental limitation of the experiment (see chapter 5).

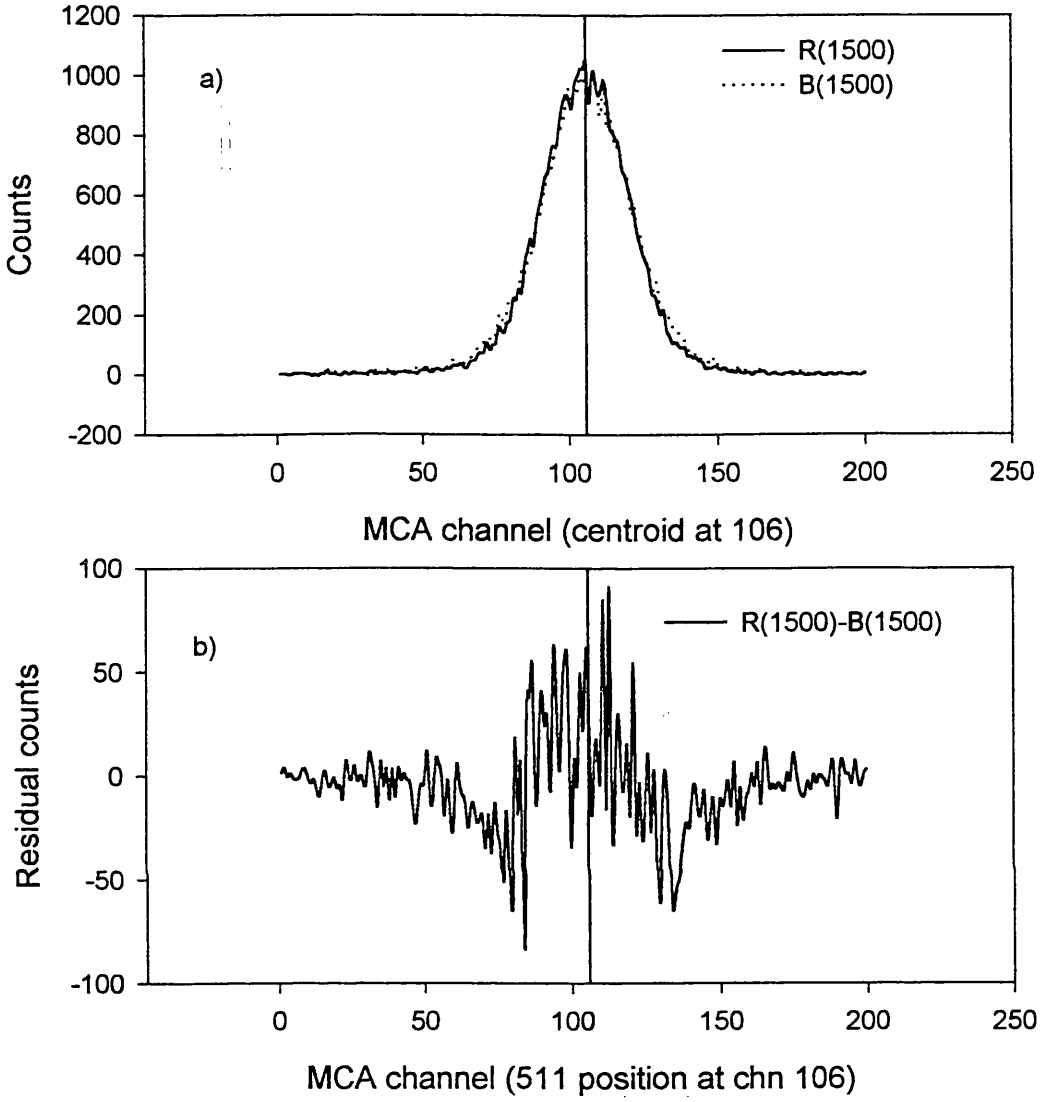

Figure 3.9 a & b, The photopeaks and subsequent subtractions for a positron impact energy of 1500 eV. The centroid position, as determined by a Gaussian fit to the photopeaks is marked with a cursor at channel 106. The structure of the subtraction is approximately the same on both sides of the cursor.

The structure of the subtraction R-B shown in figure 3.10b clearly showed a region of positive area to the left of the channel corresponding to the 511 keV position (102) and a negative region to the right of this position. This effect was not seen in the R(1500)-B(1500) subtraction of figure 3.10b, although some form of structure was apparent. The residue of figure 3.9b implies that the R(1500) peak was narrower than the B(1500), resulting in a residual peak with "dips" on either side. The reason for this may be the same as that which gave rise to a narrower redshifted component in the subtraction of 3.10b (see below). Although the regions seen in figure 3.10b were small, they were clearly present and represented the expected situation, at low positron impact energies, in which the redshifted

R peak has a slightly increased weighting to the left of the 511 keV peak and the blueshifted peak B a similar increased weighting to the right, which is negative following a R-B subtraction. A subtraction of B-R would simply exchange the "polarities" of these areas and would have been entirely equivalent to the present discussion. The choice of R-B was arbitrary. The qualitative magnitude of these areas was not expected to correspond closely to the relative areas of the p-Ps components and the total peak due to the large statistical error. It was this limitation that prevented any qualitative conclusions to be drawn from this work. It was possible, however, to demonstrate that the Doppler shift effect had actually been observed, and a very rough estimate was made of the positronium kinetic energy.

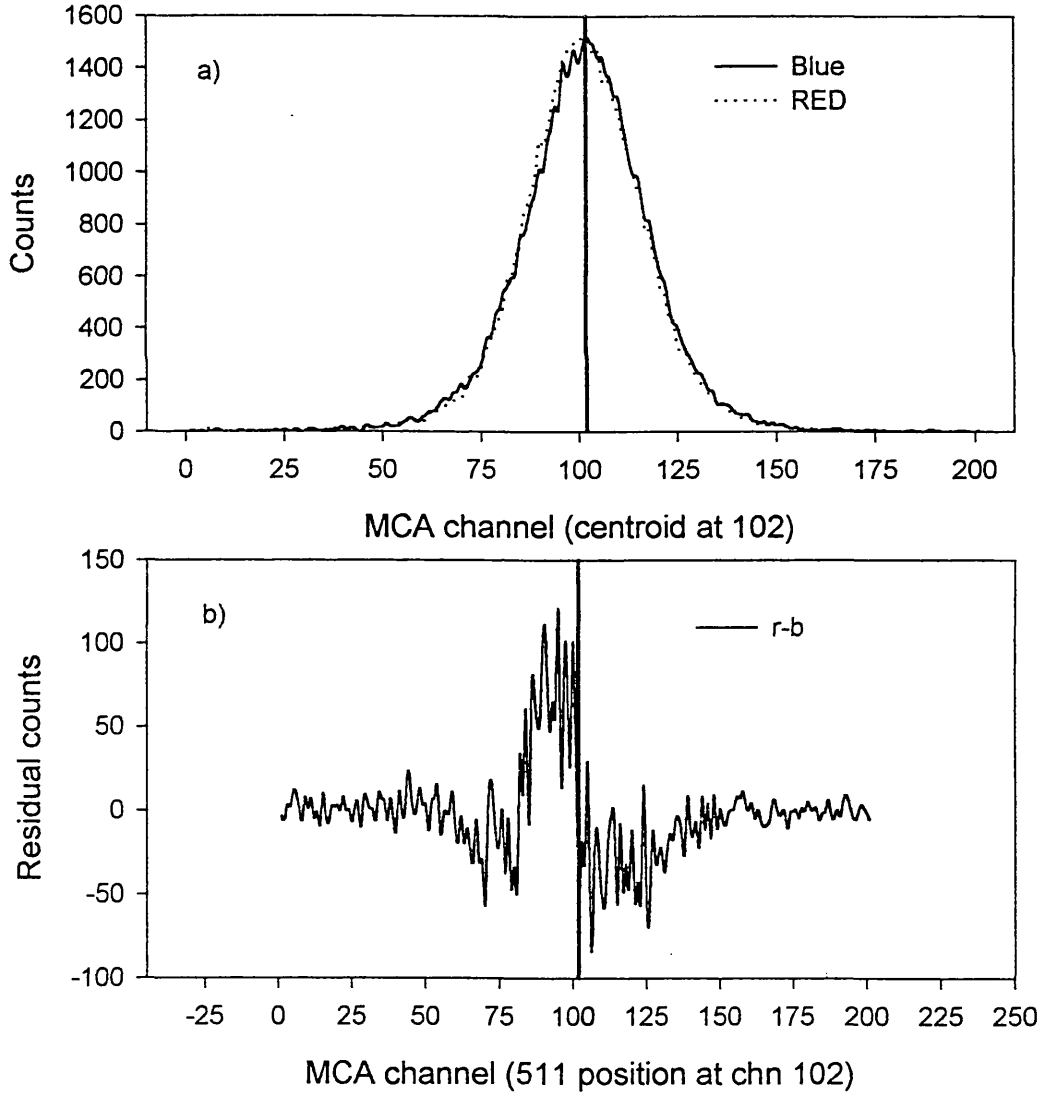

Figure 3.10 a & b, The photopeaks and subsequent subtractions for a positron impact energy of 50 eV. The centroid position, as determined by a Gaussian fit to the photopeaks is marked with a cursor at channel 102. The structure of the subtraction is different on each side of the cursor, indicating the presence of a Doppler shifted p-Ps component.

Since the structure observed for the low energy case was not present at high energies it is reasonable to attribute that structure to the Doppler shifting of the annihilation radiation of positronium. Were this not the case (for example, if the effect were the result of some zero error or a statistical residue from some of the data analysis procedures) the simple act of increasing the beam energy would not suppress the structure. However, as shown in figure 3.1, an implantation energy of 1500 eV is expected to result in a positronium fraction of zero which, if the effect is due to positronium in any way, would surely suppress the specific form of the structure, as observed. Increasing the beam energy to this level would not have any significant effect on the direct annihilation process other than changing the positronium fraction, and even if it were to do so, such an effect would not give rise to an asymmetric residual following peak subtraction. Thus, the asymmetric form of figure 3.10b, and its corresponding absence from 3.9b, is interpreted as an observation of the Doppler shifted annihilation radiation of p-Ps, within the caveats mentioned above. It is not clear why the R (left of cursor) component appears to be narrower than the B (right of cursor) component. This persistent effect may be due to the difference in the solid angle subtended by the detector for the R and B spectra measurements, so that the reduced solid angle for the R component gave rise to a lower positronium "energy acceptance". However, the difference in solid angle was small and it is not yet possible to explain this difference definitively.

From a visual inspection of the residual peaks we estimate a shift of the order of 10 channels. At 0.11 keV/chn this represented a shift of photon energy of 1.1 keV. From equation 2.10 we have

$$\frac{\Delta\lambda}{\lambda} = \frac{v}{c} \qquad (2.10)$$

where λ is the unshifted photon wavelength (2.43×10^{-12} m) and $\Delta\lambda$ is the shift in wavelength of a photon moving with speed v, as measured along the line of v. Thus, the velocity of the p-Ps perpendicular to the detector surface is given by,

$$v = \frac{hc^2}{\lambda}\left[\frac{1}{511keV} - \frac{1}{E}\right] \qquad (3.12),$$

where E is the shifted photon energy in keV. This velocity, however, is the component of the p-Ps velocity in the direction of the detector. The p-Ps velocity perpendicular to the target is thus v/sin(45) = 1.41 x v. A shift of 10 channels therefore corresponds to a positronium kinetic energy of ~5 eV. Clearly, this is an inaccurate determination but is the best that may be obtained with the present statistics. It does not seem valid to attempt any curve fitting to the two areas of the residual peak (i.e. on either side of the 511 keV position) since at least three free parameters would be required (i.e., FWHM, centroid position and amplitude) and so, with such poor statistics, the centroid determination may well be incorrect. In addition to this, the residues appear to contain only partial peaks, with a shear at the intersection of the two components. This could also give rise to a misleading centroid position.

Thus, in summary, the Doppler shift of the annihilation radiation of p-Ps has been observed and a crude estimate of ~5 eV for the kinetic energy of such positronium has been made following positron impact on a copper target at 50 eV. The obvious deficiencies of the experiment as it stands are considered in chapter 5.

Chapter 4: Monte Carlo Simulation

4.1 Program objectives

As mentioned in section 1.4.3, one method of producing low energy antihydrogen is the positronium-antiproton reaction (equation 1.18). The Monte Carlo simulation described in this chapter was developed in order to estimate the antihydrogen production rates and dynamics that may be obtained by such a reaction using the ATHENA collaboration antiproton trap, described in section 1.4.2b, and thus evaluate this reaction so that it may be compared with some of the other reactions (also mentioned in 1.4.3) under consideration. In order to perform the calculation, recent theoretical work (Mitroy 1995a, 1995b, 1996, Mitroy and Ryzhikh, 1997) regarding the formation of antihydrogen was used as input, as well as various assumptions and reported data. Details of all these input data are given in section 4.4. The full dynamics of any antihydrogen produced were needed to determine the final trapping rate, which was limited to atoms with temperatures below 1 K only, and so the program calculated total production rates, angular distributions and velocities for antihydrogen atoms in each of the states considered.

4.2 The Monte Carlo Principle

The term "Monte Carlo method" (MCM) is a very general description of statistical simulation or sampling techniques that make use of random numbers and probability distributions to model physical or mathematical systems. Such methods are used for a wide variety of applications in many different fields, from the simulation of complex subnuclear processes, stock markets and biological systems to more mundane matters such as games of chance. Strictly speaking, any method of problem solving that relies on the use of random numbers may be described as a MCM. The simplest type of MCM is a "hit and miss" integration. For example, to estimate the area of a bounded region, A, it might be enclosed by a square of side length a (and area a^2). Then if n random points are selected from inside the square and it is found that p of these points are inside A, an estimate of the area of A would be given by

$$Area \approx \frac{pa^2}{n} \qquad (4.1).$$

Another example of a MCM is the classical trajectory Monte Carlo method (CTMCM). In this case collision cross sections are evaluated by randomly selecting pre-collision system parameters, such as particle momenta and positions. The equations describing the kinematics of the system components are then integrated step by step for many initial parameters and the relative probabilities of the various outcomes are used to determine cross sections. In effect this is a model of the collision event that includes the statistical variance that would be expected in a real experiment.

In this simulation, a large number of individual positronium atom trajectories were considered step by step. The cross sections for various interactions that could take place between these particles and trapped antiprotons were known and so whenever the physical conditions made such an interaction possible these cross sections were employed to determine the outcome of that specific interaction. This invariably meant either selecting some parameter randomly but with a probability weighting (associated with the interaction, as in the case of the positronium angular distributions which were random but weighted with a cosine distribution in θ and ϕ, see sections 4.3 & 4.5.2 and figure 4.1) or by the logical initiation of a reaction subroutine (for example, the formation of an antihydrogen atom) dependent on a statement of the form

IF [random number(RN) < probability(PB)] THEN U

where U would represent a routine in which the process with probability PB actually occurs. If U doesn't occur then, typically, the trajectory will continue until the next opportunity to take part in some sort of interaction. This was, in fact, the method utilised in the case for antihydrogen formation. The probability then was determined by the total formation cross section (a function of positronium kinetic energy see section 4.4.2), the antiproton density and the distance moved through the antiproton cloud (the step length DR, see 4.3). As well as this an enhancement factor was included to reduce run times. (See section 4.4.2). "U" was then the reaction routine (see section 4.3 & figure 4.1). Other Monte Carlo selections made in the program were variations on these themes.

Any MCM is entirely dependent on the existence of a true random number generator. It should be noted that it is impossible to generate totally random numbers on a finite digital computer. Most of the algorithms available have been subjected to rigorous tests for statistical independence and usually have extremely long repetition periods ($\sim 10^{42}$) (see, for example, Youssef 1996).

4.3 Program Structure

The experimental procedure simulated by the program included an incident positron beam striking a surface (known in this context as a converter) from which positronium atoms were produced, in backscattering geometry, and emitted towards an antiproton cloud approximately 10 mm from the surface of the converter. This process was described using a positronium energy distribution obtained by the synthesis of reported distributions from aluminium for work function (Mills et al 1986) and backscattering (Howell at al 1986) emission (see section 4.4.1). The spatial distribution of the positronium atoms about the surface of the converter was taken, in the absence of detailed information regarding positronium emission angles, to be a cosine distribution. Thus, a flux of positronium with a given energy and momentum was considered to emanate from the aluminium surface.

Once these atoms encountered the antiproton cloud, total and differential cross sections (TCS & DCS, see sections 4.4.2 & 4.4.3) were employed to determine if the reaction (1.18) took place for a given interaction and, if so, the electron emission angle was determined by a Monte Carlo selection (see below). From this information it was possible to calculate the antihydrogen energy and momentum and this information was stored in data files for every antihydrogen event.

An outline of this methodology is shown in figure 4.1 which follows the path of individual positronium atoms and the possible outcomes of each trajectory. Although this diagram is a simplification of the main programming tasks, it provides an overview of the main selection procedures. Each step is explained more fully in this section.

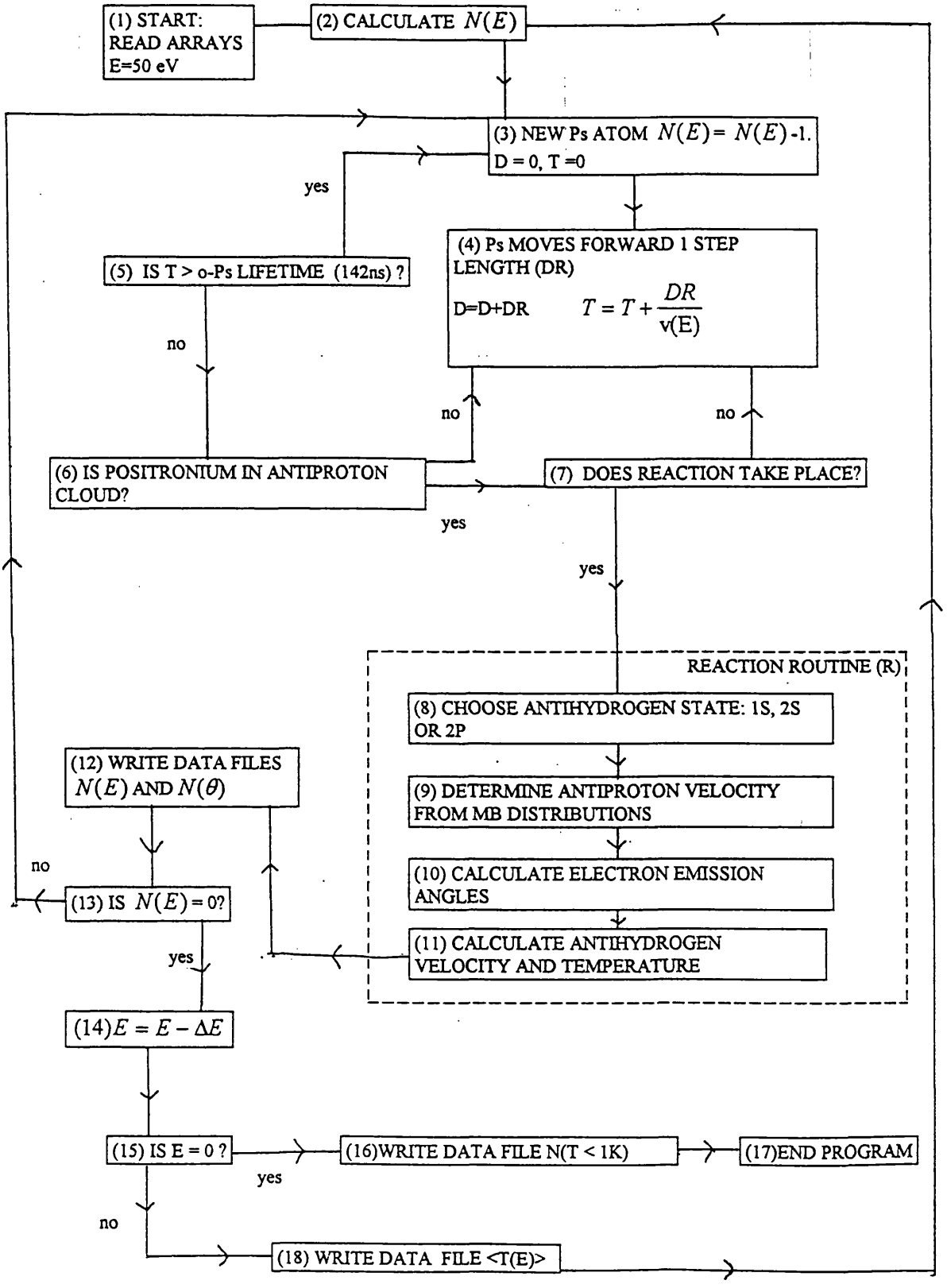

Figure 4.1. A schematic of the program methodology (see text).

1) All of the input data to the program was stored in a set of arrays, which were kept in separate files. When the program was initiated these files were read into the random access memory (RAM) of the computer so that, when necessary, the arrays could be accessed instantaneously. Had the arrays been accessed from the stored files run times would have been significantly increased. The first positronium kinetic energy was pre-set at 50 eV.
2) Having read the arrays, the positronium kinetic energy distribution and the total number of positronium atoms are used to calculate $N(E)$, the number of positronium atoms at each energy.
3) A new positronium trajectory was started by setting the time, T, and the distance, D, travelled along the vector **A** (see 4.5.2 for co-ordinate system) to zero. The space interval DR (see below) was not increased in the first step, but the direction of **A** was decided randomly against a cosine distribution weighting of θ and ϕ. The number of positronium atoms left at the energy E was then reduced by one. That is, $N(E) \rightarrow N(E) - 1$.
4) The positronium atoms were moved along **A** by one step length, (DR) set as 10^{-4} m. The time interval was also increased by an amount DT. This time interval was calculated as $DT = \frac{DR}{v_{Ps}}$ (4.2), where v_{Ps} is the positronium velocity.
5) Only o-Ps was considered in this simulation. As the time interval, DT, was increased the total elapsed time for each atom was compared to the mean o-Ps lifetime (142 ns). If this lifetime was exceeded the atom was "killed" and a new trajectory was started. If the lifetime had not been exceeded the atom was allowed to continue.
6) The motion of the positronium atoms was tracked along the vector **A** as well as along the Cartesian components x, y and z (see 4.5.2). The position of the atoms was then monitored with respect to the antiproton cloud, which was modelled to have fixed co-ordinates. A simple comparison of the positronium co-ordinates with the defined antiproton co-ordinates thus revealed whether the positronium atoms were within the antiproton region. If the positronium atoms were found not to be in the cloud the time and step lengths were increased again and the lifetime was also checked again. Also, to avoid tracking positronium atoms whose trajectories were such that no interaction with the antiprotons was possible, atoms were "killed" if they exceeded certain boundary

values of x, y and z. This procedure also took into account any atoms that passed through the cloud without interacting.

7) If a positronium atom was found to be inside the antiproton cloud, the total antihydrogen formation cross sections were used to determine if the reaction (1.18) occurred. Only antihydrogen in the states 1S, 2S and 2P were considered in this simulation so the total formation cross section used was the sum of the formation cross sections for these states. (See 4.4.2). In order to make the computing time practical the simulations were speeded up by using artificially high cross sections (enhanced by a factor of 10^7), which were then scaled down to produce the true reaction rates. Care was taken to avoid unrealistic reaction dynamics as a result of this enhancement, for example, all positronium forming antihydrogen as soon as it encounters the antiproton cloud. No discernible change was observed when the enhancement factor was deliberately varied over two orders of magnitude. If no reaction occurred, the step length and time period were increased and the time was compared with the o-Ps lifetime. If a reaction did occur the antihydrogen subroutine R was initiated.

8) The first component of R was to decide which state of antihydrogen was formed. For this the individual formation cross section for each state as a fraction of the summed formation rate was compared with a random number. In accordance with these cross sections the final proportions selected were 44% (1S), 8% (2S) and 48% (2P).

9) The antiproton velocities were assumed to be one-dimensional Maxwell-Boltzmann distributions in the y and z directions and zero in the x direction. (see sections 4.4.4 & 4.5.2). The antiproton velocity for a given reaction was thus chosen by a Monte Carlo selection from these distributions.

10) The electron emission angles were determined using the differential cross sections (see section 4.4.3) for various positronium kinetic energies. The DCS used were all for ground state antihydrogen. It was found that the excited state antihydrogen dynamics were not affected by this choice since the correct DCS for these states were quite similar. Only ground state antihydrogen was formed at temperatures low enough to enable trapping (i.e. T< 1 K), and so a detailed analysis of the excited state dynamics was not undertaken. The range of DCS available meant that only selected points were studied in the temperature minimum region (see section 4.6). The electron emission was symmetric about the initial positronium vector **A** and so the azimuthal angle ϕ' was

selected randomly with equal weight between 0 and 2π. The angle θ' was determined by a Monte Carlo selection from the DCS.

11) The antihydrogen velocities were calculated by conservation of momentum. It was assumed that all of the available energy was taken up by the electron so that the momentum of the electron, the antiproton and the positronium were known. By using a co-ordinate transformation the electron velocity was expressed in terms of the Cartesian co-ordinates of the initial positronium and so the antihydrogen velocity was also calculated in this system.

12) Having calculated the antihydrogen velocities the temperature and angle θ (see sections 4.5 & 4.6) were known and were written into a data file. In one file a record of the number of antihydrogen atoms at a given positronium energy was kept. This data eventually represented the positronium energy distribution, folded with the antihydrogen formation cross section over the same energy region.

13) After an antihydrogen atom was made, the number of positronium atoms left at the current energy ($N(E)$) was checked. If there were still trajectories left to run T and D were reset to zero and a new atom was emitted from the converter.

14) If there were no trajectories left to run, the energy was reduced by ΔE, which was set at 1 eV.

15) After reducing the energy a check was made to see if the end of the scale had been reached.

16) If there were no further energy steps, the total number of antihydrogen atoms formed at temperatures less than 1 K was stored in a data file.

17) With no more energy steps, the program closed all of the files stored in the RAM and wrote the data files to permanent stored files. The program was then terminated.

18) If there were still further energy steps the mean antihydrogen temperature for the previous step was calculated and stored in a data file. The program then returned to step (2), calculated the number of positronium atoms at the new energy and repeated the entire process.

4.4 Input data

4.4.1 Positronium energy distribution

The positronium energy distribution used for this simulation was obtained by the synthesis of reported distributions from aluminium for backscattered (Howell et al 1986) and work function (Mills et al 1986) positronium. The choice of aluminium was an arbitrary one governed simply by the availability of data. The physics behind positronium formation at surfaces by delocalised positrons is discussed more fully in section 1.3.2d but it should be noted here that, for aluminium, as with all metals and semiconductors, positronium may be formed only at the surface and cannot exist in the bulk. It is therefore more appropriate to refer to a positronium formation potential than a positronium work function (a quantity that can be defined for materials in which positronium can exist in the bulk, such as ionic crystals or molecular solids, see section 1.3.1d). This potential, ε_{Ps}, is, by conservation of energy, given by

$$\varepsilon_{Ps} = \phi_+ + \phi_- - 6.8(eV) \qquad (1.14)$$

with the symbols defined in section 1.3.2d. The composite distribution function used by the program is shown in figure 4.2. The work function and backscattering components are shown separately and are clearly as distinctly different. The contribution to the total amount of positronium formed from each of these regions is approximately equal. The former (work function) is limited to a sharp distribution, peaking at the aluminium positronium formation potential (-2.6.eV) while the backscattered component extends almost up to the positron impact energy. The overall shape of this distribution is extremely important to the final antihydrogen yields (see section 4.6). In particular, the relatively large number of low energy positronium atoms is crucial to the formation of low energy antihydrogen atoms. The area under the distribution was normalised to unity and the actual number of positronium atoms was included as a program input variable.

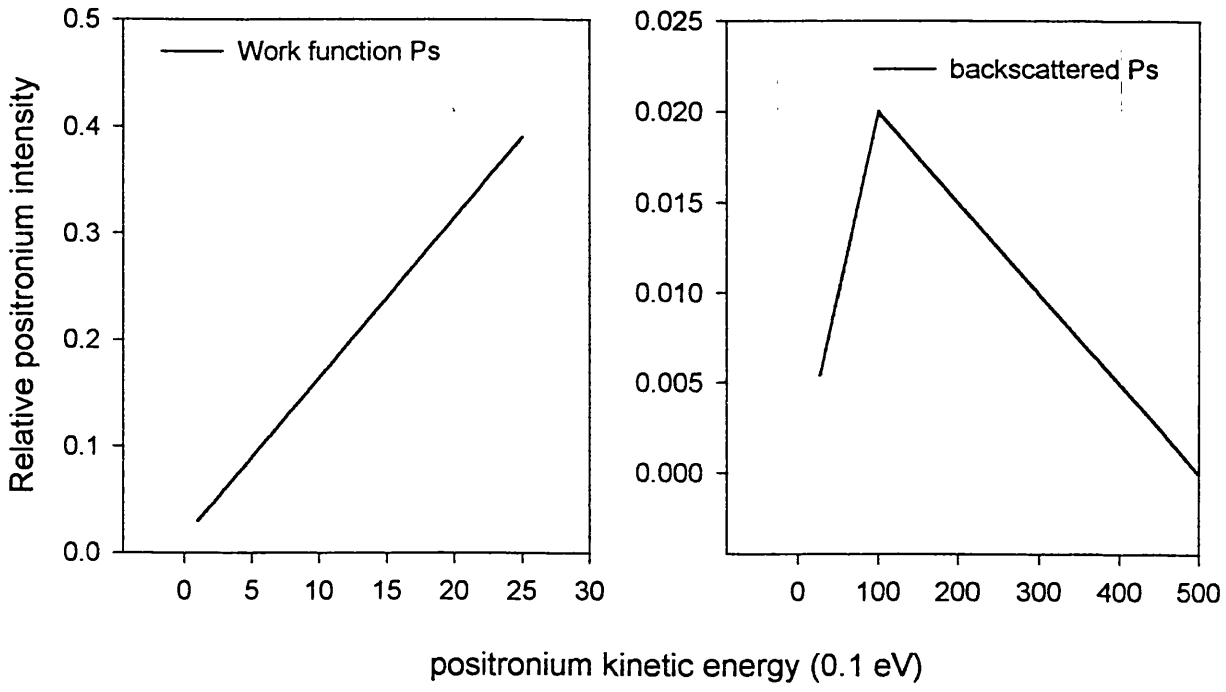

Figure 4.2 The two components of the positronium energy distribution. These figures are shown seperately for clarity.

4.4.2 Total antihydrogen formation cross sections

All of the cross sections used for these simulations were calculated by Mitroy and co-workers (1995a, 1995b, 1996, 1997) using a close-coupling (CC) approach. This is an approximation which involves writing the total scattering wavefunction as an expansion of a set of system states (known as the basis set). It is assumed that these states are closely coupled together (hence the name). This means that the N states $q = 1,2....N$ (say) in the approximate wavefunction are closely coupled together and that the influence of other states with $q > N$ is small, and is an approximation because the basis set is, in practice, never complete. Increased accuracy is obtained by the inclusion of further states (or pseudostates, see below) in this basis.

It should be noted that positron-hydrogen scattering reactions of the form

$$e^+ + H \rightarrow Ps + p \qquad (4.3)$$

are related by time reversal to

$$p + Ps \rightarrow e^+ + H \qquad (4.4)$$

which, by charge conjugation, is related to the reaction of (1.18),

$$\bar{p} + Ps \rightarrow \bar{H} + e^- \qquad (1.18).$$

This is of interest because the computations of Mitroy (and other CC calculations) allow one to specify any channel as the entrance channel, thus (4.4) and (4.3) are considered in exactly the same way. Thus, due to charge conjugation invariance, the formation of antihydrogen by positronium impact on antiprotons is included automatically in positron-Hydrogen scattering CC calculations of this nature. These calculations may also then be compared to experiment, which is not currently possible for direct calculations involving antihydrogen.

The cross sections were derived from two different model calculations; below a positronium kinetic energy of 6.8 eV, close-coupling CC(13,8) model calculations were used while CC(28,3) model calculations were used above this energy. These models differ in their basis sets, where the notation refers to the number of included states of hydrogen (or antihydrogen, see above) and positronium. This includes both exact states and what are known as *pseudostates.* These are approximate wavefunctions that either represent some average over a group of physical states (bound and continuum) or are a simplified representation of a specific state. The inclusion of such pseudostates helps to offset the effects of open channels in a system that are not included explicitly in the basis set. There is no prescribed way to choose which pseudostates to include but, generally speaking, better accuracy is obtained with further additions. The CC(13,8) basis calculations included antihydrogen physical states (1S, 2S, 2P, 3S, 3P, 3D) with 7 antihydrogen-type pseudostates (4S, 5S, 4P, 5P, 6P, 4D, 4F) and three physical positronium states (1S, 2S, 2P) with 5 positronium-type states (3S, 3P, 3D, 4S, 5S). However, only the ground state and the first two excited states of antihydrogen (1S, 2S, 2P) were considered in the simulation, and so the total formation cross section was slightly underestimated.

The CC(28,3) model calculations were somewhat different from the CC(13,8). Above the positronium formation threshold (6.8 eV) it becomes desirable to use a larger basis set since there are more open channels. For this reason calculations above this energy were performed using a basis set obtained from what is known as an L^2 or Laguerre basis. In this formalism all of the target states are constructed from a function (which depends on the size of the basis). which contains the associated Laguerre polynomials (which are simply

the derivatives of the ordinary Laguerre polynomials). All of the states are therefore pseudostates, although the basis generating function contains a free parameter which allows one to match the lowest energy states to the exact eigenfunctions (e.g. Bray and Stelbovics 1992). For the CC(28,3) Mitroy used a Laguerre basis to generate 28 hydrogen type states (11S, 9P and 8D states) and added 3 physical positronium states to the basis (1S, 2S, 2P).

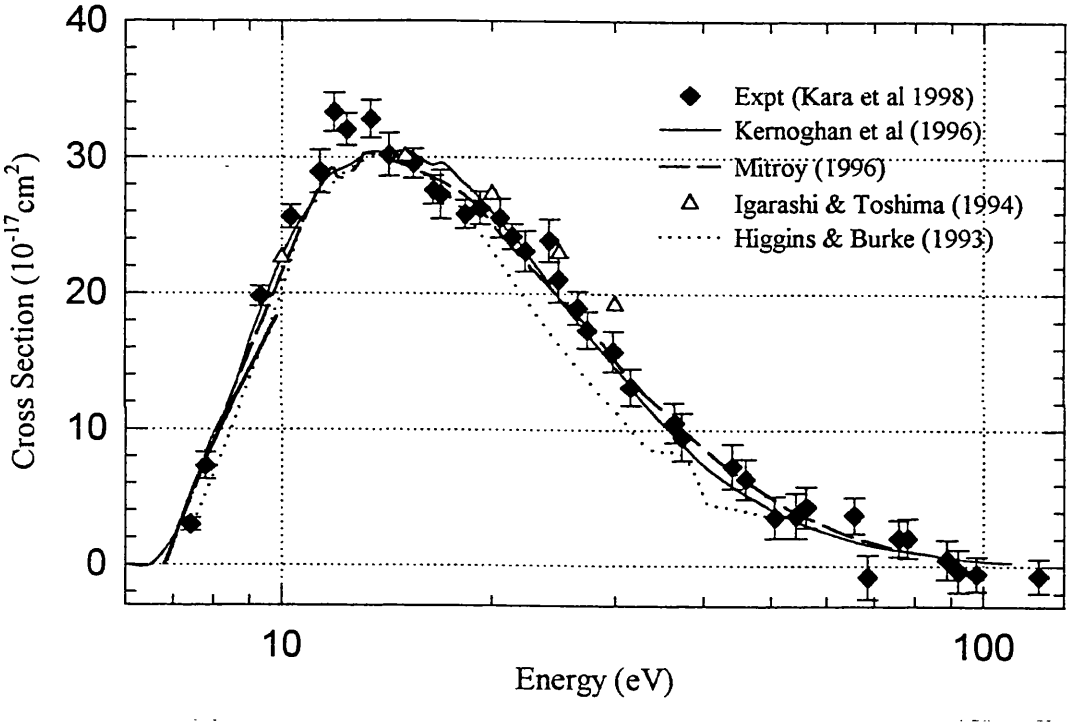

Figure 4.3 Comparison of experimental and theoretical values of σ_{Ps}, the cross section for positronium formation for positron-hydrogen scattering.

The cross sections thus calculated show good agreement with other recent calculations and with experiment, as may be ascertained from figure 4.3. The CC(13,8) calculations are expected to be within 2% of exact cross sections, as determined by accurate variational calculations (Mitroy 1996 and references therein). By extending the CC(28,3) calculations down to lower energies (i.e. < 6.8 eV) agreement with the CC(13,8) calculations indicates an accuracy of ~5% for these cross sections (Mitroy 1996)

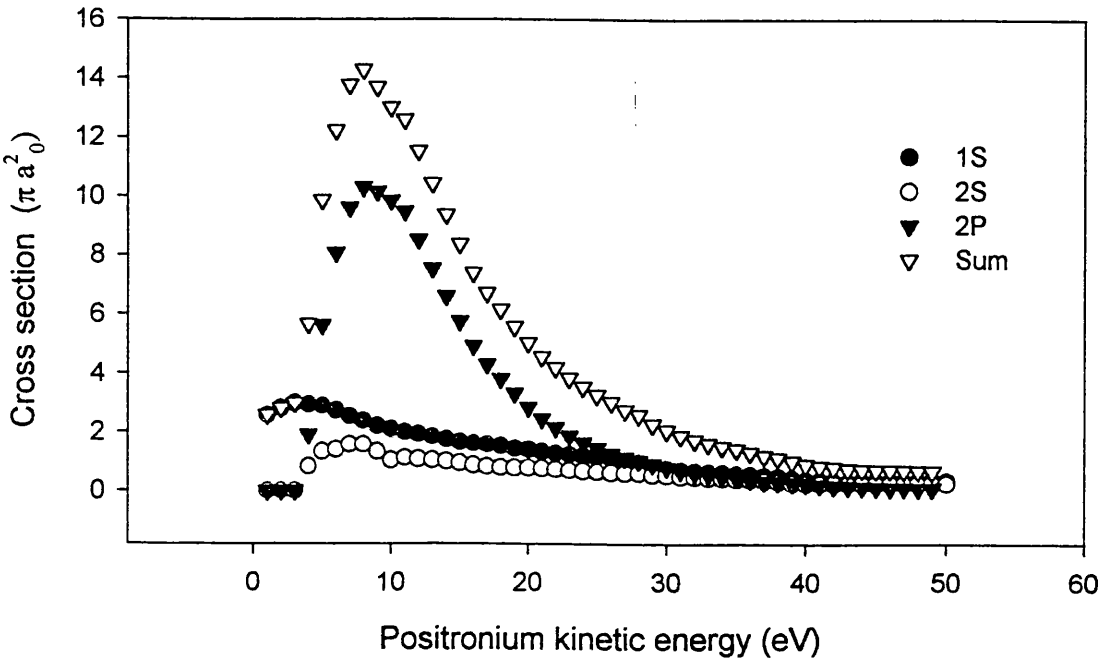

Figure 4.4. The antihydrogen formation cross sections for the first three states (with ground state positronium) and the total formation cross section. The use of only these states results in a small underestimation of the total.

The total antihydrogen formation cross sections for the three states used in the simulation are shown in figure 4.4. These were artificially enhanced by a factor of 10^7 in order to make the run times more practical, with the appropriate re-scaling afterwards.

4.4.3 Differential cross sections

The differential cross sections necessary for this simulation were produced by the same calculations as the cross sections described above. These describe the electron emission angle with respect to the direction of the initial positronium trajectory, following the formation of an antihydrogen atom by impact with a stationary antiproton. Without these cross sections it would not have been possible to calculate the dynamics of any of the reactants. A selection of the differential cross sections are shown in figure 4.5. The small differences proved to be important when a high resolution scan was performed on the low (positronium) energy region of figure 4.8. This was a result of the delicate energy balance that occurred near the equilibrium region (see section 4.6) where the recoil effects determined the final antihydrogen dynamics. These effects were due to the difference in

binding energy of the positronium and antihydrogen atoms and were found to be extremely important in the production of trappable antihydrogen

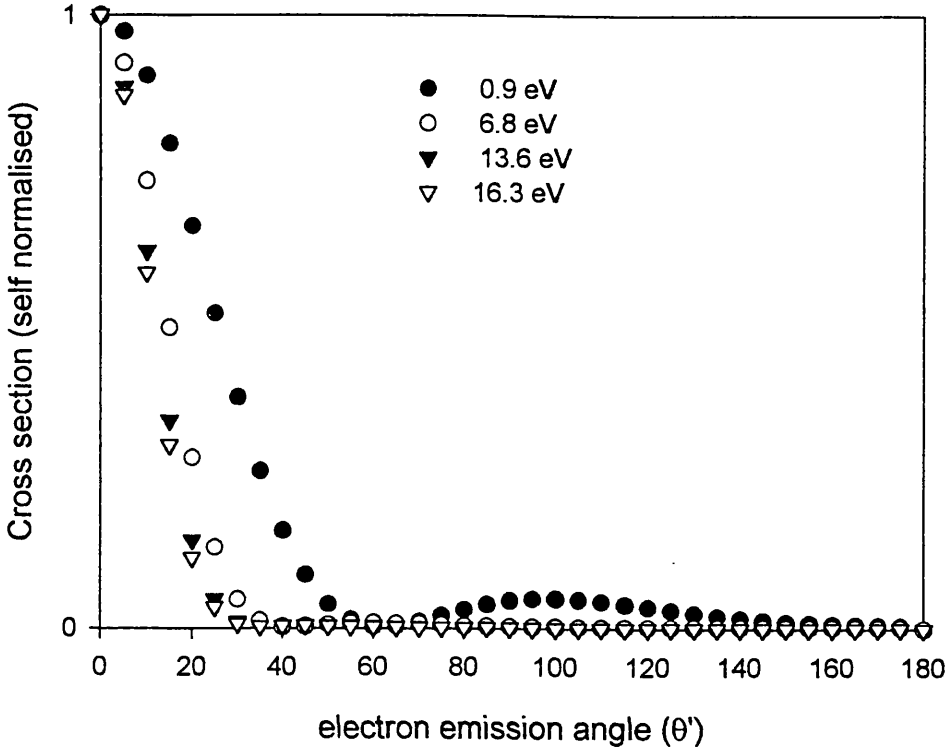

Figure 4.5. A selection of differential cross sections use in the simulation.

The DCS become increasingly forward peaked as the positronium kinetic energy increases, converging quickly after ~13.6 eV. For this reason the simulation uses the differential cross section for 16.3 eV for the energy range 16.3-50 eV.

4.4.4 Antiproton velocities

Since the antiprotons were deemed to be confined in a Penning trap and held at a constant temperature (4.2 K), the velocity distributions in the y and z directions were characterised by 1-dimensional Maxwell Boltzmann (MB). In the x direction the cloud of antiprotons were expected to move coherently (and therefore slowly) due to the harmonic potential well and the velocity in this direction is taken to be zero. (X. Feng, private communication.) The one dimensional (y direction) MB velocity distribution is given by

$$n(v_y)dv_y = \sqrt{\frac{m_{\bar{p}}}{2kT\pi}} e^{-m_{\bar{p}}v_y^2/2kT} dv_y \quad (4.5)$$

(See, for example, Reif 1985). A similar expression determines the velocity distribution for the z direction. From hereon, only the y direction will be considered, with the understanding that the same arguments apply to the z direction and that the velocity in the x direction is negligible. Figure (4.6) shows a plot of this distribution taken as output from the program. The peak is that of a Gaussian distribution (4.5 is Gaussian in nature) with a variance of $\sqrt{kT/m_{\bar{p}}}$ so that the width of the peak decreases with temperature. The centroid of the distribution is the mean velocity, which is zero as we would expect since the antiprotons have the same probability of moving in either the positive or negative directions. The actual velocity was chosen from this distribution by a Monte Carlo selection procedure. The 1-dimensional distributions are all independent, so this distribution is unaffected by the fact that v_x is zero.

The distributions were written into the code rather than included in the input data arrays to increase the simulation speed. Although the array needed for these distributions was not large, the need to write arrays into the RAM reduces the available memory therein for other operations, which then require increased processing time.

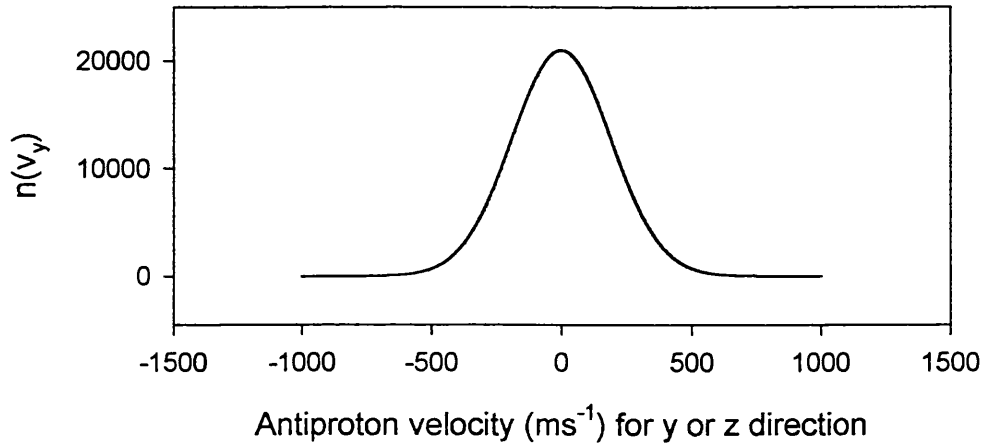

Figure 4.6 The antiproton velocity distributions for the y and z directions.

4.5 Reaction kinematics

4.5.1 Antihydrogen state selection

The decision as to whether an antihydrogen atom was created during an interaction between a positronium atom and an antiproton was based on the total formation cross section. Once an atom had been deemed to have been created it was then necessary to choose which state was made. Since only the first three states of antihydrogen were considered this selection was accomplished by a Monte Carlo selection based on the relative contributions of each states to the total cross section. These values were energy dependent (see figure 4.4) and the proportions were calculated accordingly.

4.5.2 Co-ordinate transformations

In a given reaction, knowledge of the antiproton, positronium and the emitted electron velocities enable that of the antihydrogen atom produced in the reaction to be calculated. In this case, the velocities were all known in a fixed co-ordinate system, based on the trap configuration, with the exception of that of the electron. The emission angle of this particle was determined from the DCS (see section 4.4.3) with respect to the initial positronium trajectory. It was therefore necessary to perform a co-ordinate transformation such that the electron velocities could be expressed in terms of the original system, and thus determine the antihydrogen angular distributions in that system also. Figure 4.7 shows the collision

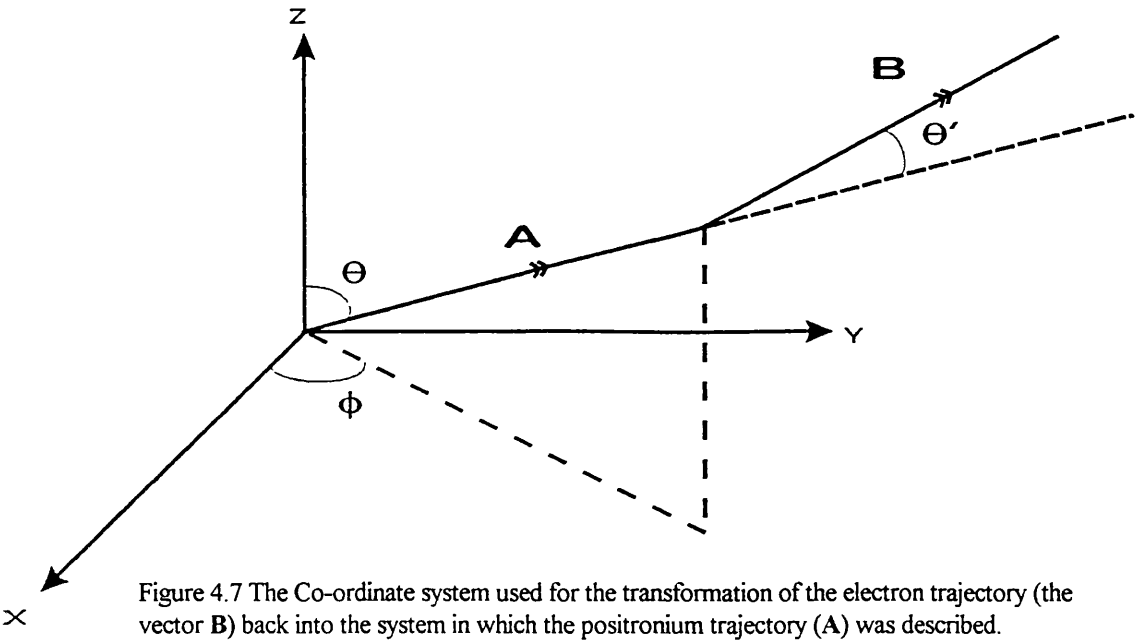

Figure 4.7 The Co-ordinate system used for the transformation of the electron trajectory (the vector **B**) back into the system in which the positronium trajectory (**A**) was described.

geometry in terms of spherical polar co-ordinates (SPC), which was the system used to perform the transformation. Note that the individual particle velocities were always tracked along Cartesian components. The SPC system was used because the electron direction was calculated in terms of an emission angle.

If the incident positronium moves along vector **A** then the electron emitted following the formation of antihydrogen will move along vector **B**, where **B** is a rotation of **A**. This rotation consists of a random and equally weighted azimuthal rotation (not shown in figure 4.7 but henceforth denoted by ϕ') and a rotation in θ determined by the DCS and denoted by θ'. To express the electron velocity in the original system it was necessary to perform a transformation between an arbitrary system, which was defined to be that in which the vector **A** was the z direction (in the new system) and the original system. This resulted in the expressions below, which were derived by J W Humberston (Private communication, see appendix 2 for the derivation) and describe the components of the electron velocity in Cartesian co-ordinates in the original system using the angles of the new system.

$$v_x = v(\cos\theta\sin\theta'\cos\phi\cos\phi' + \sin\theta\cos\theta'\cos\phi - \sin\theta'\sin\phi\sin\phi') \qquad (4.6\text{ a}),$$

$$v_y = v(\cos\theta\sin\theta'\sin\phi\cos\phi' + \sin\theta'\cos\phi\sin\phi' + \sin\theta\cos\theta'\sin\phi) \qquad (4.6\text{b}),$$

$$v_z = v(\cos\theta\cos\theta' - \sin\theta\sin\theta'\cos\phi') \qquad (4.6\text{c}),$$

where v is the electron speed. It may easily be verified that 4.6 a, b & c reduce to the usual Cartesian components in SPC when $\theta' = \varphi' = 0^\circ$.

4.5.3 Antihydrogen energy and momentum

Once the electron velocity was known in the initial frame it was possible to calculate all of the antihydrogen dynamics (by conservation of momentum). Thus,

$$v_{\bar{H}} = \frac{1}{m_{\bar{H}}}\left(m_{Ps}v_{Ps} + m_{\bar{p}}v_{\bar{p}} - m_e v_e\right) \qquad (4.7)$$

where, v and m refer to speed and mass respectively and subscripts $\bar{H}, \bar{p}, e$ and Ps refer to antihydrogen, antiprotons electrons and positronium respectively. (Note that 4.7 is the

general term and was applied separately for each Cartesian component, giving rise to three components for the antihydrogen velocity, and thus also the angular distributions). Similarly, by assuming that the electron kinetic energy is much larger than that of the antihydrogen, the electron velocity is given by,

$$v_e = \sqrt{\frac{2}{m_e}\left[\frac{m_{Ps}v_{Ps}^2}{2} + m_{\bar{p}}v_{\bar{p}}^2 + \Delta E\right]} \qquad (4.8)$$

where ΔE is the difference in binding energy between antihydrogen and positronium. Note that this is dependent on the quantum states of both species.

In order to illustrate the general character of this reaction, focusing on the antihydrogen dynamics, it is instructive to consider the antihydrogen velocity analytically. This is simplified by making a few assumptions, namely, that the electron emission angle is zero and that the antiproton velocity is negligible. These are not unreasonable since the antiprotons will have a velocity of the order of a few hundred ms^{-1} (see figure 4.6) and the average emission angle is around 20° (see figure 4.5). Then,

$$v_e^2 = 4v_{Ps}^2 + \phi^2 v_{\bar{H}}^2 - 4\phi\ v_{Ps}v_{\bar{H}} \qquad (4.9)$$

follows from conservation of momentum and whilst the conservation of energy gives,

$$v_e^2 = 2\left(v_{Ps}^2 + \frac{\Delta E}{m_e}\right) \qquad (4.10),$$

where $\phi = \frac{m_{\bar{H}}}{m_e}$. By combining these and eliminating v_e we find that

$$v_{\bar{H}}^2 = \frac{1}{\phi^2}\left[6v_{Ps}^2 + 2E' \pm 4v_{Ps}\sqrt{2\left(v_{Ps}^2 + \frac{\Delta E}{m_e}\right)}\right] \qquad (4.11).$$

Differentiating (4.11) with respect to v_{Ps} gives

$$\frac{dv_{\bar{H}}^2}{dv_{Ps}} = \frac{1}{\phi^2}\left[12v_{Ps} \pm \left\{4\sqrt{2\left(v_{Ps}^2 + \frac{\Delta E}{m}\right)} + \frac{8v_{Ps}^2}{\sqrt{2\left(v_{Ps}^2 + \frac{\Delta E}{m}\right)}}\right\}\right] \qquad (4.12).$$

If 4.12 is set to zero we find that

$$m_e v_{Ps}^2 = \Delta E \qquad (4.13).$$

That is, the antihydrogen velocity (and concurrent temperature) is a minimum when the incident positronium has a kinetic energy equal to the difference in the binding energies of the positronium and antihydrogen. For ground state antihydrogen this occurs at 6.8 eV. For the excited antihydrogen states ΔE is negative (-3.4 eV) and there is no temperature minimum. (Note that this is only true for antihydrogen formation with positronium in the ground state: see figure 4.8 for the program output data which shows the variation of all antihydrogen states as a function of ground state positronium kinetic energy). The angular distributions of antihydrogen were given with respect to the y axis such that

$$\theta = tan^{-1}\left[\frac{v_{z\bar{H}}}{v_{x\bar{H}}}\right] \qquad (4.14)$$

where $v_{z\bar{H}}$ and $v_{x\bar{H}}$ are the x and y components of the antihydrogen speed respectively.

4.6 Program output

Over the range of all positronium kinetic energies, the simulation has predicted an antihydrogen production rate of 8.4 atoms per hour with the parameters specified above, namely a primary positron beam of 10^7 e^+s^{-1} and 10^7 antiprotons trapped at 4.2 K. Of these 10% were created (in the 1S state only) with a temperature below 1 K. This corresponds to a trapping rate of roughly 20 atoms per day, although only the ground state (1S) and the first two excited states (2S, 2P) were considered in this calculation, thus underestimating the total production rate. Of these the fractions created in each state were 44% (1S), 8% (2S), 48% (2P) in accordance with the formation cross sections.

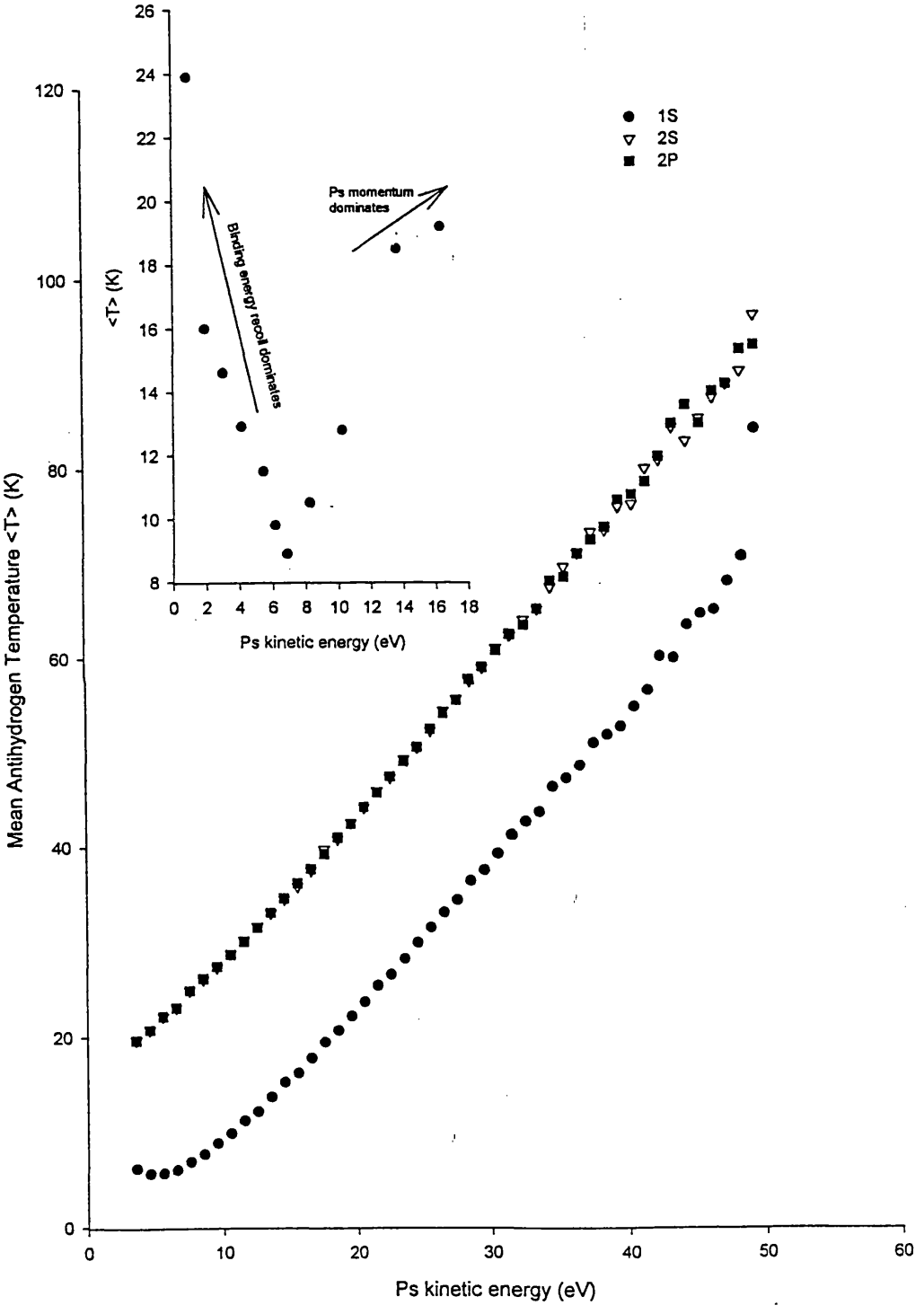

Figure 4.8 The variation of the mean antihydrogen temperature with positronium kinetic energy for each antihydrogen state and, inset, the low energy region. In the latter calculation only the specific differential cross sections are used at each energy for increased resolution, whilst average DCS were used for the low resolution scan.

The mean antihydrogen temperature as a function of the incident positronium energy was calculated and is shown in figure 4.8. The gross energy dependence is determined primarily by the increasing positronium momentum, and the onset of this behaviour is indicated in the inset, which is a high resolution calculation of the low energy region.

The energy balance (between the two regions indicated in the inset of figure 4.8) is so delicate near the minimum that only the exact cross sections show the correct structure. For this reason only a limited number of points could be calculated. At lower positronium kinetic energies, the differential cross sections tend to be less forward peaked, which results in correspondingly higher mean antihydrogen temperatures, countered of course by the overall reduction in positronium momentum. It is in this region where the recoil momentum caused by the 6.8 eV difference in the binding energies of (ground state) positronium and (ground state) antihydrogen becomes important.

So, a temperature minimum occurs when the momentum of the emitted electron is equal to that of the initial positronium. Then neglecting the antiproton momentum, the antihydrogen will have zero momentum, and hence the mean temperature will be zero. We expect only an approximation to this and so there will be a non-zero minimum temperature corresponding to the case where the difference in the momentum of the positronium and the electron is at some minimum level.

The positronium kinetic energy at the antihydrogen temperature minimum was expected to be near 6.8 eV (see section 4.5.3). It may be seen from figure 4.8 that this is very close (within the grid point energy resolution for which the differential cross sections were calculated) to the value found in the simulation. When the positronium kinetic energy is below 6.8 eV the momentum of the emitted electron is greater than that of the positronium, due to the difference in binding energies of ground state antihydrogen and positronium, and so the antihydrogen must absorb the excess by recoiling in the opposite direction to the electron, thus increasing its mean temperature, as shown in figure 4.8. It has been pointed out (Deutch et al 1993) that, for ground state antihydrogen and positronium, the limiting temperature (that is, for $v_{Ps} = 0$ and stationary antiprotons) is 28.6 K, which is approached in figure 4.8. Excited state antihydrogen is created only above the threshold positronium

kinetic energy (3.4 eV) at a mean temperature of ~20 K which increases monotonically with positronium energy.

The behaviour described above also gives rise to the angular distribution shown in figure 4.9, which is that of the antihydrogen atoms created throughout the positronium energy range 0-50 eV. Recoiling antihydrogen (formed by positronium with energies less than 6.8 eV) always moves in the direction of the converter and, since a large fraction of the antihydrogen atoms are created when the positronium energy is below this level, we find that the ground state antihydrogen is preferentially produced in the "backscattered" direction. The excited state antihydrogen, with a binding energy less than that of positronium, does not experience this recoil effect and is therefore produced entirely in the forward direction.

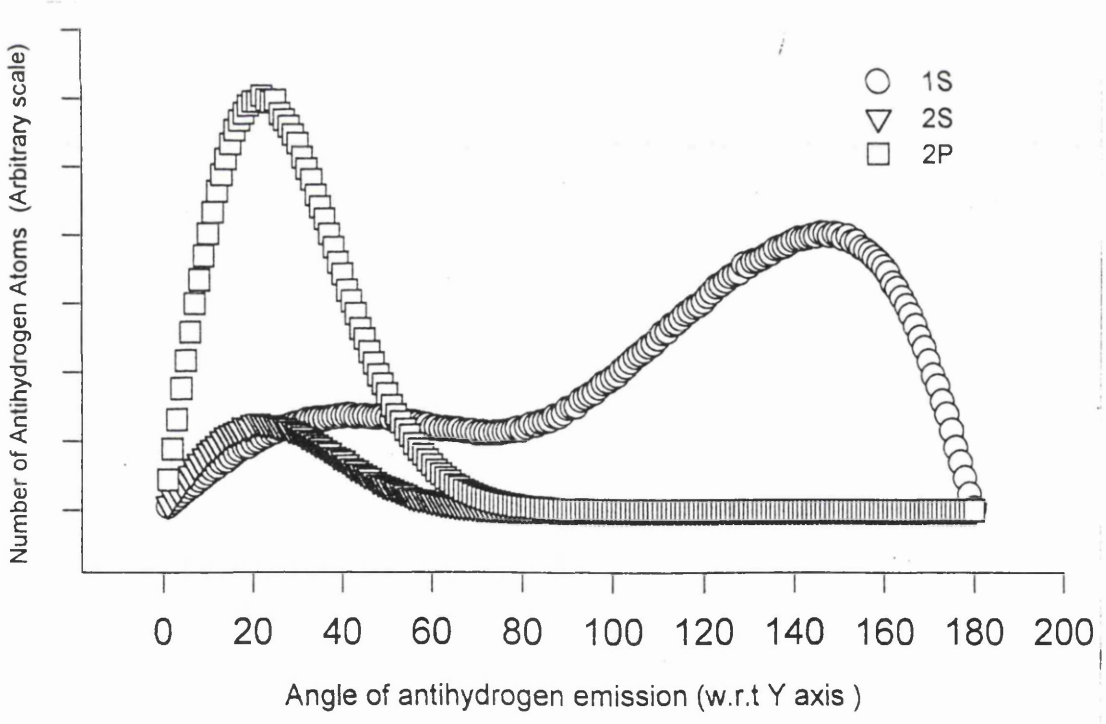

Figure 4.9 The anisotropic angular distributions of each antihydrogen state considered. The low energy backscattered antihydrogen atoms are formed predominantly in the ground state, while the excited states are produced only in the forward direction. (see text).

5 Conclusions

5.1 Experiments

The formation of positronium following positron impact on metal and metal oxide targets has been measured for incident positron energies in the range 0-3 keV and at cryogenic temperatures. These measurements indicate that the formation of positronium is largely unaffected for metal oxide materials (of the form described in chapter 3) when the temperature is reduced and material is condensed onto them. For metal targets this is not the case and the presence of material on the surface plays a more important role. In the context of positronium formation for antihydrogen production the need for a cryogenic environment may be used as an advantage. If it is necessary to implant positrons at a high energy (ie, a few keV) the formation of positronium in the condensed material itself could provide a higher fraction than would be possible for a "clean" material, as in the case of copper. Since the tungsten data is not yet understood it is not possible to draw any firm conclusions, but it is possible that the effect observed is the result of some physical process that warrants further study in its own right.

The experimental work described in this thesis has provided unexpected, and as yet unexplained, data. The formation of positronium from tungsten with N_2 gas condensed on the surface is, compared with similar data from copper, still a mystery. It is, however, one that may be resolved by further, more systematic, studies. In order to ascertain exactly what affect the presence of N_2 on metal targets has on the positronium fractions it would be desirable to apply the gas layers in small increments. This may then allow a better determination of where positronium formation occurs for such an arrangement. It would also be useful to compare a wider range of target materials, with both positive and negative work functions to see if the negative work function of the tungsten is the cause of the anomaly. In this way various factors can be eliminated and the effect studied in detail. The Doppler shift spectroscopy experiments have provided a preliminary description of a relatively easy method of measuring the kinetic energy of positronium emitted from metal surfaces. The main drawback with this work was the short run times, and correspondingly poor statistics, that were necessary. The obvious answer to this problem would be the use of a digital stabiliser. The detector-target orientation used provides an oportunity to confirm

any measurements made since the positronium kinetic energy so obtained should be the same in both cases. Longer runs would allow a detailed investigation of the redshifted and blue shifted peaks and may explain why different lineshapes for the two were observed in this work. In addition to this, if the p-Ps components can be extracted with accuracy their areas may be compared with those of the photopeak and positronium fractions may inferred. This would provide a relatively easy method of measuring both Ps fractions and Ps kinetic energies simultaneously without the need for any calibrations. Unfortunately time and equipment limitations have prevented some of these studies from being undertaken.

5.2 Simulation

The motivation behind the simulation described in this chapter was to evaluate the antihydrogen production and trapping rates that may be expected from the positronium based reaction 1.18. Within the limitations imposed on the calculation (see below) this has been achieved, although the predicted creation of only 20 cold antihydrogen atoms per day is rather low. The implications of this for ATHENA (see section 1.4.1) are clear; another method must be considered or steps must be taken to improve this rate. In fact, since no reaction scheme has been proven by experiment, (for antiparticles, the charge conjugate of reaction 1.18 has been observed by Merrison et al, 1997) other methods are being considered, although they have been described only in passing in this work (see section 1.4.3). However, there are difficulties associated with some of these other methods which make the use of the positronium reaction desirable. (See Holzscheiter and Charlton 1998 for a general review of low energy antihydrogen, including alternative reaction schemes). It is of interest to note that problems with plasma confinement, which is necessary in some form for all schemes of low energy antihydrogen production, have recently come to light. At high densities, the inter-particle description of these plasmas is dominated by Coulomb forces to the extent that they are effectively shielded from the external trapping fields. The usual rotation about the magnetic field lines of individual particles is thus better described by the rotation of the strongly coupled plasma as a rigid body. Since the angular momentum of this body is conserved, confinement is aided by this effect. If a torque is introduced to such rotation, perhaps by field alignment errors or interactions with residual gas atoms, the

angular velocity may be reduced. To conserve angular momentum the radius of the rotating body must then increase and this could lead to a loss of particles on the wall of the chamber. This process is not problematical as far as the positronium reaction is concerned. The number of trapped antiprotons envisaged for this scheme ($\sim 10^7$) is sufficiently low to allow a fluid description of the plasma. Also, the rotation is slow in this case and the field alignments/chamber pressure have not caused any detectable deconfinement effects (Holzscheiter and Charlton 1998). In fact long term storage of $\sim 10^7$ electron cooled antiprotons has become a routine undertaking (see section 1.4.2 b&c). Problems do arise, however, in the three body recombination scheme 1.21 which is the most viable alternative to the positronium reaction. Here it is envisaged that a confined cloud of $\sim 10^9$ positrons will be merged with an antiproton cloud similar to that of the positronium reaction. This raises two main points. Firstly, the positron plasma will be very dense and so the rotation effect cannot be ignored. In order to combine two opposite charge species (i.e. antiprotons and positrons) a nested trap configuration is being considered in which one charge species is stored in an elongated potential well which has, at its centre, an inverted potential well. This means that the overall field is azimuthally asymmetric and this will exacerbate the deconfinement effect described above. Another problem is that when the two plasmas are merged the rotation of the positron cloud will induce rotation in the antiproton cloud. Thus, any antihydrogen that is produced will be more energetic and difficult to trap. For these reasons it is desirable to consider techniques that may lead to an improved rate using the positronium reaction.

The simulation was performed using only ground state positronium but it has been shown (Charlton 1990) that large enhancements in the antihydrogen production rate may be obtained when highly excited positronium atoms are used, although the antihydrogen produced in this way is formed in a high Rydberg state. Although the simulation predicted that only ground state antihydrogen was produced at energies low enough to be trapped, this is only the case when the positronium used is in the ground state. The production rate for antihydrogen formation by reaction 1.18 is expected to increase (Charlton 1990) as $\sim n_{Ps}^3$, where n_{Ps} refers to the principal quanrtum number of the positronium. In addition to this, the trapping rate per atom should increase as well with excited state positronium. High n_{Ps}

positronium atoms will preferentially produce antihydrogen atoms of a comparable energy (assuming the antiprotons are cold) with a principal quantum number, $n_{\bar{H}}$, of $\sqrt{2}n_{Ps}$ in order to conserve momentum, and the recoil effect seen with the low energy 1S antihydrogen is avoided. Therefore, investigations should be made regarding the efficient production of excited state positronium in an environment similar to that of the antiproton trap. An interesting suggestion regarding this matter has been made by Hessels et al (1998). They have pointed out that, by using laser excited alkali-metal atoms in a Rydberg state, a charge exchange process with cold trapped positrons may be initiated, thus producing Rydberg positronium, which may be used to produce antihydrogen in the same way as described above. CTMC calculations have predicted an instantaneous production rate of 10^6 antihydrogen atoms per second using this method. Otherwise it may be possible to laser excite positronium to high n_{Ps} states (see, for example, Ziock et al 1989).

The assumed angular distribution of the positronium considered in this simulation (see section 4.3) was very important to the calculation in that it determined how many of the emitted positronium atoms actually encountered the antiproton cloud. The inclusion of data from direct measurements of angular distributions of positronium emitted from surfaces (whatever state of positronium is considered) would improve the accuracy of the calculation. Any such measurements should be carried out at cryogenic temperatures since the distributions are likely to be affected by the presence of absorbed species on the converter.

In summary, the final trapping rate of ~20 atoms per day that has been predicted by the simulation is too low for realistic spectroscopy and steps should be taken to improve this rate. Due to difficulties associated with other methods the positronium based reaction of 1.18 is one of the best prospects for the formation of low energy antihydrogen, if only the production rate can be improved. It is thought that this may be achieved by using Rydberg positronium from either a two stage Rydberg charge transfer method or by direct laser stimulation. The prospects for this, as well as the possibility of circumventing the plasma confinement problem, are currently being considered by the ATHENA collaboration.

Appendix 1: The prediction of antimatter

The existence of antimatter became known when Dirac (1930a) wrote a relativistically covariant form of the Schrödinger wave equation (SWE) and found that, in this formalism, there were two distinct energy solutions. Before considering the work of Dirac it is of interest to look at a previous attempt to formulate a relativistic analogue of the single particle Schrödinger equation, the Klein-Gordon equation (KGE). This will clarify just why the Dirac equation has the form it does. The following treatment considers free particles only. That is, no potential terms appear in the Hamiltonian. This means that non-relativistic energy (E) is given by

$$\mathrm{E} = \text{Kinetic Energy} = \frac{p^2}{2m} \qquad \text{(A1.1)}$$

Where p refers to momentum and m to mass. To obtain the SWE one must apply the substitutions

$$\mathrm{E} \rightarrow \mathrm{i}\frac{\partial}{\partial t} \qquad \text{(A1.2a)}$$

$$\mathrm{p} \rightarrow -i\nabla \qquad \text{(A1.2b).}$$

(This appendix makes use of natural units $\hbar = c = 1$). By making such substitutions one necessarily introduces the concept of a dynamic function particle descriptor since (A1.2) are operators and must act on some function. We interpret this as a wavefunction. Thus, for a wavefunction ψ, (A1.1) becomes

$$i\frac{\partial \psi}{\partial t} = -\frac{\nabla^2 \psi}{2m} \qquad \text{(A1.3)}$$

which is the SWE. Now, if relativity is to be considered the energy expression (A1.1) must be replaced with the relativistic energy expression,

$$\mathrm{E}^2 = \mathrm{m}^2 + \mathrm{p}^2 \qquad \text{(A1.4)}$$

Then, if the same substitutions (A1.2) are applied to (A1.4) we obtain

$$\nabla^2 \psi - \frac{\partial^2}{\partial t^2}\psi = m^2 \psi \qquad \text{(A1.5)}$$

which is the KGE, where ψ is again the wavefunction on which the operators are assumed to act. Just as with the SWE one may derive a conservation law for a probability current for the KGE. The probability density ρ contains time derivatives of ψ and, for a free particle is approximately proportional to the energy (e.g. Guidry 1991) i.e.:

$$\rho \sim E = \pm\sqrt{\mathrm{p}^2 + \mathrm{m}^2} \qquad \text{(A1.6)}$$

One can see straight away that the KG equation admits to both negative energy solutions and to negative values in the probability density. These problems led to this theory being initially discarded.

Dirac managed to turn the presence of negative energy solutions into an advantage but he still had to eliminate the negative probability densities. Since these were seen to be due to the second order time derivatives in the KGE, and, since in relativity space and time enter on the same footing, Dirac reasoned that

difficulties such as negative probability densities would not occur in an equation which was of first order in both space and time derivatives. Such an equation maybe obtained by replacing (A1.4) with

$$E \rightarrow \alpha p + \beta m \qquad \text{(A1.7)},$$

where α and β are coefficients to be determined. Then after making the usual substitutions, one obtains the Dirac wave equation

$$i\frac{\partial \psi}{\partial t} = \left(-\alpha \nabla + \beta m \right) \psi \qquad \text{(A1.8)}.$$

In order to be a valid wave equation this must be Lorentz invariant and consistent with the relativistic energy expression of (A1.4) and it must also forbid negative probability densities. It can be shown that this is not possible if α and β are numbers, but that it is if they are 4x4 noncommuting matrices satisfying the conditions shown in (A1.9). (See, for example, Guidry 1991)

$$\alpha_1^2 = \alpha_2^2 = \alpha_3^2 = \beta^2 = 1 \qquad \text{(A1.9a)}$$

$$\{\alpha_i, \alpha_j\} \equiv \alpha_i \alpha_j + \alpha_j \alpha_i = 2\delta_{ij} \qquad \text{(A1.9b)}$$

$$\{\alpha_i, \beta\} \equiv \alpha_i \beta + \beta \alpha_i = 0 \qquad \text{(A1.9c)}$$

where, δ_{ij} is the Dirac delta function and the unit vector is represented by $1 = \begin{pmatrix} 1 & 0 & 0 & 0 \\ 0 & 1 & 0 & 0 \\ 0 & 0 & 1 & 0 \\ 0 & 0 & 0 & 1 \end{pmatrix}$.

One choice of these matrices which will satisfy (A1.9) is

$$\alpha_1 = \begin{pmatrix} 0 & 0 & 0 & 1 \\ 0 & 0 & 1 & 0 \\ 0 & 1 & 0 & 0 \\ 1 & 0 & 0 & 0 \end{pmatrix} \qquad \alpha_2 = \begin{pmatrix} 0 & 0 & 0 & -i \\ 0 & 0 & i & 0 \\ 0 & -i & 0 & 0 \\ i & 0 & 0 & 0 \end{pmatrix}$$

(A1.10).

$$\alpha_1 = \begin{pmatrix} 0 & 0 & 1 & 0 \\ 0 & 0 & 0 & -1 \\ 1 & 0 & 0 & 0 \\ 0 & -1 & 0 & 0 \end{pmatrix} \qquad \beta = \begin{pmatrix} 1 & 0 & 0 & 0 \\ 0 & 1 & 0 & 0 \\ 0 & 0 & -1 & 0 \\ 0 & 0 & 0 & -1 \end{pmatrix}$$

If (A1.8) has matrix coefficients the wavefunction must be of the form,

$$\psi = \begin{pmatrix} \psi_1 \\ \psi_2 \\ \psi_3 \\ \psi_4 \end{pmatrix} \qquad \text{(A1.11)}.$$

One can see that the Dirac equation corresponding to (A1.10) is a matrix equation representing four simultaneous differential equations. If we consider a stationary free particle (that is, p = 0) then, from (A1.8), we find that,

$$H\psi = i\frac{\partial\psi}{\partial t} = \beta m\psi \qquad \text{(A1.12).}$$

This corresponds to 4 simultaneous differential equations, (n=1,2)

$$i\frac{\partial\psi_n}{\partial t} = m\psi_n \ , \qquad i\frac{\partial\psi_{n+2}}{\partial t} = -m\psi_{n+2} \qquad \text{(A1.13).}$$

The solution to these equations is

$$\psi_n = u_n \exp\{-imt\}, \quad \psi_{n+2} = u_{n+2}\exp\{+imt\} \qquad \text{(A1.14a)}$$

which may be written,

$$\psi = \exp\{-imt\}\begin{pmatrix} u_1 \\ u_2 \\ 0 \\ 0 \end{pmatrix} + \exp\{imt\}\begin{pmatrix} 0 \\ 0 \\ u_3 \\ u_4 \end{pmatrix} \qquad \text{(A1.14b)}$$

where u_n (n=1,2,3,4) represent the zero momentum (p=0) eigenspinors. Recall from (A1.8) that the total energy is given by,

$$E\psi = i\frac{\partial\psi}{\partial t} = \beta m\psi, \qquad \text{(A1.15)}$$

i.e. $E(\psi_n) = m$ (+'ve energy) (A1.16a)

$E(\psi_{n+2}) = -m$ (-'ve energy) (A1.16b)

The probability density derived (e.g., Itzykson and Zuber, 1980) from the Dirac equation is shown in (A1.17), and is clearly positive definite at all times.

$$\rho = |\psi_1|^2 + |\psi_2|^2 + |\psi_3|^2 + |\psi_4|^2 > 0 \qquad \text{(A1.17)}$$

Now, although there are no longer problems with probability densities, the negative energy solutions seen previously in the KGE (see above) remain. This is inevitable if an energy expression of the form (A1.4) is used, as it is here (A1.7). Dirac applied his equation to the electron and proposed a Hole Theory to explain the negative energy solutions. He assumed that the negative energy states were usually full and that free electrons, being fermions, were prevented from occupying such states by the Pauli Exclusion Principle. This set of filled negative energy states is now called the Fermi sea. If this sea were tranquil then it would exhibit no observable effects. However, the tranquillity of the Fermi sea is disturbed by quantum fluctuations of the vacuum and by interactions with radiation, and so there are observables associated with it.

The positive states are almost all empty and so an electron could be excited from a negative energy state to an unoccupied positive energy state, either by real physical processes or by virtual fluctuations, leaving a "hole" which would behave exactly like a positively charged electron. This process is known as pair production. Dirac initially suggested that the Coulomb force between the electrons in the (filled) negative energy states would lead to an energy correction that would make the "hole" appear to have a greater rest mass than an electron and that it was in fact a proton. It was quickly realised (Weyl, 1931) that the "hole" particle must have the same rest mass as the electron. No such particle was known at the time so the theory had predicted a new particle, with the same mass as the electron and an equal and opposite charge - the positron. (Dirac 1930a).

Similarly, an electron could, with the emission of radiation, fall from a positive energy state into a hole. This process is known as annihilation since it effectively involves the annihilation of the electron and the hole (positron). Fig (A1.1) shows the production of an electron-positron pair in the Fermi sea (perhaps due to an incident photon, which is not shown).

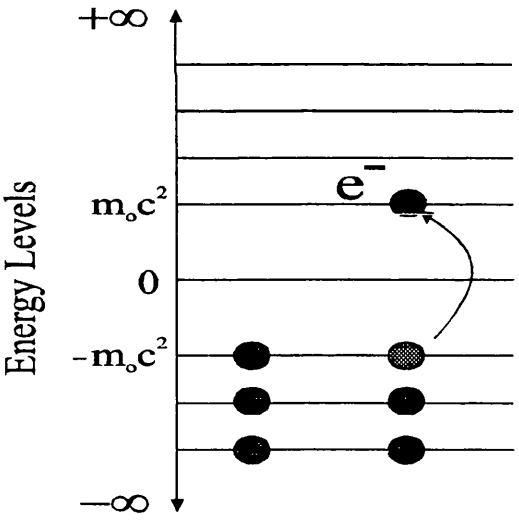

Fig(A1.1) The excitation of a negative energy electron to a positive energy, leaving a hole in the fermi sea which is intwerpreted as a positron. (Garner 1997 PhD thesis).

Another observable property of the Fermi sea is the phenomenon of vacuum polarisation. Because of quantum fluctuations the Fermi sea is awash with virtual electron-positron (hole) pairs. So, if a positive energy electron exists in this medium it will polarise it An electron would then attract virtual positrons and so the electron charge will be shielded when viewed from a distance. Thus, a (hypothetical) probe would encounter an effective charge unless it were to operate at very short distances, where the bare electron charge would reappear. Since all electrons are immersed in the Fermi sea the effective charge is that measured in all experiments.

Dirac had taken what had initially seemed to be a fatal flaw in his theory and turned it into one of its greatest triumphs. With hindsight we can see that a wavefunction of the form shown in (A1.11) is necessary because it must describe both a particle and its antiparticle (both of them having two spin states) simultaneously. It may also be said that the mass energy equivalence of relativity gave a hint at the phenomena of pair production, from which the existence of antimatter could, in principle, be inferred. However, the importance of the work of Dirac remains clear.

There is another interpretation of the negative energy solutions of the Dirac equation. The hole theory used to explain the solutions is only valid for fermions, since the exclusion principle does not prevent bosons from occupying the lower energy states ad infinitum. The second interpretation is due to Stückelberg (1941) and Feynman (1949). In this description the negative energy solutions moving backward in time are equivalent to positive energy solutions moving forward in time, where only negative energy particles can move backwards in time, and vice-versa. This interpretation does not distinguish between fermions and bosons. It is a consequence of the observation that

$$\exp[-i(-E)(-t)] = \exp(-iEt), \qquad \text{(A1.18)}$$

since a plane wave solution of a single particle wave equation may have a form like (A1.18), so clearly the wavefunction of a particle would be the same whichever side of (A1.18) was included. We may consider, for example, an electron scattering event with two separate space-time diagrams, shown in figs A1.2.a and A1.2.b

In fig 1.2.a we see a non-relativistic scattering event in which an electron is scattered from two potential sites (V). In this, and subsequent, diagrams we assume that time is increasing vertically. We see the electron moving forwards in time between scattering events. However, in the relativistic quantum mechanics of Stückelberg and Feynman there is another interpretation.

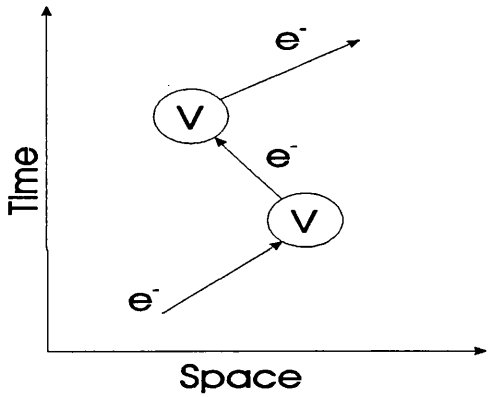

Figure (A1.2a). Second order scattering event in nonrelativistic quantum mechanics.

If we consider the possibility of particles moving backwards in time we must then allow for space-time diagrams like that shown in fig (1.2.b). Here the electron is scattered backwards in time and is assigned a negative energy . We can also interpret this diagram as fig (1.2.c). The particle moving backwards in time is equivalent to the antiparticle moving forwards in time with positive energy. In such diagrams the emission of an antiparticle with momentum p is equivalent to the absorption of a particle with momentum -p, and vice versa. This viewpoint allows processes involving only antiparticles to be converted into equivalent processes involving only particles by changing the signs of all antiparticle momenta (actually, 4-momenta) and reversing the role of entry and exit states for the antiparticle lines (i.e., by changing the directions of the arrows.) In other words, positrons in this interpretation are thought of as electrons moving backwards in time.

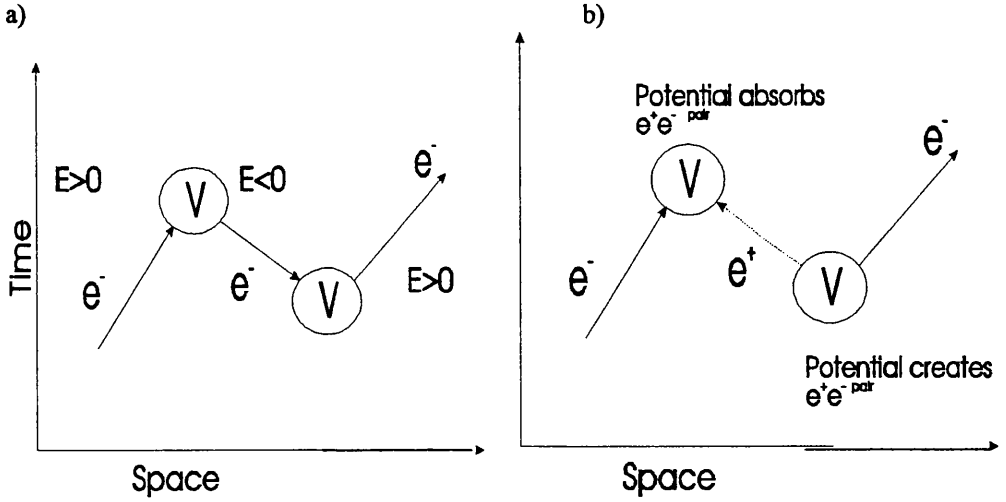

Figures (1.2.b) & (1.2.c) show a backward in time process that contributes to the mechanism shown in figure (1.2a). (b) is described by relativistic quantum mechanics whilst (c) represents the Feynman reinterpretation of the same process.

Appendix 2: Derivation of the co-ordinate transformations of chapter 4.

This appendix contains of the derivation of equations (4.6a - 4.6c) due to J Humberston, with embellishments for the sake of clarity.

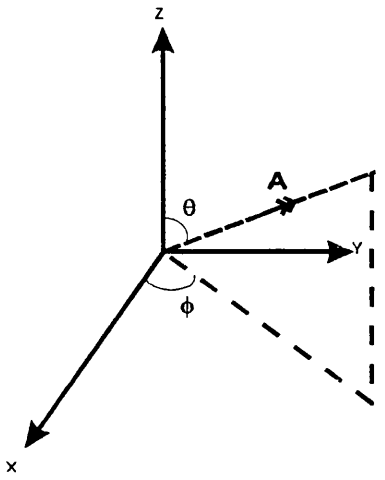

Figure A2.1 The spherical polar co-ordinate system. The vector **A** is identified with the incident positronium direction (see section 4.5.2.)

Consider first the standard spherical polar co-ordinate system (SPC), as shown in A2.1.

The standard (but arbitrary) choice of the definitions of θ, the polar angle and ϕ, the azimuthal angle place the z axis in a "privileged" position. (It is for this reason that the treatment below begins with a choice of a new z axis.) The Cartesian components of **A** may be written in terms of the SPC co-ordinates, and it is immediately obvious that the z component of **A** is independent of ϕ and is given by

$$z = A\cos\theta \qquad \text{(A2.1)},$$

where A is the length of the vector **A**. Similarly, we note that the projection of A into the x-y plane is given by $A\sin\theta$ and the x and y components are thus given by

$$x = A\sin\theta\cos\phi \qquad \text{(A2.2)}$$

and

$$y = A\sin\theta\sin\phi \qquad \text{(A2.3)}$$

respectively. Note that if A is unity A21.1 -A2.3 are the unit vectors along these axes.

We now turn our attention to figure A2.2, which is similar to figure 3.n with the inclusion of a new arbitrary co-ordinate system, the Cartesian axes of which are denoted by the unit vectors, **x'**, **y'**and **z'**. The definition of the relative orientation of these axes is chosen to exploit the properties of the SPC system alluded to above, which

are a result of the choice of the initial SPC angles. Thus, the direction of **A** is taken as the new z axis, defined by the unit vector **z'**. We can therefore say that, in terms of the fixed Cartesian unit vectors, **i, j** and **k**,

$$\mathbf{z'} = \mathbf{i}(x) + \mathbf{j}(y) + \mathbf{k}(z) \qquad \text{(A2.4)}$$

or,

$$\mathbf{z'} = \mathbf{i}(\sin\theta\cos\phi) + \mathbf{j}(\sin\theta\sin\phi) + \mathbf{k}(\cos\theta) \qquad \text{(A2.4a),}$$

since **z'** is in the direction of **A.** Then **x'** is defined as the unit vector perpendicular to **z'** in the plane defined by **z'** and z. Thus, in a similar manner as above, it may be seen that the **k** component of the unit vector **x'** is independent of the azimuthal angle ϕ and is given by $-\sin\theta$ (negative because the **k** direction is along that of positive z). Also, the projection of **x'** into the x-y plane is described by $\cos\theta$ and so we find that

$$\mathbf{x'} = \mathbf{i}(\cos\theta\cos\phi) + \mathbf{j}(\cos\theta\sin\phi) + \mathbf{k}(-\sin\theta) \qquad \text{(A2.5).}$$

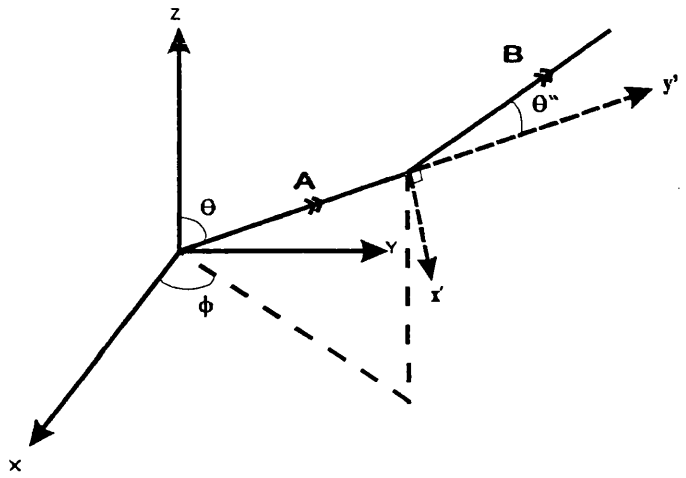

Figure A2.2 The spherical polar co-ordinate system including the rotated co-ordinate system denoted by the primed unit vectors.

Finally the unit vector, **y'**, is perpendicular to both **x'** and **z'** and is therefore given by,

$$\mathbf{y'} = \mathbf{z'}\times\mathbf{x'} = \begin{vmatrix} \mathbf{i} & \mathbf{j} & \mathbf{k} \\ \sin\theta\cos\phi & \sin\theta\sin\phi & \cos\theta \\ \cos\theta\cos\phi & \cos\theta\sin\phi & -\sin\theta \end{vmatrix} \qquad \text{(A2.6).}$$

Thus, we find that,

$$\mathbf{y'} = \mathbf{i}(-\sin^2\theta\sin\phi - \cos^2\theta\sin\phi) - \mathbf{j}(-\sin^2\theta\cos\phi - \cos^2\theta\cos\phi) + \mathbf{k}(\sin\theta\cos\theta\sin\phi\cos\phi - \sin\theta\cos\theta\sin\phi\cos\phi) \qquad \text{(A2.7)}$$

Or,

$$\mathbf{y'} = \mathbf{i}(-\sin\phi) + \mathbf{j}(\cos\phi) + \mathbf{k}(0) \qquad \text{(A2.8)}$$

Now, a unit vector **B'**, along **B** (which is a rotation of the vector **A** through the angles θ'' and ϕ', although the latter is not shown in figure A3.2) is associated with the direction of the emitted electron (see section 4.5.2). If the angles through which **A** is rotated into **B** (the double primed angles, corresponding to the differential cross

section/rotational symmetry) represent the direction of **B** in the co-ordinate system defined by **x'** **y'** and **z'**then the unit vector in this direction is given by,

$$B' = \sin\theta''\cos\phi''\mathbf{x}' + \sin\theta''\sin\phi''\mathbf{y}' + \cos\theta''\mathbf{z}' \qquad \text{(A2.9)}.$$

By substitution of A2.5, A2.4a and A2.8 into A2.9 we obtain,

$$\begin{aligned} B' = {} & \sin\theta''\cos\phi'' \; [\cos\theta\cos\phi\,\mathbf{i} + \cos\theta\sin\phi\,\mathbf{j} - \sin\theta\,\mathbf{k}] \\ & + \sin\theta''\sin\phi''[-\sin\phi\,\mathbf{i} + \cos\phi\,\mathbf{j} + 0\mathbf{k}] \\ & + \cos\theta''[\sin\theta\cos\phi\,\mathbf{i} + \sin\theta\sin\phi\,\mathbf{j} + \cos\theta\,\mathbf{k}] \end{aligned} \qquad \text{(A2.10)}$$

Which becomes,

$$\begin{aligned} B' = {} & \mathbf{i}\,[\cos\theta\sin\theta''\cos\phi\cos\phi'' - \sin\theta''\sin\phi\sin\phi'' + \sin\theta\cos\theta''\cos\phi] \\ & + \mathbf{j}\,[\cos\theta\sin\theta''\sin\phi\cos\phi + \sin\theta''\cos\phi\sin\phi'' + \sin\theta\cos\theta''\sin\phi] \\ & + \mathbf{k}\,[\cos\theta\cos\theta'' - \sin\theta\sin\theta''\cos\phi''] \end{aligned} \qquad \text{(A2.11)}$$

Equation A2.11 is equivalent to equations (4.6 a-c). As expected, the various components all vanish to their equivalent forms shown in equations A31-3 (with A = unity) when there is no rotation of the polar and azimuthal angles. (that is, for the case when the directions of both **A** and **B** are the same).

References

Adkins G S, Ann. Phys. (NY) 146 (1983) 18

Anderson C D, Science 76 (1932a) 238

Anderson C D, Phys Rev 41 (1932b) 405

Anderson C D, Phys Rev 43 (1933) 491

Baker J A, Chilton N B, Jensen K O, Walker A B and Coleman P G, Appl Phys. Lett 59 (1991) 2962

Baur G, Boero G, Braukskiepe S, Buzzo A, Eyrich W, Geyer R, Grzonka D Hauffe J Kilian K, LoVeter M Macri M, Moosburger M Nellen R, Oelert W, Passaggio S, Pozzo A, Röhrich K, Sachs K, Schepers G, Sefzick T, Simon R S, Stratmann R, Stinzing F and Wolke M, Phys Lett. B368 (1996) 251

Beling C D, Simpson R I, Stewart M G, Charlton M, Jacobsen F M, Griffith T C Moriarty P and Fung S, Appl. Phys A 42 (1987) 111

Blackett P M S and Occhialini G P S, Proc Roy Soc London A 139 (1933) 699

Blanford G, Christian D C, Gollwitzer K, Mandelkern M, Munger C T, Schultz J and Zioulas, Phys. Rev. Lett. B 368 (1998) 3037

Brandt W and Paulin R, Phys. Rev. Lett. 21 (1968) 193

Brandt W and Paulin R, Phys. Rev. B 15, (1977) 2511

Bray I and Stelbovics A T, Phys. Rev. A 45 (1992) 6995

Britton D T, Huttenen P A, Mäkinen J, Soininen E and Vehanen A Phys. Rev. Lett 26 (1989) 2413

Carbotte J P and Arora H L, Can. J Phys 45 (1967) 387

Canter K F, Coleman P G, Griffith T C and Heyland G R, J Phys B 5 (1972) L167

Chaglar I, Rice Evans P, El Khangi F A R and Berry AA, Nucl. Instr. Meth. 187 (1981) 581

Chang T, Tang H, and Li Y (1985a) "Positron Annihilation" ed P c Jain, R M Singru and K P Gopinathan (Singapore World Scientific)212

Chang T, Tang H and Li Y in ICPA85 (1985b) 212

Charlton M, Phys. Lett. A 143 (1990) 143

Charlton M, Eades J, Horváth D, Hughes R J and Zimmermann C Phys. Rep. 241 (1994) 65

Chen D M, Lynn K G, Pareja R and Nielsen B, Phys. Rev. B 31 (1985) 4123

Cherry W, PhD Thesis (1958) Princeton University

Coleman P G, "Slow Positron Interactions with Metal Samples" ed. A Ishii Trans Tech Switzerland (1993) 171

Costello D G, Groce D E, Herring D F and McGowan J W, Phys Rev B 5 (1972) 1433

Dale J M, Hulett L D and Pendyala S Surf. Int. Anal 2 (1980) 199

Deutch B I, Charlton M, Holzscheiter M H, Hvelplund P, Jørgensen L V, Knudsen H Laricchia G, Merrison J P and Poulsen M R, Hyperfine Interactions 76 (1993) 153

Dirac P A M, Proc Royal Soc A 126 (1930a) 360

Dirac P A M, Proc Camb Phil Soc 26 (1930b) 361

Dupasquier A and Zecca A Riv. Nuovo Cimento 8 (1985) 3

Eötvös RV, Pekar D and Fekete E, Ann. Phys. (Liepzig) 68 (1922) 11

Feng X, Holzscheiter M H, Charlton M, Hangst J, King N S P, Lewis R A, Rochet J and Yamazaki Y Hyperfine Interactions 109 (1997) 145

Feynman R P, Phys. Rev. 76 (1949) 749, 769

Gabrielse G, Fei X, Orozco L A, Tjoelker R L, Haas J, Kalinowsky H, Trainor T A and Kells W, Phys. Rev. Lett. 65 (1990) 1317

Garner A J, PhD thesis University College London (1997)

Goodyear A, Knights A P and Coleman P G, J Phys. Condens. Matter 6 (1994) 9601

Gramsch E, Throwe J and Lynn K G, App Phys Lett 51 (1987) 1862

Greaves R G, Tinkle MD and Surko C M Phys. Plasmas 1 (1994) 1439

Guidry M "Gauge Field Theories, An Introduction With Applications" (1991) John Wiley & Sons, INC

Gullikson E M and Mills A P Jr Phys. Rev. Lett 57 (1986) 376

Gullikson E M, Mills A P Jr and Murray C A, Phys. Rev. B38 (1988) 1705

Gullikson E M and Mills A P Jr, Phys. Rev. B 42 (1990) 7695

Hessels E A, Homan D M and Cavagnero M J, Phys. Rev. A 57 (1998) 1668

Higgins K and Burke P G, J Phys. B 26 (1993) 4264

Hodges C H, Phys. Rev. Lett. 25 (1970) 284

Holzscheiter M H and Charlton M, Rep. Prog. Phys (1998) in press

Howell R H, Rosenberg I J and Fluss M J, Phys Rev B 34 (1986) 3069

Hughes R J and Holzscheiter M H, J Mod. Opt, 39 (1992) 263

Hutchins S M, Coleman P G, Stone R J and West R N, J Phys B 20 (1986) 282

Igarashi A and Toshima N, Phys. Rev. A (1994) 232

Itzykson C and Zuber J, "Quantum field theory" McGraw Hill New York (1980)

Jacobsen F M and Lynn K G, Phys. Rev. Lett 76 (1996) 4262

Jorch H H and Campbell J L, Nucl. Instr. Meth. 143 (1977) 551

Jorch H H, Lynn K G and McMullen T Phys. Rev. B 30 (1984) 93

Kern J, Nucl. Instr. and Meth. 79 (1970) 233

Kernoghan A A, Robinson D R J, McAlinden M T and Walters H R J J Phys. B 29 (1996) 2089

Knights A P and Coleman P G, J Phys. Condens. Matter 7 (1995a) 3485

Knights A P and Coleman P G, J Phys. Condens. Matter 7 (1995b) 6477

Knights A P and Coleman P G, Surf. Sci. 367 (1996) 238

Lahtinen J, Vehanen A, Huomo H, Mäkinen J, Huttunen P, Rytsölä K, Bentzon M and Hautojärvi P, Nucl. Instrum Methods B 17 (1986) 73

Lang N D and Kohn W, Phys Rev B 1 (1970) 4555

Lowy D N and Jackson A D, Phys. Rev. B 12 (1975) 1689

Lynn K G Phys. Rev. Lett. 43 (1979) 391

Lynn K G, Schultz P J and Mackenzie I K, Solid State Comm. 38 (1980) 473

Lynn K G and Lutz H, Phys. Rev. B 22 (1980) 4143

Lynn K G in POS81 (1981) 609

Lynn K G, Nielsen B and Quateman J H, App. Phys. Lett 47 (1985) 239

Lynn K G and Nielsen B Phys. Rev. B 36 (1987) 7107

Lynn K G, Gramsch E, Usmar S G and Sferlazzo P, App Phys Lett 55 (1989) 87

Madanski L and Rasetti F, Phys Rev 79 (1950) 397

Marder S, Hughes V, Wu C S and Bennet W, Phys. Rev. 103 (1956) 1258

Maury S, Hyperfine Interactions 109 (1997) 43

McMullen T, (1984) Unpublished

McMullen T in ICPA85 (1985) 657

Merrison J P, Charlton M, Deutch B I and Jørgenson L V, J Phys Condens Matter 4 (1992) L207

Merrison J P, Bluhme H, Chevalier J, Deutch B I, Jørgenson L V, Knudsen H, Poulsen M R and Charlton M, Phys. Rev. Lett 78 (1997) 2728

Mills A P Jr Phys. Rev. Lett. 41 (1978) 1282

Mills A P Jr, Appl Phys Lett 35 (1979) 427

Mills A P Jr, Appl Phys 22 (1980) 273

Mills A P and Wilson R, Phys. Rev. A 26 (1982) 490

Mills A P Jr and Crane W S, Phys Rev Lett. 53 (1984) 2165

Mills A P Jr and Murray C A Appl. Phys. 21 (1980) 323

Mills A P Jr, Platzman P M, Brown B L, Phys Rev Lett 41 (1978) 1076

Mills A P Jr and Gullikson E M, Appl Phys Lett 49 (1986) 1121

Mills A P, Pfeiffer L and Platzman P M, Phys Rev Lett 51 (1986) 1085

Mitroy J, Aust. J. Phys. 48 (1995a) 893

Mitroy J, Aust. J. Phys. 48 (1995b) 645

Mitroy J, Phys. B 29 (1996) L263

Mitroy J and Ryzhikh, J Phys. B 30 (1997) 1332

Mogensen O E Appl. Phys. 6 (1975) 315

Möhl D, Hyperfine Interactions 109 (1997) 33

Mourino M, Lobl H, and Paulin R, Phys. Lett. 71A, (1979) 106

Murray C A and Mills A P Jr, Solid State Comm. 34 (1980) 789

Murphy T J and Surko C M Phys. Rev. A 46 (1992) 5696

Nielsen B, Lynn K G and Chen Yen-C, Phys. Rev. Lett. 57 (1986) 1789

Oliva J, Phys. Rev. B 21 (1980) 4909

Ore A, Univ. i Bergen Arbok Natuvidensabelig Rekke 9 (1949)

Ore A and Powell J L, Phys Rev 75 (1949) 1696

Overton N, Knights A P, Goodyear A, Coleman P G App. Surf. Sci. 85 (1995) 54

Perkins A and Carbotte J P, Phys Rev B 1 (1970) 101

Poulsen M R, Charlton M, Chevalier J, Deutch B I, Jørgensen L and Laricchia G, J Phys. Condens. Matter 3 (1991) 2849

Poulsen M R, Charlton M and Laricchia G, J Phys: Condens Matter 5 (1993) 5209

Pritchard D E, Phys. Rev. Lett. 51 (1983) 1336

Reif F, "Fundamentals of Statistical and Thermal Physics" (1985) McGraw Hill, Singapore

Robinson D C, Nucl. Instr. and Meth 126 (1970) 120

Sasamoto N, Koyama K and Tanaka S I, Nucl. Instr. Meth. 125 (1975) 115

Schultz P J and Lynn K G, Rev Mod Phys 60 (1988) 701

Schultz P J, Gullikson E M and Mills A P Jr, Phys. Rev. B 34 (1986) 442

Stein T S, Kauppila W E and Roellig L O, Rev. Sci. Inst 45 (1974) 951

Stückelberg E C G, Helv. Phys. Acta 14 (1941) 588

Surko C M, Greaves R G and Charlton M, Hyperfine Interactions 109 (1997) 181

Tong B Y, Phys Rev B 5 (1972) 1436

Valkealahti, S and Nieminen R M, Appl. Phys A 32 (1983) 95

Valkealahti, S and Nieminen R M, Appl. Phys A 35 (1984) 51

Vehanen A, Lynn K G, Schultz and Eldrup M, App Phys A 32 (1983) 163

Vehanen A, Saarinen K, Hautojärvi P, and H Huomo, Phys. Rev. B 35 (1987) 4606

Weyl H, Gruppentheorie und Quantunmechanik (1931) 2nd ed. 234

Yang C N, Phys. Rev. 77 (1950) 242

Youssef J, Phys. Rev. D 54 (1996) 168

Ziock K P, Howell R H, Magnota F, Failor R A and Jones K M, Phys. Rev. Lett 64 (1990) 2366